UNIVERSITY
OF LATVIA

Laima Bušaite

MAGNETO-OPTICAL EFFECTS IN RUBIDIUM VAPOR AND NITROGEN–VACANCY CENTERS IN DIAMOND

Doctoral Dissertation

Submitted for the degree of Doctor of Physics
Subfield of Laser Physics and Spectroscopy

Riga, 2021

Abstract

This dissertation covers the development, adaptation and validation of theoretical and numerical models, that describe nonlinear magneto-optical rotation in atomic rubidium as well as hyperfine level mixing and dynamic nuclear spin polarization in nitrogen–vacancy centers in diamond. The models, developed as part of this work, are based on the Liouville equation for quantum systems with added relaxation. The first part of the dissertation is focused on nonlinear magneto-optical rotation for the rubidium $5^2S_{1/2} \longrightarrow 6^2P_{1/2}$ transition. This part describes the influence on rotation signals of partially resolved hyperfine structure as well as repopulation of the ground state via intermediate states. The model was validated using experimental data. The second part of the dissertation encompasses the development of numerical models that describe optically detected magnetic resonance signals and dynamic nuclear spin polarization of nitrogen–vacancy centers. These models are used to analyze the influence of such parameters as the angle between the nitrogen–vacancy axis and the magnetic field direction, crystal strain, relaxation rates and optical pumping rate, which corresponds to laser power. The analysis of the models mainly focuses on the magnetic field regions where magnetic sublevels cross. Experimental data is used to test the developed models.

Contents

List of Abbreviations

CVD	chemical vapor deposition 76, 116, 118
CW	continuous-wave 60, 114
DFT	density functional theory 73
DNP	dynamic nuclear polarization 49, 50, 87, 88, 98, 102
ES	excited state 59, 60
ESLAC	excited-state level anti-crossing 8, 11, 49, 50, 59, 60, 87, 88, 91, 92, 95, 97, 98
GS	ground state 59, 60
GSLAC	ground-state level anti-crossing 8, 11, 48–50, 59–64, 66–68, 70, 71, 77, 78, 80–84, 86–88, 91, 92, 95–99, 101, 102
HFS	hyperfine structure 4, 65–75
HPHT	high-pressure, high-temperature 76, 116
IR	infrared 7, 15, 41, 114, 115
LAC	level anti-crossing 59
MW	microwave 60, 65, 76
NMOR	nonlinear magneto-optical rotation 2, 5, 14, 15, 18, 22, 24, 37, 38, 40–43, 45, 46, 100, 102, 114, 115
NMR	nuclear magnetic resonance 48, 98
NV	nitrogen–vacancy 2, 4, 8–15, 19, 48–58, 60–62, 68–74, 76, 80–84, 86–91, 93–102, 116–118
ODMR	optically detected magnetic resonance 2, 9–13, 15, 48, 49, 60, 61, 66, 68–71, 73, 75–84, 86, 96–98, 100, 102, 117
P1	substitutional nitrogen 81, 97
PM	polarization moment 29, 35
PP KTP	periodically poled potassium titanyl phosphate 114
Rb	rubidium 7, 14, 15, 18, 31, 32

List of Figures

List of Tables

Chapter 1

Introduction

This dissertation is dedicated to magneto-optical effects in two types of media: atomic vapor and nitrogen–vacancy (NV) centers in diamond.

Although these systems are quite different, their behavior exhibits some similarities. The NV center is often called an atom-like defect, which comes from the fact that the NV center's level structure is similar to what we see in an atomic level structure. This allows us to describe the NV centers using methods developed for atoms, although the solid-state characteristics of NV centers, such as phonon relaxations, must be taken into account properly. In addition, the magnetic sublevels of NV centers are separated in the absence of an external field. In alkali atoms the spontaneous relaxation transitions are observed as fluorescence. In NV centers, we also observe fluorescence, but unlike in atoms, there are also nonradiative relaxation pathways, in which the energy is transferred via phonon interaction. Such a pathway is called an intersystem crossing, as the relaxation occurs between triplet and singlet states. It is an essential process for electron and nuclear spin polarization of the NV center.

1.1 Aim and tasks of the dissertation

The goal of the dissertation is to study magneto-optical effects in two different systems, adapt and validate the theoretical model of nonlinear magneto-optical rotation (NMOR) in atomic Rb and explore the hyperfine interaction of nitrogen-vacancy centers in diamond by modeling the processes of hyperfine interaction in the presence of an external magnetic field, which among other effects leads also to nuclear spin polarization of nitrogen.

The tasks of the dissertation are:

1. Adapt the model for describing NMOR to fit the experimental conditions of blue light excitation, which lead to cascade transitions in spontaneous relaxation.

2. Examine the hyperfine-structure interaction in NV centers in the magnetic field range that corresponds to ground-state level-crossing region and analyze the influ-

ence on the optically detected magnetic resonance (ODMR) signals of the different factors, such as imperfections in the alignment of the axis of the NV centers with respect to an applied magnetic field and nuclear spin polarization.

3. Perform numerical calculations of the nuclear spin polarization in NV centers and analyze the influence of such parameters as the angle between the magnetic field and the NV center axis, relaxation transition rates, pumping rate and strain on nuclear spin polarization.

1.2 Contents of the dissertation

The dissertation is divided into two parts. Part I is dedicated to magneto-optical effects in atoms, specifically nonlinear magneto-optical rotation (NMOR) in rubidium. The NMOR signals in Rb vapor are typically measured for the D_1 and D_2 lines, which are excited by infrared (IR) light. If the atom is excited with higher frequency radiation, corresponding to blue light, the repopulation of the ground state can occur via several intermediate states. The aim of this study is to validate the theoretical model for a system with intermediate states as well as unresolved hyperfine structure in the excited state. Chapter 2 gives some general background on nonlinear magneto-optical rotation. Chapter 3 is devoted to the study of nonlinear magneto-optical rotation, for the case of excitation to higher energy levels.

Part II of the dissertation treats magneto-optical effects in nitrogen–vacancy (NV) centers. The aim of this part is to examine the electron- and nuclear-spin interaction that leads to hyperfine structure and mixing of the levels in external magnetic fields. Chapter 5 gives insight into the structure of NV centers. Chapter 6 describes a model that takes into account magnetic-sublevel hyperfine nonlinear splitting and mixing of the levels of NV centers in the vicinity of level crossing and anticrossing to model optically detected magnetic resonance signals. Chapter 7 is devoted to the analysis of the results of numerical simulations of the nuclear spin polarization of NV centers over a wide range of magnetic field values.

The dissertation is based on theoretical calculations that were done in active collaboration with experiments carried out at the University of California at Berkeley, the Laser Centre of the University of Latvia and the Johannes Gutenberg-University in Mainz. The collaboration was mutually enriching because the theoretical model helped to plan, analyze and interpret the experiments, while the experimental results helped to validate the experimental model. The execution of the experiments is not part of the dissertation, but the data analysis and development of fitting procedures are included in the dissertation.

1.3 Publications and author's contribution

1.3.1 Publications covered in the thesis

The results of the research are published in three papers.

[P1] S. Pustelny, L. Busaite, M. Auzinsh, A. Akulshin, N. Leefer, and D. Budker, "Nonlinear magneto-optical rotation in rubidium vapor excited with blue light," Physical Review A, vol. 92, no. 5, 2015.

Author's contribution: Theoretical calculations, model adaptation and signal simulation, part of data analysis, development of fitting procedure.

[P2] M. Auzinsh, A. Berzins, D. Budker, L. Busaite, R. Ferber, F. Gahbauer, R. Lazda, A. Wickenbrock, and H. Zheng, "Hyperfine level structure in nitrogen-vacancy centers near the ground-state level anticrossing," Physical Review B, vol. 100, p. 075204, 8 2019.

Author's contribution: Model development, adaptation and signal calculation, part of data analysis, development of fitting procedure.

[P3] L. Busaite, R. Lazda, A. Berzins, M. Auzinsh, R. Ferber, and F. Gahbauer, "Dynamic 14N nuclear spin polarization in nitrogen-vacancy centers in diamond," Physical Review B, vol. 102, p. 224101, 12 2020.

Author's contribution: Model development and adaptation, data analysis, fitting of experimental data.

1.3.2 Publications not covered in this thesis

[P4] L. Skuja, K. Smits, A. Trukhin, F. Gahbauer, R. Ferber, M. Auzinsh, L. Busaite, L. Razinkovas, M. Mackoit-Sinkevičienė, and A. Alkauskas, "Dynamics of Singlet Oxygen Molecule Trapped in Silica Glass Studied by Luminescence Polarization Anisotropy and Density Functional Theory," Journal of Physical Chemistry C, 2020.

[P5] A. Mozers, L. Busaite, D. Osite, and M. Auzinsh, "Angular momentum alignment-to-orientation conversion in the ground state of Rb atoms at room temperature," Physical Review A, vol. 102, p. 53102, 2020.

[P6] R. Lazda, L. Busaite, A. Berzins, J. Smits, F. Gahbauer, M. Auzinsh, D. Budker, and R. Ferber, "Cross-relaxation studies with optically detected magnetic resonances in nitrogen-vacancy centers in diamond in external magnetic field," Physical Review B, vol. 103, p. 134104, 2021.

[P7] A. Mozers, L. Busaite, D. Osite, and M. Auzinsh, "Alignment-to-orientation conversion in the ground state of atomic Cs with linearly polarized laser excitation," 2020.

1.4 Conferences as a presenting author on the topics of the thesis

[C1] Laima Busaite, Marcis Auzinsh, Szymon Pustelny, Dmitry Budker "Nonlinear Magneto-Optical Rotation in Atomic Rubidium at 6^2P_{Je} Excitation", oral presentation at *Development in Optics and Communication 2013*, April 10–12, 2013, Riga, Latvia.

[C2] Laima Busaite, Marcis Auzinsh, Szymon Pustelny, Dmitry Budker "Theoretical and Experimental Investigation of NMOR in Atomic Rubidium at 6^2P_{Je} Excitation", poster presentation at *The 21st International Conference on Laser Spectroscopy*, June 9–14, 2013, Berkeley, USA.

[C3] Laima Busaite, Marcis Auzinsh, Szymon Pustelny, Dmitry Budker "Investigation of nonlinear magneto-optical rotation in atomic rubidium at 420 nm excitation", oral presentation at *TLL/Colima Joint Workshop*, September 1–5, 2013, Vilnius, Lithuania.

[C4] Laima Busaite, Alexander Akulshin, Marcis Auzinsh, Szymon Pustelny, Dmitry Budker "Nonlinear Magneto-Optical Rotation in Rb Vapor Excited by Blue Light", oral presentation at *Development in Optics and Communication 2014*, April 9–12, 2014, Riga, Latvia.

[C5] Laima Busaite, Alexander Akulshin, Marcis Auzinsh, Szymon Pustelny, Dmitry Budker, Nathan Leefer "Nonlinear Magneto-Optical Rotation in Rubidium Vapor Excited to $6^2P_{1/2}$ State", poster presentation at *47th conference of the European Group on Atomic Systems*, July 14–17, 2015, Riga, Latvia.

[C6] Laima Busaite, Alexander Akulshin, Marcis Auzinsh, Szymon Pustelny, Dmitry Budker, Nathan Leefer "Nonlinear magneto-optical rotation in rubidium vapor in blue light excitation", oral presentation at *74th Scientific Conference of the University of Latvia*, February 2, 2016, Riga, Latvia.

[C7] Laima Busaite, Reinis Lazda, Marcis Auzinsh, Janis Smits, Linards Kalvans, Agris Spiss "Theoretical Modelling of Optically Detectable Magnetic Resonances in Nitrogen-Vacancy Centres in Diamond", poster presentation at *Open Reading 2016*, March 15–18, 2016, Vilnius, Lithuania.

[C8] Laima Bušaite, M. Auziņš, A. Bērziņš, R. Ferber, F. Gahbauer, L. Kalvans, R. Lazda, J. Smits, "Level Crossing Optically Detectable Magnetic Resonance Signals in Nitrogen–Vacancy Centres in Diamonds", 1st TLL Workshop *Quantum and Nonlinear Optics with Rydberg-State Atoms*, November 10–11, 2016, Riga, Latvia.

[C9] Laima Bušaite, Mārcis Auziņš, Ruvins Ferbers, Florians Gahbauers, Reinis Lazda "Optically detected mangnetic resonance signals in nitrogen–vacancy centers in diamond in the presence of strong external magnetic field", oral presentation at *75th Scientific Conference of the University of Latvia*, February 1, 2017, Riga, Latvia.

[C10] Laima Busaite, Marcis Auzinsh, Andris Berzins, Ruvin Ferber, Florian Gahbauer, Reinis Lazda "Optically Detectable Magnetic Resonance Signals in Nitrogen - Vacancy Centres in Diamond Near Ground State Level Crossing", poster presentation at *Open Reading 2016*, March 14–17, 2017, Vilnius, Lithuania.

[C11] Laima Busaite, Marcis Auzinsh, Andris Berzins, Ruvin Ferber, Florian Gahbauer, Reinis Lazda "Level anti-crossing studies in nitrogen – vacancy centers in diamond crystals", poster presentation at *The 23rd International Conference on Laser Spectroscopy*, July 3–7, 2017, Arcachon Convention Centre, France.

[C12] Laima Busaite, Marcis Auzinsh, Andris Berzins, Ruvins Ferbers, Florian Gahbauer, Reinis Lazda "Optically detected magnetic resonance signal studies for nitrogen-vacancy centers near level crossing", oral presentation at *76th Scientific Conference of the University of Latvia*, February 2, 2018, Riga, Latvia.

[C13] Laima Busaite, Marcis Auzinsh, Andris Berzins, Ruvin Ferber, Florian Gahbauer, Reinis Lazda "Level anti-crossing signal dependence on nitrogen-vacancy centre's orientation in magnetic field", oral presentation at *Open Readings 2018*, March 20—23, 2018, Vilnius, Lithuania.

[C14] Laima Busaite, Marcis Auzinsh, Andris Berzins, Ruvin Ferber, Florian Gahbauer, Reinis Lazda "Calculating the Influence of 13C Interaction to Nitrogen - Vacancy Center Level Anti-Crossing Optically Detectable Magnetic Resonance Signals", poster presentation at *Open Readings 2019*, March 19-–22, 2019, Vilnius, Lithuania.

[C15] Laima Busaite, Reinis Lazda, Andris Berzins, Marcis Auzinsh, Ruvin Ferber, and Florian Gahbauer "Optically induced nuclear spin polarization in NV centers", oral presentation at *78th Scientific Conference of the University of Latvia*, January 28, 2020, Riga, Latvia.

[C16] Laima Busaite, Reinis Lazda, Andris Berzins, Marcis Auzinsh, Ruvin Ferber, and Florian Gahbauer "Dynamic nuclear spin polarization in Nitrogen–Vacancy centers in diamond", poster presentation at *The 52nd Conference of the European Group on Atomic Systems (EGAS)*, July 6–8, 2021, Zagreb, Croatia (virtual conference).

[C17] Laima Busaite, Marcis Auzinsh, Ruvin Ferber, Florian Gahbauer, Arturs Mozers, Dace Osite "Development of a 3D single-port magnetometer based on magneto-optical resonances in an alkali vapor", poster presentation at *The 52nd Conference*

of the European Group on Atomic Systems (EGAS), July 6–8, 2021, Zagreb, Croatia (virtual conference).

Part I

Nonlinear magneto-optical rotation in atomic rubidium vapor

Introduction to Part I

Most of the studies of nonlinear magneto-optical rotation (NMOR) are done in alkali vapors on the strong D_1 and D_2 lines, which correspond to the fine structure transitions $5^2S_{1/2} \longrightarrow 5^2P_{1/2}$ and $5^2S_{1/2} \longrightarrow 5^2P_{3/2}$. To a large extent these studies are motivated by the fact that NMOR of the D_1 and D_2 lines of alkali atoms are used to develop extremely sensitive magnetometers for many practical applications [4]. These studies show good agreement between experimental observations and theoretical predictions [5, 6].

A different physical system was explored in the study that is a part of this dissertation. Here, a higher-state excitation ($5^2S_{1/2} \longrightarrow 6^2P_{1/2}$) of the rubidium atom was analyzed. This study was motivated by the fact that these transitions are excited by visible light with a wavelength that is less absorbed by water, and therefore would allow underwater magnetometry of distant objects. In such a system the repopulation of the ground-state sublevels is more complex as it can occur via intermediate states ($6^2S_{1/2}$, $4^2D_{3/2}$, $5^2P_{1/2}$, $5^2P_{3/2}$, see Figure 3.1a). As a result, it was necessary to analyze the role of different relaxation channels in NMOR. Another difference from the D-line excitation is the hyperfine splitting of the excited state. The splitting of the hyperfine levels of the $6^2P_{1/2}$ state is much smaller than the splitting of the $5^2P_{1/2}$ and $5^2P_{3/2}$ states. Thus, this study offers the possibility of investigating the nontrivial influence of excited-state hyperfine splitting on the generation and probing of ground-state coherences [7, 8], one consequence of which is the impossibility of creating higher-rank coherences in the ground state.

In this research a model based on [7] was applied to the atomic system of rubidium vapor excited at the $5^2S_{1/2} \longrightarrow 6^2P_{1/2}$ absorption line. The results of the calculations were compared to the experimental results obtained by exciting and probing the atomic vapor with 421-nm light. The aim was to verify that the real system, which includes different relaxation channels, can be described using a single relaxation parameter for ground-state repopulation.

The observation of NMOR at the $5^2S_{1/2} \longrightarrow 6^2P_{1/2}$ line suggests the possibility of another application. As the $5^2S_{1/2} \longrightarrow 6^2P_{1/2}$ has a low transition strength, the excitation only weakly perturbs the atomic medium. As a result, a nondestructive probe based on blue NMOR may be used to probe laser-cooled and trapped atoms. Although one may argue that this same function could be achieved with stronger transitions such as the D_1 or

D_2 lines using weakly detuned light, the blue-light excitation provides another advantage. Cooling and trapping is performed using near infrared beams, so using the blue light for measurements would increase the precision of the state detection by separating the cooling and trapping beams.

Chapter 2

Theoretical background

Nonlinear magneto-optical rotation (NMOR) is a light-intensity-dependent effect in which the plane of light polarization is rotated during the light's propagation through a medium in the presence of an external magnetic field. This effect has been studied extensively over the years, both experimentally and theoretically [9]. These studies were carried out to increase the understanding of the physical processes of the rotation of light polarization, leading to fundamental insights and practical applications. A detailed understanding of such effects as the creation, evolution, and detection of quantum states in atoms led to development of techniques of quantum-state engineering [5, 10–12] and quantum nondemolition measurements (nondestructive measurement of quantum states) [13, 14]. NMOR has been used in studies of the relaxation of ground-state coherences in atomic vapor [15–18], leading to the development of techniques that enable the generation of long-lived (60 s) ground-state coherences. NMOR has also more practical applications such as in atomic clocks [19], narrow-band optical filters [20], optical magnetometers [4], and laser-frequency locking systems [21]. Fundamental research on the interactions of laser radiation with atoms is an interesting area in which to apply NMOR. The effect has been used in the search for nonmagnetic spin couplings [22–26]. Its use also has been proposed for experiments that focus on the detection of the constituents of dark matter [27].

2.1 Description of NMOR

2.1.1 Linear magneto-optical rotation

Magneto-optical rotation is an effect that causes the rotation of the polarization plane of linearly polarized light that passes through a medium in the presence of a magnetic field. If the magnetic field is applied along the light-propagation direction, it is called theFaraday effect (Figure 2.1), discovered by Michael Faraday in 1845. Linearly polarized light is a combination of left (σ^+) and right (σ^-) circularly polarized components. The difference between the propagation speeds of differently circularly polarized waves results

in a phase shift between the circular components, and so the polarization plane of linearly polarized light is rotated.

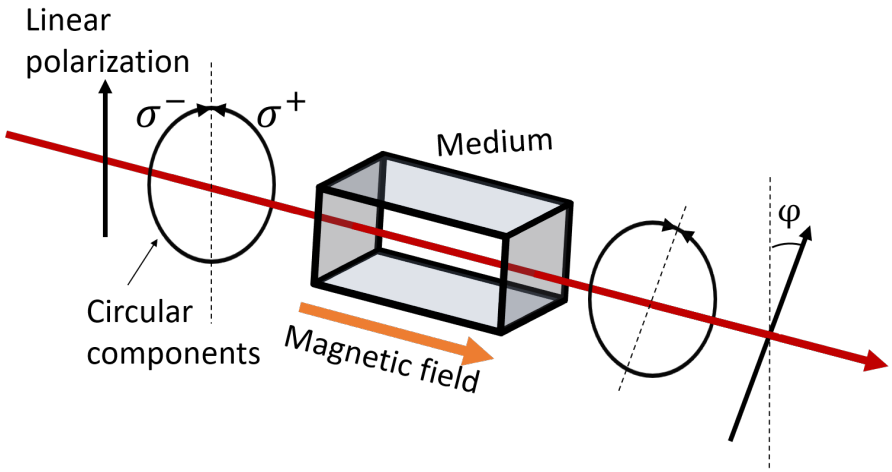

Figure 2.1: Magneto-optical rotation (Faraday effect). Light polarized linearly along the y-axis enters a medium. A magnetic field is applied in the direction of light propagation (z-axis). Left (σ^+) and right (σ^-) circularly polarized light components acquire different phases while propagating through the medium. As a result, the axis of light polarization is rotated by an angle φ.

To describe circularly polarized light it is useful to use the spherical basis defined by [7]

$$\begin{aligned} \hat{\epsilon}_+ &= -\frac{1}{\sqrt{2}}\left(\hat{\epsilon}_x + i\hat{\epsilon}_y\right), \\ \hat{\epsilon}_0 &= \hat{\epsilon}_z, \\ \hat{\epsilon}_- &= \frac{1}{\sqrt{2}}\left(\hat{\epsilon}_x - i\hat{\epsilon}_y\right), \end{aligned} \tag{2.1}$$

If the electrical field is expressed in Cartesian components, we need to express the basis-unit vectors in Cartesian coordinates in the terms of their spherical components [15]

$$\begin{aligned} \hat{\epsilon}_x &= \frac{1}{\sqrt{2}}\left(\hat{\epsilon}_- - \hat{\epsilon}_-\right), \\ \hat{\epsilon}_z &= \hat{\epsilon}_0, \\ \hat{\epsilon}_y &= \frac{i}{\sqrt{2}}\left(\hat{\epsilon}_+ + \hat{\epsilon}_-\right), \end{aligned} \tag{2.2}$$

where $\hat{\epsilon}_x$ and $\hat{\epsilon}_y$ are the basis-unit vectors polarized along the x and y directions, and $\hat{\epsilon}_+$ and $\hat{\epsilon}_-$ are the vectors representing right and left circularly polarized light, respectively.

The electric field of light linearly polarized along the x-axis can be described by

$$\begin{aligned} \vec{E} &= E_0\,\hat{\epsilon}_x \cos(kz - \omega t) = \\ &= \frac{E_0}{2}\left[\frac{\hat{\epsilon}_-}{\sqrt{2}}e^{i(k_- z - \omega t)} - \frac{\hat{\epsilon}_+}{\sqrt{2}}e^{i(k_+ z - \omega t)}\right] + \frac{E_0}{2}\left[\frac{\hat{\epsilon}_-}{\sqrt{2}}e^{-i(k_- z - \omega t)} - \frac{\hat{\epsilon}_+}{\sqrt{2}}e^{-i(k_+ z - \omega t)}\right], \end{aligned} \tag{2.3}$$

where E_0 is the amplitude of the optical electric field, and ω is the frequency of the light. The magnitude of the wavevectors $k_\pm$ are given as

$$k_\pm = \frac{2\pi}{\lambda} = \frac{\eta_\pm \omega}{c}, \tag{2.4}$$

where λ is the wavelength of light, and $\eta_\pm$ is the complex refractive index

$$\eta_\pm = n_\pm + i\kappa_\pm. \tag{2.5}$$

The imaginary part of the complex refractive index is the absorption coefficient $\kappa_\pm$, and the real part is the refractive index $n_\pm$, which characterizes the dispersion of the medium.

If the refractive indices (n_- and n_+) of the circular components of the light polarization are different, each propagates in medium with different velocity, leading to a phase difference:

$$\varphi = \frac{\omega \ell}{c}(n_+ - n_-), \tag{2.6}$$

where ℓ is the path length in the active medium. The phase difference leads to a rotation of the polarization plane by an angle ϕ:

$$\phi = \frac{\varphi}{2}. \tag{2.7}$$

A difference in absorption coefficients leads to elliptical light polarization.

At the end of the 18th century Domenico Macaluso and Orso Corbino discovered a strong dependence of the magneto-optical rotation on light frequency: the Faraday effect was shown to have a resonant character in the vicinity of the resonance absorption lines. The Macaluso-Corbino effect can be explained in an $F = 1 \longrightarrow F' = 0$ atomic transition, where F and F' are the total angular momenta of the ground and excited states (Figure 2.2).

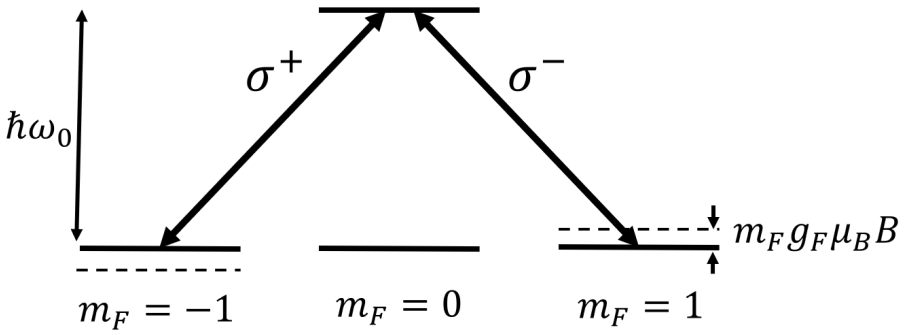

Figure 2.2: Energy level scheme for the $F = 1 \longrightarrow F' = 0$ atomic transition. The Zeeman sublevels are shifted by the magnetic field, which changing the resonance frequencies for the right and left circularly polarized components.

Light that is linearly polarized perpendicularly to magnetic field direction (quantization axis) can be considered as being composed of two counter-rotating circular components (σ^+ and σ^-). The right circularly polarized (σ^-) component of the linearly

polarized light interacts with the atom, generating a transition between the Zeeman sublevels $m_F = +1$ of ground state and $m_{F'} = 0$ of excited state. In the same way, the left circularly polarized (σ^+) component of the linearly polarized light generated transition between $m_F = -1$ and $m_{F'} = 0$.

In the case of narrow-band light that interacts with a low-density atomic vapor described by a two-level transition, the complex refractive index can be expanded as

$$\eta \approx 1 + 2\pi\chi_0 \frac{1}{(\omega - \omega_0) + i\Gamma/2}, \tag{2.8}$$

where ω is the frequency of the light, ω_0 is the transition frequency, Γ is the relaxation rate of excited state, and χ_0 is the atomic linear susceptibility. If the light field is weak enough, it can be assumed that the atom can be excited by each of the polarization eigenmodes independently. If a magnetic field is not applied, the Zeeman sublevels are degenerate and the resonance frequencies for both absorption components are the same. The real part of the refractive index n as a function of light detuning is shown in Figure 2.3a as a blue solid dispersion curve. The refractive index for both of the circular components is the same, and no rotation of the polarization plane of the light is observed.

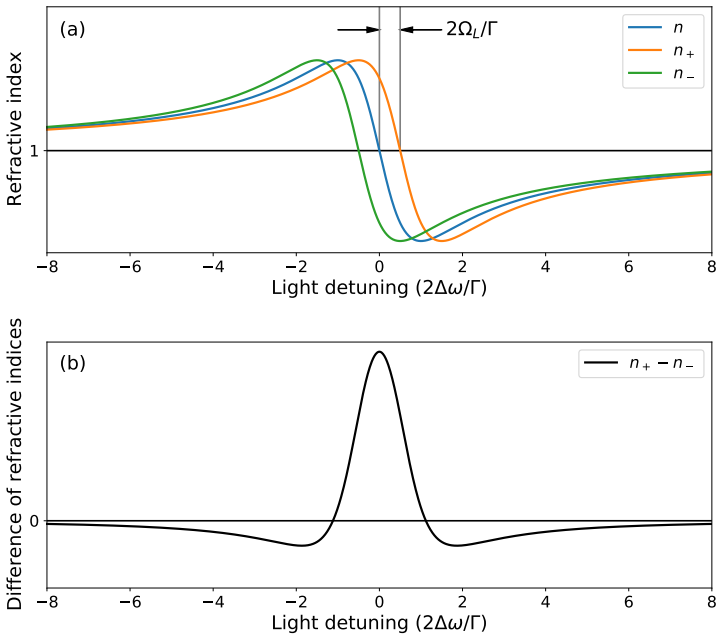

Figure 2.3: (a) Dependence of refractive index on light frequency detuning in the absence (n) and presence ($n_\pm$) of magnetic field. (b) The difference between refractive indices leads to a dependence of the magneto-optical rotation on the detuning of the light frequency.

When a magnetic field is applied along light propagation direction, the Zeeman sublevels are shifted by an amount that corresponds to the Larmor frequency Ω_L (Figure 2.2):

$$\Omega_L = m_F g_F \mu_B B, \tag{2.9}$$

where g_F is Landé factor and μ_B is the Bohr magneton. Due to the resonance frequency shift, the refractive index [Eq. (2.8)] is modified for each of the circular components:

$$\eta_{\pm} \approx 1 + 2\pi\chi_0 \frac{1}{(\Delta\omega \mp \Omega_L) + i\Gamma/2}, \tag{2.10}$$

where $\Delta\omega = \omega - \omega_0$ is the light-frequency detuning from resonance in the absence of magnetic field.

The difference in the real parts of refractive indices of circular components leads to rotation of the polarization plane. The angle of rotation can be calculated as a function of magnetic field and light frequency detuning by combining Eqs. (2.6), (2.7) and (2.10):

$$\phi \approx \frac{4\pi\chi_0\omega\ell}{c} \frac{\Omega_L \left(\Delta\omega^2 - \Omega_L^2 - \Gamma^2/4\right)}{\left(\Delta\omega^2 - \Omega_L^2 - \Gamma^2/4\right)^2 + \left(\Gamma \cdot \Delta\omega\right)^2} \tag{2.11}$$

2.1.2 Nonlinear effects

The optical properties of the medium depend on the intensity of the applied light. Nonlinear light–atom interactions can be described as a three-stage process:

- pumping: modifying the properties of the medium by light;
- evolution: the medium and its properties evolve by interacting with other fields, such as a magnetic field;
- probing of the properties of the medium

All of these processes occur simultaneously, but it is useful to look at these processes individually, as though separated in time, when explaining the principles and building models.

Light-induced polarization of atoms characterizes the properties of the medium

$$\mathbf{P} = \mathrm{Tr}[\rho(\mathbf{E_0})\mathbf{d}] \tag{2.12}$$

where $\mathbf{d}$ is the electric dipole moment, and E_0 is the amplitude of the electric field of the light. The quantum state is described by the density operator ρ

$$\rho = \frac{1}{N} \sum_{i=1}^{N} |\psi_i\rangle \langle\psi_i| , \tag{2.13}$$

which is averaged over an ensemble. $|\psi_i\rangle$ is a state vector.

2.1.3 The Liouville equation

The interaction of atoms in a vapor cell with external optical and magnetic fields can be described by the density-matrix formalism. The time evolution of the density matrix ρ can be described by the Liouville equation ($\hbar = 1$, $c = 1$) [7]:

$$\dot{\rho} = -i\Big[\hat{H}, \rho\Big] - \frac{1}{2}\Big\{\hat{\Gamma}, \rho\Big\} + \hat{\Lambda} + \mathrm{Tr}\Big(\hat{\mathcal{F}}\rho\Big), \tag{2.14}$$

where $\hat{H} = \hat{H}_0 + \hat{V}$ is time-independent Hamiltonian, which consists of the unperturbed system Hamiltonian $\hat{H}_0$ and the interaction Hamiltonian $\hat{V}$. $\hat{\Gamma}$ is the relaxation operator, which accounts for such processes as transit relaxation due to the thermal velocity of atoms and the relaxation of the excited state due to spontaneous emission, Λ is repopulation operator that describes repopulation processes that are independent of the density matrix, such as processes induced by wall collisions or transit relaxation, and $\hat{\mathcal{F}}$ is the density-matrix-dependent repopulation operator, which describes processes such as repopulation of the ground states due to spontaneous emission from the excited states. The spontaneous emission operator ($\hbar = 1$, $c = 1$) is defined as [28]

$$\mathcal{F}^{sr}_{mn} = \frac{4}{3}\omega^3_{rm}\mathbf{d}_{mr} \cdot \mathbf{d}_{sn}, \tag{2.15}$$

which connects the excited-state levels $|s\rangle$, $|r\rangle$ with the ground-state levels $|m\rangle$, $|n\rangle$. The trace in (2.14) is calculated over the excited state levels.

The quantum operators in (2.14) can be written in an irreducible tensor basis. A quantum operator $\hat{A}$ can be written as:

$$\hat{A} = \sum_{\kappa q} A^{\kappa q}_{FF'} T^{(\kappa)}_{q;FF'}, \tag{2.16}$$

where $T^{(\kappa)}_{q;FF'}$ is the q-th component of the irreducible tensor with rank κ ($\kappa = 0, \ldots, 2F$ and $q = -\kappa, \ldots, \kappa$). $A^{\kappa q}_{FF'}$ are the components of the polarization moments (PMs) or multipoles. F and F' indicate the set of quantum numbers of total angular momentum for the states on which the operator is acting.

The polarization moments $A^{\kappa q}_{FF'}$ of the operator $\hat{A}$ are related to the matrix elements $A_{Fm,F'm'}$ of operator $\hat{A}$ in the $|Fm\rangle$ basis, where m and m' are the magnetic quantum numbers in terms of the Clebsch-Gordan coefficients [8]:

$$A^{\kappa q}_{FF'} = \mathrm{Tr}\left[A\left(T^{(\kappa)}_{q;FF'}\right)^\dagger\right] = \sum_{mm'}(-1)^{F'-m'} \langle FmF'-m'|\kappa q\rangle\, A_{Fm,F'm'}. \tag{2.17}$$

To write the polarization moments in the form of (2.17), we should consider the orthogonality condition

$$\mathrm{Tr}\left[T^{(\kappa)}_{q;F_1F_2}\left(T^{(\kappa')}_{q';F'_1F'_2}\right)^\dagger\right] = \delta_{\kappa\kappa'}\delta_{qq'}\delta_{F_1F'_1}\delta_{F_2F'_2} \tag{2.18}$$

and the phase convention

$$\left[T^{(\kappa)}_{q;FF'}\right]^\dagger = T^{(\kappa q)}_{FF'}, \tag{2.19}$$

where $T^{(\kappa)}_{q;FF'}$ is the covariant tensor and $T^{(\kappa q)}_{FF'}$ is the contravariant tensor.

These relations can be used to expand the density operators as well as other operators in (2.14). The Liouville equation in the irreducible tensor basis can be written

as [7]

$$\dot{\rho}^{(\kappa q)}_{F_g F'_g} = i(-1)^{F_g+F'_g+\kappa+1} \sum_{\kappa',\kappa'',q',q'',F''} \sqrt{(2\kappa'+1)(2\kappa''+1)}\, \langle \kappa' q' \kappa'' q'' | \kappa q \rangle \begin{Bmatrix} \kappa' & \kappa'' & \kappa \\ F'_g & F_g & F'' \end{Bmatrix} \times$$
$$\times \left[\left(H^{(\kappa' q')}_{F_g F''} - \frac{i}{2}\Gamma^{(\kappa' q')}_{F_g F''} \right) \rho^{(\kappa'' q'')}_{F'' F'_g} - \rho^{(\kappa' q')}_{F_g F''} \left(H^{(\kappa'' q'')}_{F'' F'_g} + \frac{i}{2}\Gamma^{(\kappa'' q'')}_{F'' F'_g} \right) \right] +$$
$$+ \Lambda^{(\kappa q)}_{F_g F'_g} + \frac{4}{3}\omega_0^3 \sum_{F_e, F'_e > F_g, F'_g} \langle F_g \| d \| F_e \rangle\, \rho^{(\kappa q)}_{F_e F'_e} \left\langle F'_e \| d \| F'_g \right\rangle (-1)^{F_e+F'_e+\kappa+1} \begin{Bmatrix} \kappa & F'_g & F_g \\ 1 & F_e & F'_e \end{Bmatrix}. \tag{2.20}$$

To be able to compare different hyperfine transitions, we express the reduced dipole matrix element for hyperfine transitions $\langle F_g \| d \| F_e \rangle$ through the dipole matrix element for fine-structure transitions $\langle J_g \| d \| J_e \rangle$ as [8]

$$\langle F_g \| d \| F_e \rangle = (-1)^{J_e+I+F_g+1} \sqrt{(2F_g+1)(2F_e+1}} \begin{Bmatrix} J_e & F_e & I \\ F_g & J_g & 1 \end{Bmatrix} \langle J_g \| d \| J_e \rangle\,, \tag{2.21}$$

where I is nuclear spin and J is electron angular momentum. The reduced dipole matrix element $\langle J_g \| d \| J_e \rangle$ can be calculated from [7]

$$R\gamma_e = \frac{4}{3}\frac{\omega_0^3}{2J_e+1} |\, \langle J_g \| d \| J_e \rangle\, |^2, \tag{2.22}$$

where R is the branching ratio for the transition $J_e \longrightarrow J_g$, γ_e is the excited-state relaxation rate and ω_0 is the transition frequency between the ground and excited states.

The first two terms of equation (2.14) are combined in equation (2.20) by the expression under the sum. The second term in (2.20) describes the density-matrix-independent repopulation, and the last term describes the density-matrix-dependent repopulation caused by spontaneous relaxation.

Chapter 3

Nonlinear magneto-optical rotation with blue light

In this chapter we apply a model that was developed in [7] for an atomic system with unresolved hyperfine structure in the excited state due to Doppler broadening. The model describes the rotation of the polarization plane of light as it traverses vapor of atomic rubidium. This model was adapted to the excitation of the $5^2S_{1/2} \longrightarrow 6^2P_{1/2}$ transition in the scope of the thesis. To compare the results of the model with the experimental results, the model needs to be adapted to the experimental conditions. We have to take into account the difference of laser beam profiles in the model and in the experiment, which leads to requires an adjustment of the Rabi frequency and the ground-state relaxation rate. The model is then tested by comparing its results to experimental data that were obtained at the University of California at Berkeley by Dr. Szymon Pustelny. The experimental measurement process is not part of the dissertation. The results described in this chapter are published in [29].

3.1 Modeling NMOR for higher level excitation

3.1.1 Atomic system

The atomic system used in the model calculations is Rb vapor with atoms moving at a thermal velocity that corresponds to a temperature of 85°C. Atoms are excited on the $5^2S_{1/2} \longrightarrow 6^2P_{1/2}$ transition. The excitation beam and magnetic field are directed along the quantization axis (x-axis), so that the electric field vector is perpendicular to the quantization axis and is parallel to the z-axis. The excitation geometry is show in Figure 3.1a. The repopulation of the ground state can happen through direct spontaneous transitions back to the initial $5^2S_{1/2}$ state as well as through spontaneous transitions via intermediate states ($6^2S_{1/2}$, $4^2D_{3/2}$, $5^2P_{1/2}$, $5^2P_{3/2}$) (Figure 3.1b).

The model describes a simplified system in which repopulation of the ground state

due to spontaneous decay is characterized by a single parameter based on the branching ratio R (Figure 3.1c). According to this approach, the cascade transitions (Figure 3.1b) are substituted by a single relaxation rate from the excited state to the ground state. In each of the cascade transitions the atomic polarization decreases [30], so the direct transitions play a more significant role in polarization transfer compared to transitions via intermediate states.

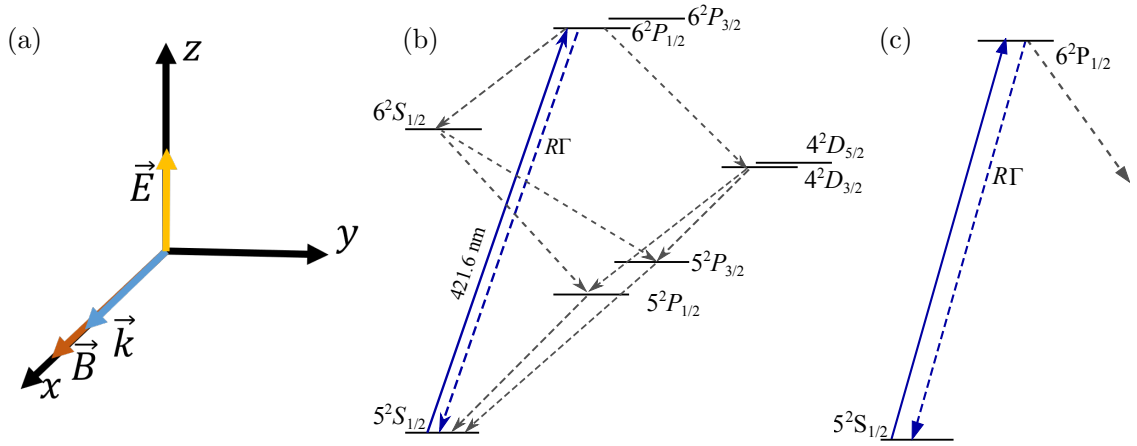

Figure 3.1: (a) Excitation geometry. (b) Energy states and transitions of Rb atoms excited by resonant radiation at 421.6 nm. (c) Simplified level scheme depicting the two-level scheme used in the model. The solid line indicates the excitation light, the dashed lines indicate channels of spontaneous emission.

Figure 3.2 shows hyperfine transitions of ^{85}Rb and ^{87}Rb. The Doppler width at the temperatures of the vapor cell in the experiment (85°C) is around 600 MHz, so the excited state hyperfine levels are unresolved under the Doppler profile.

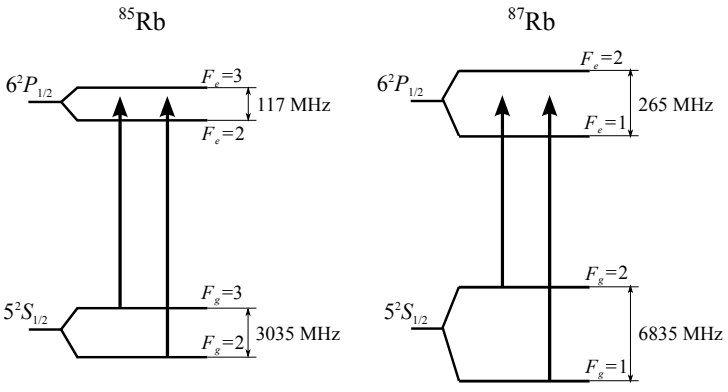

Figure 3.2: Energy level diagram of the $5^2S_{1/2} \longrightarrow 6^2P_{1/2}$ transitions in ^{85}Rb and ^{87}Rb.

3.1.2 Description of the theoretical model

Magneto-optical rotation can be analyzed as a three-stage process. It consists of optical pumping, evolution and probing of the atomic state. In the first stage, the applied

light pumps atoms, modifying their optical properties and introducing anisotropy to the medium. Light polarization defines the axis of the generated anisotropy. During the second stage, the angular momentum anisotropy created in ground and excited states evolves. The evolution of the atomic state is caused by an external magnetic field, resulting in precession of the anisotropy of angular momentum distribution around the magnetic field vector. In addition to precession, the system undergoes relaxation processes leading to relaxation of atomic polarization and optical anisotropy of the medium. In the final stage we can observe the modified properties of the medium as it affects the propagation of light, leading to rotation of light polarization. In an experiment all of these stages occur simultaneously, but for theoretical model purposes, they can be considered independently.

To describe the evolution of the quantum system, we use the density matrix formalism. Light interaction with atoms is described semi-classically by the electric-dipole-interaction Hamiltonian. Optical excitation occurs together with spontaneous emission, which is described in the Liouville equation (2.14) by the spontaneous emission operator $\hat{\Gamma}$, and repopulation due to spontaneous emission $\hat{\mathcal{F}}$. Both optical excitation and spontaneous emission are responsible for optically pumping the medium and generating polarization in the medium. In a real system, when exciting the transition $5^2S_{1/2} \longrightarrow 6^2P_{1/2}$, the state relaxes through several intermediate states (Figure 3.1b). In this model, we use a single excited-state relaxation rate, because the polarization transfer from the excited state to the ground state via intermediate states is weaker than that caused through direct transitions. This results of our study show that reducing the cascade system to a two-state system is an acceptable approximation for low light intensity and weak magnetic field conditions [29].

Optical pumping

To describe optical pumping, it is useful to employ the irreducible tensor expansion of the density matrix. This makes it easier to simplify the theoretical description. In a low-light-intensity excitation regime, when an unpolarized atom absorbs a photon, it may only create the three lowest polarization moments: population, orientation, and alignment.

Equation (2.20) is used to calculate the evolution of the density matrix during the first stage, optical pumping, during which atomic polarization is generated. The full Hamiltonian can be written as $\hat{H} = \hat{H}_0 + \hat{V}$, where $\hat{H}_0$ is the system Hamiltonian (atom in absence of excitation) and $\hat{V}$ is the time-independent perturbation operator. At this stage the magnetic field is neglected. The interaction operator of the first stage can be written as a light-atom electronic dipole interaction:

$$\hat{V}_{pump} = -\mathbf{d} \cdot \mathbf{E}, \tag{3.1}$$

where $\mathbf{d}$ is the electric dipole moment and $\mathbf{E} = E_0 \,\mathrm{Re}(\hat{\mathbf{e}} e^{i(\mathbf{k}\cdot\mathbf{r}-\omega t)})$ is the electric field of the light in the x-axis direction ($\hat{\mathbf{e}} = \hat{\mathbf{x}}$ and $\hat{\mathbf{k}} = \hat{\mathbf{z}}$) with E_0 being the optical electric

field amplitude. In the rotating wave approximation, the electric-dipole Hamiltonian is written as

$$\hat{V}'_{pump} = -\frac{1}{2} d_z E_0, \tag{3.2}$$

where the prime refers to the rotating frame.

Evolution of polarization in a magnetic field

In the second stage, when the polarization evolves under the influence of the magnetic field, the interaction operator is replaced by an external-magnetic-field (Zeeman) interaction operator

$$\hat{V}_{evol} = -\boldsymbol{\mu} \cdot \mathbf{B}, \tag{3.3}$$

where $\mathbf{B}$ is the magnetic field vector in the x-axis direction, and $\boldsymbol{\mu}$ is the magnetic dipole moment.

Probing the ground state polarization

In the third stage the ground state polarization is probed. To calculate the rotation of light polarization we use the macroscopic polarization of the medium, using

$$\frac{\partial^2 \mathbf{E}}{\partial \ell^2} - \frac{\partial^2 \mathbf{E}}{\partial t^2} = 4\pi \frac{\partial^2 \mathbf{P}}{\partial t^2}, \tag{3.4}$$

where ℓ is the distance along the direction of light propagation. The relation of the medium's dipole polarization $\mathbf{P}$ and the density matrix ρ is given by $\mathbf{P} = N_{\text{at}} \operatorname{Tr}\{(\rho \mathbf{d})\}$, where N_{at} is the atomic density. To relate the polarization $\mathbf{P}$ to the density matrix $\tilde{\rho}$ in the rotating frame, we can write it as

$$\mathbf{P} = N_{\text{at}} \sum_{F_g m_g F_e m_e} 2\text{Re}(\tilde{\rho}_{F_g m_g, F_e m_e} \mathbf{d}_{F_g m_g, F_e m_e}) e^{i(\mathbf{k}\cdot\mathbf{r} - \omega t)}, \tag{3.5}$$

where $\mathbf{d}_{F_g m_g, F_e m_e}$ is the electronic-dipole matrix element between the ground state $|F_g m_g\rangle$ and the excited state $|F_e m_e\rangle$, $\tilde{\rho}_{F_g m_g, F_e m_e}$ is the corresponding density-matrix element in the rotating frame, and ω is the light frequency. This allows us to calculate electric susceptibility of the medium as well as refractive indices of two orthogonal circular polarization components of light responsible for the rotation of the light's polarization.

Following this approach, the polarization rotation of light can be expressed as

$$\frac{d\varphi}{d\ell} = -\frac{4\pi\omega N_{\text{at}}}{\varepsilon_0} \sum_{F_g m_g F_e m_e} \text{Im}\left[\rho'_{F_g m_g, F_e m_e} \mathbf{d}_{F_g m_g, F_e m_e} \cdot \left(\hat{\mathbf{k}} \times \hat{\mathbf{e}}\right)\right], \tag{3.6}$$

where $\hat{\mathbf{k}}$ is the unit vector of the wave vector $\mathbf{k}$, and $\hat{\mathbf{e}}$ is the light-polarization unit vector.

To obtain the optical rotation for weak probe light in terms of the ground-state density matrix, we can use first-order perturbation theory for optical coherences and

neglect coherences between nondegenerate ground states [8]:

$$\frac{d\varphi}{d\ell} = -2\pi\omega N_{\mathrm{at}}\mathrm{Im}\left[\hat{\mathbf{e}}\cdot\bar{\beta}\cdot\left(\hat{\mathbf{k}}\times\hat{\mathbf{e}}\right)\right], \tag{3.7}$$

where the tensor $\bar{\beta}$ is presented in the irreducible tensor basis as

$$\bar{\beta} = \sum_{F_g F_e \kappa q' q''} \frac{(-1)^{F_g+F_e+\kappa}}{\tilde{\omega}_{F_e F_g}} \hat{\epsilon}_{-q'}\hat{\epsilon}_{-q''}\langle 1q'1q''|\kappa\ q'+q''\rangle \begin{Bmatrix} 1 & 1 & \kappa \\ F_g & F_g & F_e \end{Bmatrix} |\langle F_g\|d\|F_e\rangle|^2 \rho^{(\kappa\ q'+q'')}_{F_g F_g}, \tag{3.8}$$

where $\hat{\epsilon}_q$ (2.1) is a spherical-basis unit vector.

In this model the multi-photon effects are not taken into account. A single photon is a spin-1 particle, so it can support PMs up to $\kappa = 2$. In the optical-pumping stage, the magnetic field is neglected, and therefore the ground-state atomic polarization produced in this stage is parallel to the direction of the linear polarization of the light; thus, it has a $q = 0$ polarization component. And as there is no preferred direction, but only a preferred axis, only the PM $\rho^{(20)}$ can be generated as a result of the light-atom interaction, while simultaneously modifying the polarization moment $\rho^{(00)}$ in the interaction.

The rotation of light polarization can only be caused by the PMs with rank $\kappa = 1$ or $\kappa = 2$. In fact, the only PM affecting the rotation of the polarization plane is $\rho^{2\ \pm1}_{F_g F_g}$ (this follows from analysis of Equation (3.8)). Taking this into account, the rotation of the plane of polarization of z-polarized light passing trough an atomic vapor that consists of a single velocity group with completely resolved hyperfine structure ($\omega_{F_g F'_g},\ \omega_{F_e F'_e} \gg \gamma_e$) is given by [7]

$$\begin{aligned} \ell_0\frac{d\varphi}{d\ell} = \frac{3}{4}\kappa_s \sum_{F_g F_e} (-1)^{2F_g} \frac{(2F_e+1)^3(2F_g+1)^3}{(2I+1)} \begin{Bmatrix} 1 & 1 & 2 \\ F_g & F_g & F_e \end{Bmatrix} \begin{Bmatrix} J_e & F_e & I \\ F_g & J_g & 1 \end{Bmatrix}^4 \\ \times x_{F_g}\left[L\left(\omega'_{F_e F_g}\right)\right]^2 \left(\frac{(-1)^{2I+2J_g}}{(2F_e+1)(2F_g+1)} \begin{Bmatrix} 1 & 1 & 2 \\ F_g & F_g & F_e \end{Bmatrix} \right. \\ \left. + R\,(-1)^{F_g-F_e}(2J_e+1) \begin{Bmatrix} 1 & 1 & 2 \\ F_e & F_e & F_g \end{Bmatrix} \begin{Bmatrix} F_g & F_g & 2 \\ F_e & F_e & 1 \end{Bmatrix} \begin{Bmatrix} J_e & F_e & I \\ F_g & J_g & 1 \end{Bmatrix}^2 \right), \end{aligned} \tag{3.9}$$

where $\ell_0 = -\left(\frac{1}{\mathcal{I}}\frac{d\mathcal{I}}{d\ell}\right)^{-1}$ is the unsaturated absorption length, and

$$\kappa_s = \frac{\langle J_g||d||J_e\rangle^2 E_0^2}{\gamma_g\gamma_e} = \frac{\Omega_R^2}{\gamma_g\gamma_e} \tag{3.10}$$

is the reduced saturation parameter. The Lorentz profile $L\left(\omega'_{F_e F_g}\right)$ is given by

$$L\left(\omega'_{F_e F_g}\right) = \frac{(\gamma_e/2)^2}{(\gamma_e/2)^2 + (\omega'_{F_e F_g})^2}, \tag{3.11}$$

where $\omega'_{F_eF_g} = -\Delta\omega_{F_eF_g} + \mathbf{k}\cdot\mathbf{v}$ is the Doppler-shifted transition frequency of a pair of hyperfine states with $\Delta\omega_{F_eF_g}$ being the detuning of light from the optical transition and v being the velocity of atoms. The magnetic-lineshape parameter x_{F_g} is given by

$$x_{F_g} = \frac{(\gamma_g/2)\Omega_{F_g}}{(\gamma_g/2)^2 + (\Omega_{F_g})^2}, \tag{3.12}$$

where γ_g is the ground-state relaxation rate and $\Omega_{F_g} = g_{F_g}\mu_B B$ is the Larmor frequency of the ground-state hyperfine level F_g with g_{F_g} being the Landé factor of the ground state F_g, and μ_B being the Bohr magneton.

In Equation (3.9) the Doppler shift characterizes the motion of the atoms from a single velocity group. To describe properly the atomic ensemble, the velocity distribution of the atoms in the sample must be introduced. The polarization of the optically pumped atoms disappears when the atoms collide with the cell wall, so the summation can be done over the signals of each velocity group calculated independently with weights given by the Maxwell distribution. The polarization rotation of an averaged ensemble can be calculated as [7, 8, 29]

$$\begin{aligned}\left\langle \ell_0 \frac{d\varphi}{d\ell} \right\rangle_v = \frac{3}{8}\kappa_s \sum_{F_gF_e} (-1)^{2F_g} \frac{(2F_e+1)^3 (2F_g+1)^3}{(2I+1)} \begin{Bmatrix} 1 & 1 & 2 \\ F_g & F_g & F_e \end{Bmatrix} \begin{Bmatrix} J_e & F_e & I \\ F_g & J_g & 1 \end{Bmatrix}^4 \\ \times e^{-(\Delta_{F_eF_g}/\Gamma_D)^2} x_{F_g} \left(\frac{(-1)^{2I+2J_g}}{(2F_e+1)(2F_g+1)} \begin{Bmatrix} 1 & 1 & 2 \\ F_g & F_g & F_e \end{Bmatrix} \right. \\ \left. + R\,(-1)^{F_g-F_e} (2J_e+1) \begin{Bmatrix} 1 & 1 & 2 \\ F_e & F_e & F_g \end{Bmatrix} \begin{Bmatrix} F_g & F_g & 2 \\ F_e & F_e & 1 \end{Bmatrix} \begin{Bmatrix} J_e & F_e & I \\ F_g & J_g & 1 \end{Bmatrix}^2 \right),\end{aligned} \tag{3.13}$$

where Γ_D is the Doppler width. If the excited-state splitting is much smaller than the Doppler width ($\omega_{F_eF'_e} \ll \Gamma_D$) and the ground-state hyperfine splitting is much larger than

the natural width ($\omega_{F_gF_g'} \gg \gamma_e$), the rotation of the polarization can be expressed as

$$\begin{aligned}\left\langle \ell_0 \frac{d\varphi}{d\ell} \right\rangle_v = \frac{3}{8}\kappa_s \sum_{F_gF_eF_e''} (-1)^{2F_g+F_e''-F_e} \frac{(2F_e+1)(2F_e''+1)(2F_g+1)}{(2I+1)} \\ \times \begin{Bmatrix} 1 & 1 & 2 \\ F_g & F_g & F_e'' \end{Bmatrix} \begin{Bmatrix} J_e & F_e & I \\ F_g & J_g & 1 \end{Bmatrix}^2 \begin{Bmatrix} J_e & F_e'' & I \\ F_g & J_g & 1 \end{Bmatrix}^2 x_{F_g} \\ \times \left(\frac{(-1)^{2I+2J_g}}{(2F_e+1)(2F_g+1)} \begin{Bmatrix} 1 & 1 & 2 \\ F_g & F_g & F_e \end{Bmatrix} \right. \\ + R \sum_{F_e'} (-1)^{F_g-F_e'} (2J_e+1)(2F_g+1)(2F_e'+1) \\ \times \begin{Bmatrix} 1 & 1 & 2 \\ F_e & F_e' & F_g \end{Bmatrix} \begin{Bmatrix} F_g & F_g & 2 \\ F_e & F_e' & 1 \end{Bmatrix} \begin{Bmatrix} J_e & F_e' & I \\ F_g & J_g & 1 \end{Bmatrix}^2 \\ \left. \times \frac{2\gamma_e^4 + (2\gamma_e^2 + \omega_{F_eF_e'}^2)\omega_{F_eF_e''}\omega_{F_e'F_e''}}{2(\gamma_e^2+\omega_{F_eF_e'}^2)(\gamma_e^2+\omega_{F_e'F_e''}^2)} \right) \frac{e^{-(\Delta_{F_eF_g}/\Gamma_D)^2}\gamma_e^2}{\gamma_e^2+\omega_{F_eF_e''}^2}.\end{aligned} \tag{3.14}$$

Equation (3.14) was used to simulate Doppler-broadened blue NMOR signals in this study.

3.2 Experimental verification of the model

The experiment was done at the University of California, Berkeley by Dr. Szymon Pustelny. The detailed description of the experiment is presented in Appendix A.1. In the experiment the frequency doubled laser light from a titan-sapphire laser is directed through a rubidium-vapor cell, which is placed inside a four-layer cylindrical μ-metal, magnetic shield (Figure 3.3). A set of additional coils inside the shield were used to apply a bias magnetic field, so that the magnetic field direction coincides with the direction of light-beam propagation. The light entering the vapor cell was linearly polarized. The beam diameter was controlled with an iris. After the cell the polarization of the light was detected with two photodiodes, which detected two orthogonally linearly polarized components I_1 and I_2. The small rotation angle was then calculated [31] as

$$\varphi = \frac{I_1 - I_2}{2(I_1 + I_2)}. \tag{3.15}$$

The experimental measurement process is not part of the dissertation. Nevertheless, the author of the dissertation carried out part of the data analysis and matched the fitting parameters to the experimental measurements.

3.2.1 Model adaptation

To investigate the validity of the model, the simulated, blue NMOR signals were compared with the experimental results.

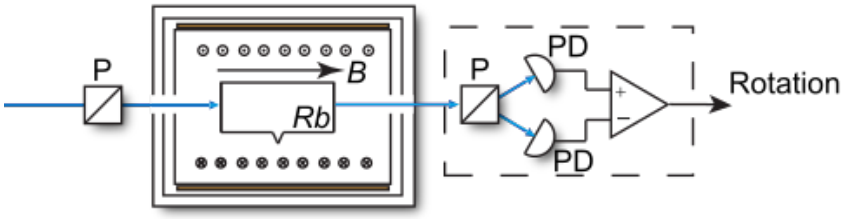

Figure 3.3: Simplified experimental scheme. Linearly polarized light passes through a cell of atomic rubidium, which is inserted inside a magnetic shield with coils that provide a bias magnetic field. The linearly polarized components of the exiting light are detected with photodiodes and the rotation of the polarization plane is determined.

To describe the problem correctly, several experimental parameters had to be determined. There are two types of parameters: those that are assumed to be known precisely, such as the Larmor frequency Ω_{F_g} (3.12) and the Doppler width Γ_D (3.14), which can be determined based on the temperature of the vapor, the strength of the magnetic field and the excitation scheme, and those that can only be estimated and have to be adjusted to fit experimental conditions, such as the Rabi frequency Ω_R [used to calculate the saturation parameter (3.10)] and the ground-state relaxation rate γ_g [used to calculate the saturation parameter (3.10) and magnetic-lineshape parameter (3.12)]. The latter is adjusted by using fitting parameters k_R and k_γ.

The ground-state relaxation rate depends primarily on the time of flight of the atoms across the beam, as atom-atom collisions are rare in the case under consideration. A simple approach is to assume that the rate is equal to the mean transverse velocity of atoms divided by the mean path length across the light beam. However, the effect of the transit rate of atoms of different velocity groups across the beam is more complex [32]. The atoms with smaller transverse velocities spend more time in the light beam and thereby contribute more to the NMOR signal, narrowing the signal [32]. To take this effect into account, we introduced a parameter k_γ that modified the transit-relaxation rate

$$\gamma_g = k_\gamma \frac{v_{\mathrm{tr}}}{r}, \tag{3.16}$$

where $v_{\mathrm{tr}} = \sqrt{k_B T/m}$ is the mean transverse velocity, with m being the mass of the atom, T denoting the temperature, k_B being Boltzmann constant, and r being the beam radius, which in the cylindrical geometry of the experiment is the same as the average path across the beam. The parameter k_γ was determined by fitting the dispersion curve to the experimental data (Figure 3.5). The values of k_γ were different for different iris apertures but were kept constant for all light detunings and light intensities. When the beam diameter changes, it modifies the weight of the contribution of the atoms from different velocity groups, so it changes the width of the NMOR signal [32]. Table 3.1 shows the fitted values of k_γ for different iris apertures.

Rabi frequency is another parameter that needs to be determined to match the theoretical calculations with experimental signals. Although the Rabi frequency can be determined from the light intensity, the model needs to account for the fact that the light beam profile does not conform to a uniform, top-hat shape, and atoms traversing the beam experience different Rabi frequencies across the beam. This effect can be accounted for with a parameter k_R, which approximates the real beam profile as a top-hat profile, so that the Rabi frequency can be expressed as

$$\Omega_R = k_R \frac{dE_0}{\hbar}, \tag{3.17}$$

where $d = \langle J_g||d||J_e\rangle$ is electric dipole matrix element, $\hbar$ is reduced Planck's constant (which was set to $\hbar = 1$ in the derivation of the model) and E_0 is the amplitude of the electric field of the light, which can be extracted from expression for the light intensity

$$I = \frac{\epsilon_0 n c E_0^2}{2} \left[\frac{\text{mW}}{\text{cm}^2}\right], \tag{3.18}$$

where ϵ_0 is the electric constant, n is the refractive index and c is the speed of light.

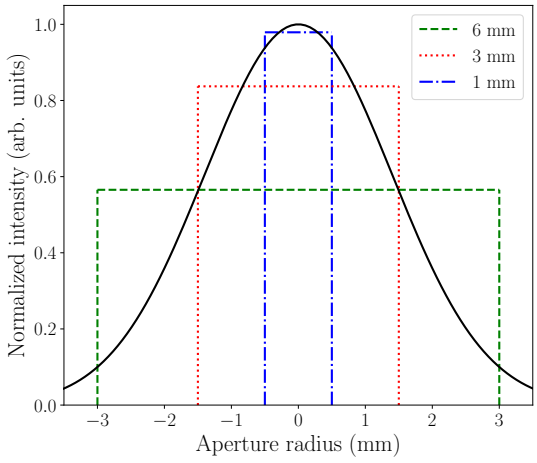

Figure 3.4: Schematic depiction of the laser-beam profile and the effect of the iris aperture on the light-intensity profile.

To estimate the parameter k_R we need to consider a light beam with a Gaussian profile

$$I(r') = I_0 e^{-\frac{2r'^2}{\sigma^2}}, \tag{3.19}$$

where I_0 is the maximum intensity at the center of the beam and σ is the radius of the beam before the iris, where the intensity drops by $1/e^2$. When the beam reaches the iris, the iris cuts the wings of the beam off, modifying the profile (Figure 3.4). The model does not include the effects of diffraction cause by the iris. The total light power then can be

expressed as

$$P = 2\pi I_0 \int_0^{R_a} r' e^{\frac{2r'^2}{\sigma^2}} dr' = 2\pi I_0 \frac{\sigma^2}{8}\left(e^{\frac{4R_a^2}{\sigma^2}} - 1\right), \tag{3.20}$$

where R_a is the radius of iris aperture. The top-hat beam intensity profile can be expressed as

$$P = I_1 \pi R_a^2, \tag{3.21}$$

where I_1 is the normalized light intensity. To use the top-hat intensity profile (3.21) instead of the real intensity distribution (3.20), we need to introduce a parameter k_R:

$$k_R = \sqrt{\frac{I_0}{I_1}} = \sqrt{\frac{4R_a^2}{\sigma^2\left(e^{\frac{4R_a^2}{\sigma^2}} - 1\right)}} \tag{3.22}$$

The parameter depends only on the iris diameter. It does not depend on laser power, so it is the same for all light intensities for given iris aperture radius. The beam radius before the iris was measured to be $\sigma = 2$ mm.

d (mm)	k_γ	k_R^{calc}	k_R^{exp}
1	0.17(1)	1.02	1.04(1)
3	0.23(2)	1.15	1.30(2)
6	0.42(7)	1.60	1.62(7)

Table 3.1: Calculated and fitted parameters k_γ and k_R for different iris aperture values.

Table 3.1 shows the calculated parameter k_R^{calc} (calculated numerically based on the beam profile and iris aperture) and fitted parameter k_R^{exp} (from the fitting of the dispersion curve to the experimental data) for different iris apertures. It can be seen that the values of the parameters depend on the beam diameter, which is determined by the iris opening, because the aperture size determines the profile of the beam. A maximally open aperture (6 mm) allows the atoms to interact with a beam that closely approximates a Gaussian profile, while an aperture of 1 mm changes the beam profile to something much closer to a top-hat profile. In the former case, when the actual beam profile strongly deviates from the uniform beam profile, the value of k_R is significantly larger than one, but in the latter case, when the beam profile is more closely approximated by a uniform intensity distribution, the value of k_R is nearly unity.

3.3 Results

The theoretical NMOR curves were calculated using the parameters k_γ and k_R (Table 3.1). Figure 3.5 compares the experimental data with the results of theoretical calculations.

Comparing the NMOR signal for the D_1 line (Figure 3.5a) and the NMOR signal measured with blue light (Figure 3.5b), it can be seen that both signals are centered around zero magnetic field and reveal a dispersive shape. The amplitude of rotation signal is defined as the maximum rotation. The width is defined as the magnetic-field difference between the maximum and minimum of the signal. The amplitude of the blue NMOR is 4 mrad and the width is 80 mG. The amplitude of the NMOR signal of the D_1 line is roughly five times larger, although the blue-light NMOR signal was measured at roughly 85°C, but the D_1-line signal was measured at room temperature (23°C), so that the vapor density was three orders of magnitude lower for the D_1-line measurement [29]. In both cases the laser intensity was the same (1.9 mW/cm^2 with an iris aperture of 1 mm) and the lasers were tuned to the same ground-state hyperfine level $F_g = 3$. The theoretical calculations were performed using parameters that correspond to the experimental temperature, the laser intensity and the iris aperture. The Rabi frequency for blue-light NMOR was $\Omega_R = 0.57$ MHz and for D_1-line NMOR was $\Omega_R = 3.6$ MHz. Although the intensity was the same for both transitions, the Rabi frequency was determined to be much smaller for blue-light excitation compared to D_1-line excitation. The reason for the different Rabi frequencies was the difference in the electric dipole moments $d = \langle J_g||d||J_e\rangle$ (3.17) of blue-light and D_1 the transitions. The difference in the degree of magnetic-field-induced anisotropy could make blue NMOR useful as a weakly perturbing probe.

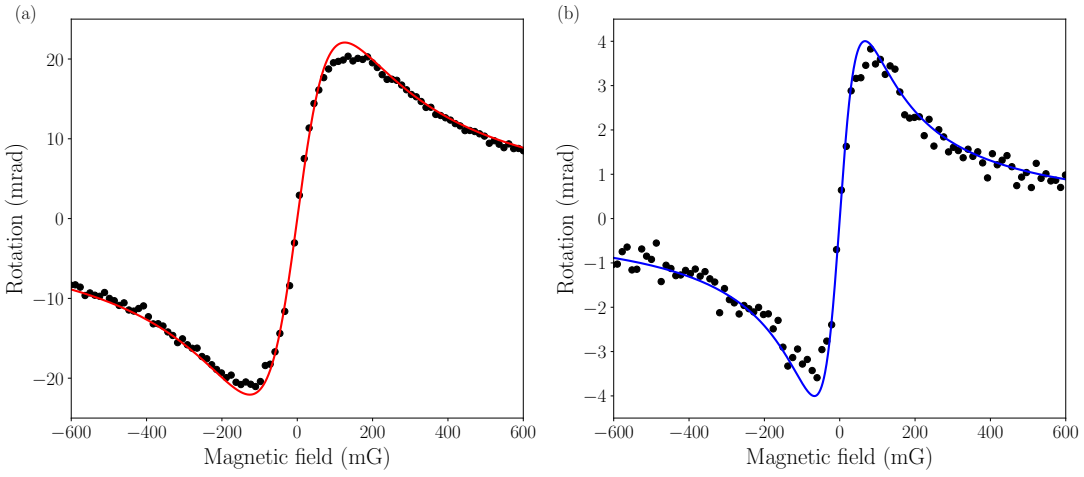

Figure 3.5: (a) Rotation of linearly polarized IR light tuned to the ^{85}Rb $F_g = 3 \longrightarrow F_e$ transition of the $5^2S_{1/2} \longrightarrow 5^2P_{1/2}$ (D_1) line. (b) Rotation of linearly polarized blue light tuned to the ^{85}Rb $F_g = 3 \longrightarrow F_e$ transition of the $5^2S_{1/2} \longrightarrow 6^2P_{1/2}$ line. The black dots are the experimental data and solid curves show the theoretical calculations for (a) $\Omega_R = 0.57$ MHz and (b) $\Omega_R = 3.6$ MHz. Note the differing vertical scales.

The advantages of the blue NMOR as a weakly perturbing probe can be manifested fully when we compare the widths of the resonances observed at the two transitions. The NMOR signal observed at the $5^2S_{1/2} \longrightarrow 5^2P_{1/2}$ transition (D_1 line) is nearly two times

broader than the one observed at the $5^2S_{1/2} \longrightarrow 6^2P_{1/2}$ transition. This difference is caused by power broadening, which dominates the resonance width at the D_1-line. A narrower signal leads to a more precise measurement.

3.3.1 NMOR Spectrum

Figure 3.6 depicts the dependence of blue-light rotation on the magnitude of the detuning from the resonance, illustrating a typical NMOR spectrum. The black dots represent the measured data at a magnetic field of 8 mG, where the signal is close to the maximum rotation, and at a light intensity of $\sim 0.1 \mathrm{mW/cm}^2$. The red solid curve is the calculated spectrum. The atoms from different velocity groups do not interact; therefore, the atoms from each of the velocity groups make an independent contribution to the signal. As a result, it is possible to calculate the theoretical signal by simply summing the contributions from atoms of different velocity groups (3.14). This approach was applied to calculating the NMOR spectra presented in Figure 3.6. As shown, the agreement of calculated spectra with the experimental data is good.

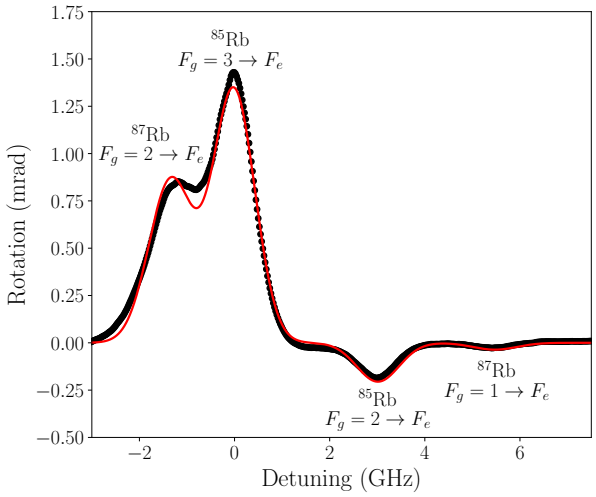

Figure 3.6: Experimental rotation spectra (black dots) measured at constant light intensity (0.1 $\mathrm{mW/cm}^2$) and theoretical rotation spectra (red curve) calculated at Rabi frequency $\Omega_R = 0.19$ MHz. The signals were obtained by scanning the frequency through all transitions of $5^2S_{1/2} \longrightarrow 6^2P_{1/2}$ line.

The strongest polarization rotation was observed for the $F_g = 3 \longrightarrow F_e$ of ^{85}Rb transition. The rotation for this transition was almost two times larger than the rotation amplitude of the second largest peak at the $F_g = 2 \longrightarrow F_e$ transition of ^{87}Rb. The ratio of rotation amplitudes at these two transitions is roughly the same as the ratio of absorption strengths at the same transitions, although the difference of Landé factors of ^{87}Rb and ^{85}Rb is $\frac{2}{3}$. The peaks in the spectrum correspond to different points in the NMOR signal. This means that the rotation amplitude of ^{87}Rb is already beyond

its maximum while the rotation of ^{85}Rb still increases with the magnetic field. Other transitions (the $F_g = 2 \longrightarrow F_e$ transition of ^{85}Rb and the $F_g = 1 \longrightarrow F_e$ of ^{87}Rb) produce much weaker signals. In this case, however, the difference in NMOR-signal amplitudes is much larger than the difference in the value of the absorption at the transitions. Moreover, due to the opposite signs of the Landé factors of the ground-state hyperfine levels, the direction of rotation at these transitions are reversed with respect to the stronger rotations of $F_g = 3 \longrightarrow F_e$ transition of ^{85}Rb and $F_g = 2 \longrightarrow F_e$ transition of ^{87}Rb.

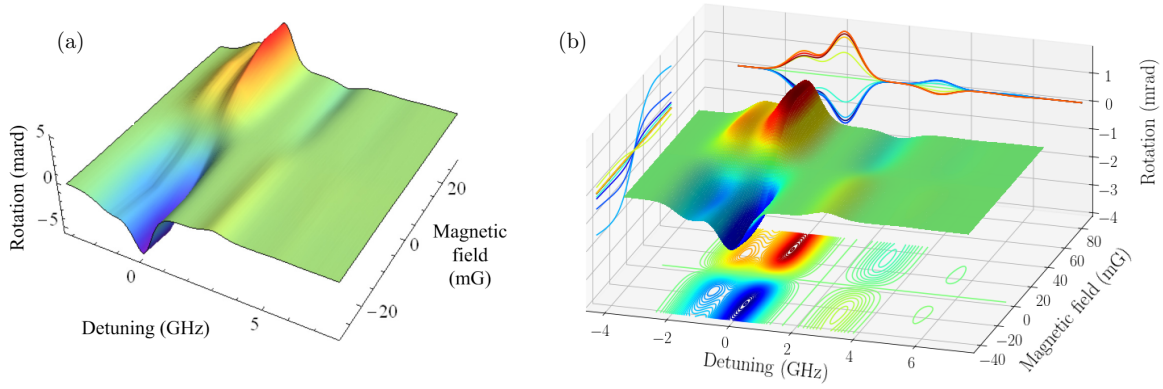

Figure 3.7: (a) Experimental rotation spectra for different magnetic fields measured at constant light intensity (0.1 mW/cm^2). The signals were obtained by scanning the frequency through all transitions of $5^2S_{1/2} \longrightarrow 6^2P_{1/2}$ line. (b) Theoretical rotation spectra for different magnetic fields, Rabi frequency $\Omega_R = 0.19$ MHz.

Figure 3.7 shows both experimental (Figure 3.7a) and theoretical (Figure 3.7b) 3D plots of spectral and magnetic-field dependence of the rotation. The experimental data and theoretical calculations confirm the analysis of Figure 3.6. It can be clearly seen that $F_g = 2 \longrightarrow F_e$ transition of ^{87}Rb reach the maximum of the rotation for lower magnetic field values than $F_g = 3 \longrightarrow F_e$ transition of ^{85}Rb.

3.3.2 Dependence of the NMOR signals on the light intensity

As an additional check on the theoretical model's ability to predict accurately the NMOR signals, as well as to test the understanding of the NMOR process, the dependence of the NMOR signals on the light intensity was studied. Figure 3.8a shows that the width of the blue NMOR signal does not depend on the light intensity. The data show that the width is also independent of hyperfine transition.

At the same time, the nonlinear character of NMOR implies that there should be a dependence of the amplitude of the signal on the light intensity. Figure 3.8b shows the amplitude of the blue NMOR signal versus the averaged light intensity for two transitions of ^{85}Rb: $F_g = 3 \longrightarrow F_e$ and $F_g = 2 \longrightarrow F_e$ (Figure 3.2). The amplitude dependence on the light intensity is different for these transitions because of the different dipole matrix

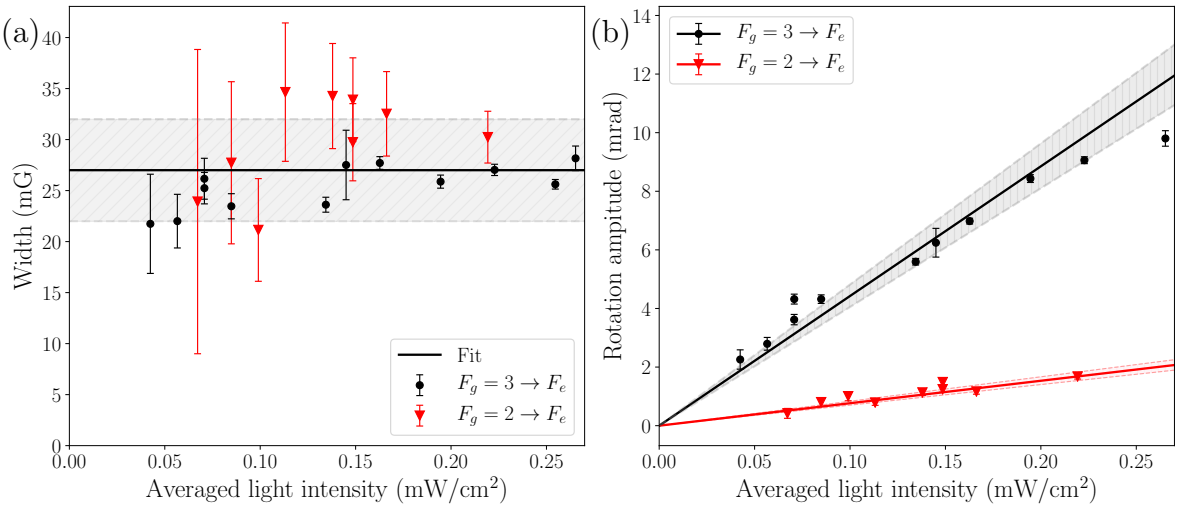

Figure 3.8: Dependence of the (a) width and (b) amplitude of rotation signals on light intensity for the transitions from the ground-state hyperfine level $F_g = 3$ (black points) and $F_g = 2$ (red triangles). The signals were measured at 85°C temperature with 6 mm beam diameter. The solid lines describe the theoretical calculations. The shaded areas mark the uncertainty of the parameter k_γ and k_R.

elements of the transitions. These differences are reproduced well by the model with the coefficient of determination $R^2 > 0.9$.

3.3.3 Influence of the beam diameter on the NMOR signals

The dependence of the rotation signal on beam diameter (Figure 3.9) was studied next with the goal of testing the reliability of the method and our theoretical model. The data of Figure 3.9 show the width and amplitude of the measured signal versus the average light intensity for different iris aperture sizes. The corresponding Rabi frequency ranges for the theoretical calculations were $0.48 - 1.19$ MHz for 1 mm, $0.15 - 0.43$ MHz for 3 mm and $0.12 - 0.31$ MHz for 6 mm beam diameter. The dependence of the amplitude on the average light intensity (Figure 3.9b) shows different slopes for the three iris apertures (3.7 ± 0.1 mrad(cm^2/mW) for 1 mm, 12.5 ± 0.4 mrad(cm^2/mW) for 3 mm and 22 ± 2 mrad(cm^2/mW) 6 mm openings). The different slopes arise from the fact that the ground-state relaxation rate is different in the three cases, and so the level of saturation of the transition also differs. Another factor that needs to be taken into account reproduce adequately the dependencies is that the different apertures result in different beam profiles (Figure 3.4), which we accounted for with the parameter k_R (Table 3.1). Combining these two contributions allows us to theoretically reproduce the experimental data with the coefficient of determination $R^2 > 0.9$.

The width of the rotation signal is independent on light intensity, but the width depends on the beam diameter (Figure 3.9a). Furthermore, the relation of the width to the

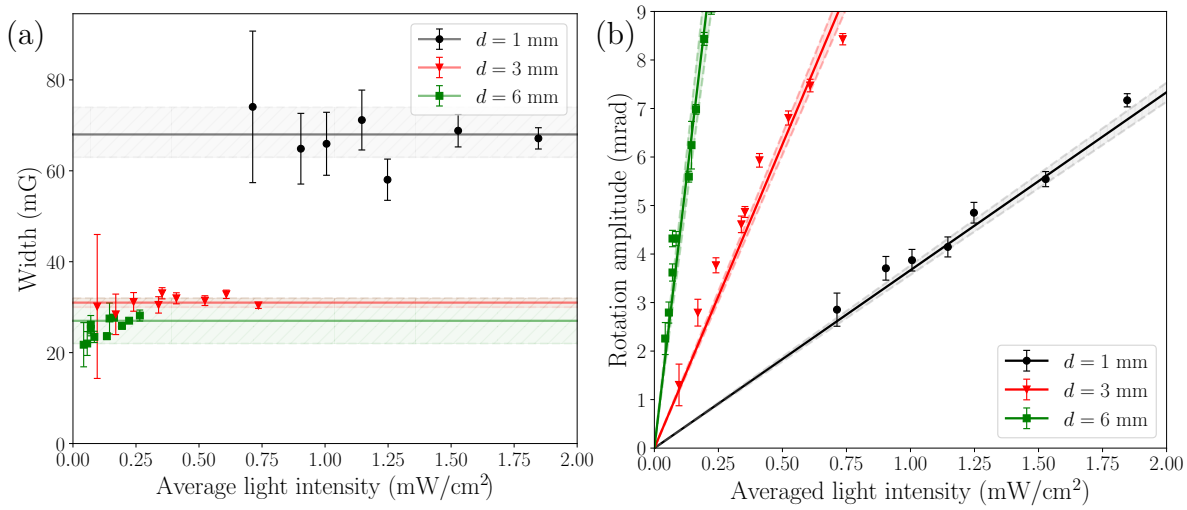

Figure 3.9: Dependence of the (a) width and (b) amplitude of rotation signals on the light intensity for different iris aperture sizes: 1 mm (black points), 3 mm (red triangles), 6 mm (green squares). The signals were measured for transitions from the ground-state hyperfine level $F_g = 3$ at 85°C temperature. The solid lines describe the theoretical calculations. The shaded areas mark the uncertainty of the parameter k_γ and k_R.

diameter of the iris opening is not straightforward. The experimentally determined widths for 3 mm and 6 mm iris openings are almost the same within the error bars (31 ± 1 mG for 3 mm and 27 ± 4 mG for 6 mm), but the width for the 1 mm iris opening is roughly two time larger (68 ± 5 mG). This effect is not related to the power broadening as the NMOR signal created by blue light is not power broadened, so this effect is related to the different dynamics of the optical pumping connected to the different beam diameters [32] and the different beam profiles (Figure 3.4). As the beam diameter is 4 mm, the iris apertures of 3 mm and 6 mm do not affect the light-intensity profile as much. The iris aperture of 6 mm lets through almost all of the beam and 3 mm cuts of just a little piece. There is a good agreement between experimental data and theoretical calculations after incorporation of these the effects.

3.4 Conclusions

The results of this chapter describe the nonlinear magneto-optical rotation at the $5^2S_{1/2} \longrightarrow 6^2P_{1/2}$ line. The dynamics of the excitation cycle for this transition differ from the D_1 or D_2 lines due to the decay of the excited atoms via several intermediate states. Nevertheless, a theoretical model was applied to this excitation transition that substituted the cascade relaxation transitions by one relaxation parameter, which characterized the direct transition to the ground state.

The theoretical model was adapted to the blue-light transition, taking into account

the experimental conditions and adjusting the parameters of the model accordingly. Due to the use of the iris to control the beam diameter in the experiment, the Rabi frequency Ω_R and ground state relaxation rate γ_g were estimated and adjusted using fitting parameters k_R and k_γ.

The theoretical model describes the experimental data, reproducing such characteristics as rotation amplitude, width and rotation spectrum for atoms in thermal motion in a vapor cell. These results are not obvious as in the atomic system only 15% of the atoms return to the ground state directly, while 85% return to the ground state through several intermediate states and thermalization on the walls of the cell.

The results provide not only fundamental understanding of NMOR induced by light that couples ground states with higher excited states but also indicate the possibility to use such an excitation scheme in magnetometry applications. For example, the weak absorption of the blue light in water could allow an application to remote underwater magnetometry [33].

Part II

Magneto-optical effects in nitrogen–vacancy centers in diamond

Chapter 4

Introduction to Part II

Nitrogen–vacancy (NV) centers in diamonds are point defects that consist of a substitutional nitrogen atom adjacent to a lattice vacancy. NV centers in diamond have been found to be versatile quantum sensors. The triplet ground state of the NV center can be optically polarized by exciting the NV center with green radiation for a short time [34–39]. The intensity of the subsequent, laser-induced red fluorescence depends on the polarization of the ground state. Moreover, the sublevel components with spin projection $m_S = \pm 1$ in an external magnetic field undergo Zeeman splitting, which makes the system inherently sensitive to magnetic field [40]. For a solid-state system, the ground-state magnetic sublevel manifold has a relatively long coherence time [41] that permits observations over experimentally interesting time scales, especially when enhanced by dynamic pulse techniques adapted from the field of nuclear magnetic resonance (NMR) [42, 43]. Being part of a crystal lattice, the NV center offers a scaleable system, from a single NV, to achieve maximum spatial resolution, to a macroscopic ensemble to enhance magnetic field sensitivity. Magnetic field sensitivities on the order of picoteslas have been achieved [44, 45]. NV centers have been used to image magnetic field distributions of microscopic magnetic structures [46–48], including in living cells [49]. Progress is being made to use NV centers to perform NMR experiments on picoliter volumes of analytes [43]. Other sensing modalities of NV centers include temperature and pressure [50].

Most of the applications of NV centers require knowledge of the detailed energy-level structure of the NV center, including the hyperfine structure, which arises from the interaction of the electron spin with the nuclear spin of the ^{14}N atom that is a part of the NV center. In Chapter 6 we analyze the hyperfine-level interaction at the magnetic field value that corresponds to the ground-state level anti-crossing (GSLAC), which leads to strong hyperfine level mixing and altering of the transition probabilities between magnetic sublevels of electron spin.

In this study optically detected magnetic resonance (ODMR) [51] signals were modeled to investigate the ground-state $m_S = 0 \longrightarrow m_S = +1$ and $m_S = 0 \longrightarrow m_S = -1$

electron spin transitions in the vicinity of the GSLAC. The model takes into account the mixing of the electron-spin state hyperfine levels to calculate the level structure and the transition strength between individual hyperfine levels. We also analyzed the influence of the slight misalignment between an external magnetic field and the axis of the NV center on the degree of spin polarization of the ^{14}N nucleus and the ODMR signal shape. The model also applied a Monte Carlo method to study the NV center's interaction with nearby ^{13}C nuclei, showing the influence of ^{13}C on ODMR signals. To test the model, we used a parameter-optimization procedure to fit the experimentally measured curves with the results of theoretical calculations.

The sensitivity of NV centers used as a probe could be dramatically enhanced if the surrounding nuclear spins could be polarized [52], a process referred to as hyperpolarization or dynamic nuclear polarization (DNP). The sensitivity could be enhanced even more if the spins on the surface of the diamond crystal or an adjacent substance could be polarized [53]. Success in achieving dynamic polarization of nuclei has been achieved near the excited-state level anti-crossing (ESLAC) around 512 G for single ^{15}N spins [54, 55], single ^{14}N and ^{15}N spins, and ensembles of ^{14}N and ^{13}C spins [56, 57]. The hyperfine interaction creates additional states which are strongly coupled near the level anticrossing. Previously the experimental signals in studies that measured nuclear spin polarization have been described successfully with models based on the master equation for the density matrix [55–57], combined with the Lindblad operator [58] or even simpler rate equations [54]. Nuclear polarization is very sensitive to any angular deviations of the magnetic field from the NV axis [54], which is important to take into account in any practical applications and useful as a signal for aligning the diamond crystal in the external magnetic field.

The nuclear spin polarization in the GSLAC magnetic field region has been studied much less in regard of nuclear spin polarization. Models have predicted that in the case of ^{15}N the polarization should fall as the magnetic field is increased from the ESLAC to the GSLAC, with a narrower peak at the GSLAC [55].

Chapter 7 analyzes the DNP for ^{14}N nuclear spin using numerical simulations based on the Lindblad equation over a wide range of magnetic field values, including both the ESLAC and GSLAC magnetic field regions. The results of the calculations show that the nuclear spin polarization decreases significantly if a transverse magnetic field or transverse strain field [59–63] are present. We also investigated the influence of pumping rate and relaxation rates on the nuclear spin polarization.

The model developed in Chapter 7 was tested using experimental ODMR signals, which were fitted using the model developed in Chapter 6 to determine the nuclear spin polarization. The experimentally determined DNP was compared with the results of the numerical calculations. The results show that nuclear spin polarization is especially sensitive to transverse magnetic field at the GSLAC, although a small dip in polarization

can also be observed at the ESLAC. The reason for observing a smaller signal at the ESLAC is that the ground-state hyperfine interaction is much weaker than the excited-state hyperfine interaction. The DNP enhancement at the GSLAC can be completely destroyed by the angle between the magnetic field direction and the axis of the NV center as small as 0.1°.

Chapter 5

Background

5.1 Physical structure of the NV center

A nitrogen-vacancy center is formed by substituting a nitrogen atom for a carbon atom in a diamond lattice next to a vacant position (Figure 5.1). The neutral NV^0 center is characterized by 5 valance electrons—three coming from dangling bonds of the three carbon atoms nearest to vacancy and two from the nitrogen dangling bonds. With one unpaired electron, the NV^0 center is a spin $\frac{1}{2}$ crystal-lattice defect. A more common form of NV center is the NV^- center, which contains two uncoupled electrons—an additional electron acquired from other nitrogen defects in the diamond lattice. The NV^- center has an electronic spin $S = 1$. In this work only the NV^- center will be analyzed. For further convenience, it will be referred as an NV center, without mentioning the charge state.

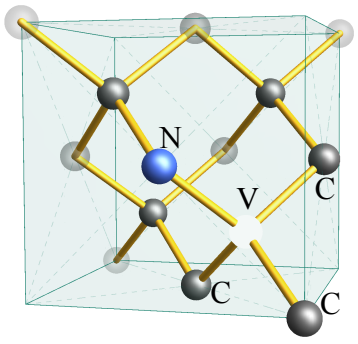

Figure 5.1: Diamond crystal with NV center

5.2 Energy structure of the NV center

NV centers have C_{3v} symmetry, which is equivalent to a symmetry under rotations by 120° around the axis running through the nitrogen and vacancy (Figure 5.2b). The C_{3v} symmetry axis of the NV center is also Z axis of the principal axes of the center. The

X and Y axis can then be chosen arbitrarily. The Z axis is also often chosen as the quantization axis, which will be the case in this work.

We can define six symmetry operations with respect to the quantization axis that connects the nitrogen atom and the vacancy (Figure 5.2b), forming a C_{3v} symmetry group:

- the identity operation ($\hat{E}$);
- two proper rotations by $\frac{2\pi}{3}$ and $\frac{4\pi}{3}$ ($\hat{C}_3$ and $\hat{C}_3^{-1}$);
- three reflections in the plane defined by the nitrogen atom, the vacancy, and one of the three carbon atoms ($\hat{\sigma}_i$).

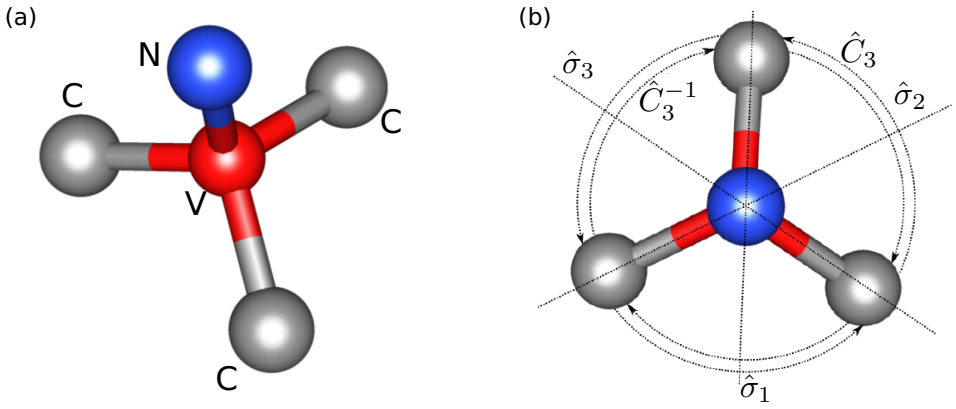

Figure 5.2: Symmetry of an NV center. (a) Nitrogen-vacancy center (carbon: gray, nitrogen: blue, vacancy: red). (b) Symmetry operations of the NV center.

The vacancy is assumed to have four dangling bonds that originate at any one of the carbon atoms or the nitrogen atom. These bonds can be labeled as $|c_1\rangle$, $|c_2\rangle$, $|c_3\rangle$, $|n\rangle$ and can be considered as atomic orbitals localized near the nuclear coordinates of the carbon and nitrogen atoms involved in the NV center. The transformation properties under the group symmetry operations are shown in table 5.1.

$\hat{R}_n$	$\hat{E}$	$\hat{C}_3$	$\hat{C}_3^{-1}$	σ_1	σ_2	σ_3
c_1	$\boldsymbol{c_1}$	c_2	c_3	$\boldsymbol{c_1}$	c_3	c_2
c_2	$\boldsymbol{c_2}$	c_3	c_1	c_3	$\boldsymbol{c_2}$	c_1
c_3	$\boldsymbol{c_3}$	c_1	c_2	c_2	c_1	$\boldsymbol{c_3}$
n	$\boldsymbol{n}$	$\boldsymbol{n}$	$\boldsymbol{n}$	$\boldsymbol{n}$	$\boldsymbol{n}$	$\boldsymbol{n}$
χ_n	4	1	1	2	2	2

Table 5.1: Symmetry operations of the orbital basis. Operations under which the orbitals are not changed are marked as bold. The last row shows the number of unchanged orbitals under a specific symmetry operation.

The NV center,formed by nitrogen and an adjacent vacancy in the diamond lattice, resembles a diatomic molecule. In order to find the corresponding molecular orbitals, we consider the irreducible representation of the C_{3v} symmetric group: the totally symmetric representation A_1, the anti-symmetric representation A_2 and the two-dimensional representation E. Using the projection operator and the characters of the C_{3v} symmetry operations, one can construct two orthogonal molecular orbitals that are totally symmetrical and transform as an irreducible representation A_1 and two that are mutually orthogonal and transform into each other as irreducible representation E:

$$|a_1\rangle = |n\rangle, \tag{5.1a}$$

$$|a_2\rangle = \frac{1}{\sqrt{3}}\left(|c_1\rangle + |c_2\rangle + |c_3\rangle\right), \tag{5.1b}$$

$$|e_x\rangle = \frac{1}{2}\left(2|c_1\rangle - |c_2\rangle - |c_3\rangle\right), \tag{5.1c}$$

$$|e_y\rangle = \frac{1}{\sqrt{2}}\left(|c_2\rangle - |c_3\rangle\right). \tag{5.1d}$$

The orbitals $|a_{1,2}\rangle$ are aligned along the quantization axis, while $|e_{x,y}\rangle$ are in the plane normal to the quantization axis (labels x and y are chosen arbitrarily). To draw an analogy to the familiar atomic orbitals of the hydrogen atom, we may say that $|a_1\rangle$ is an analogue of an s orbital, $|a_2\rangle$, of p_z, and $|e_{x,y}\rangle$, of $p_{x,y}$ orbitals. These orbitals are occupied by the six electrons of the NV center—one from each carbon atom, two from the nitrogen atom and one from the diamond lattice, given by a donor such as an additional nitrogen atom [1, 64, 65]. For the ground-state configuration, four electrons occupy the two symmetric orbitals, while the remaining two reside in the $|e_{x,y}\rangle$ orbitals (Figure 5.3). To simplify the description we may consider that two holes (which would be positively charged spin-1/2 particles) are distributed in the molecular orbitals. Thus, we may refer to the ground state of the NV center as e^2. For the excited state, one electron in $|a_2\rangle$ is promoted to the $|e_{x,y}\rangle$ levels, so that one hole is left in $|a_2\rangle$ and one in $|e\rangle$. Such a configuration can be denoted as ae.

In order to find spin states, we must construct the direct product of the basis states occupied by the two holes. From two states, we can construct three symmetrical and one anti-symmetrical direct-product, orbital-basis state. For the ground state we can express these states as:

$$|e_x\rangle \otimes |e_y\rangle = \begin{cases} |e_x e_x + e_y e_y\rangle \\ |e_x e_x - e_y e_y\rangle \\ |e_x e_y + e_y e_x\rangle \\ |e_x e_y - e_y e_x\rangle \end{cases}. \tag{5.2}$$

In the case of the first excited state, we will look at the product between $|a_2\rangle$ and

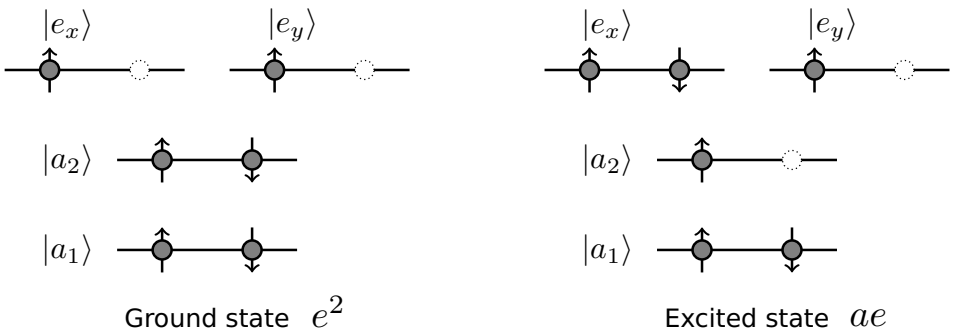

Figure 5.3: Molecular orbitals of the NV center. Gray circles represent electrons with the arrows indicating spin up or spin down. The dashed white circles represent holes.

$|e_x\rangle$ or $|e_y\rangle$

$$|a_2\rangle \otimes |e_y\rangle = \begin{cases} |ae_y + e_y a\rangle \\ |ae_y - e_y a\rangle \end{cases} \tag{5.3a}$$

$$|a_2\rangle \otimes |e_x\rangle = \begin{cases} |ae_x + e_x a\rangle \\ |ae_x - e_x a\rangle \end{cases} \tag{5.3b}$$

As there are two holes with two possible spin orientations, we may obtain similar direct product bases for the spin states:

$$|\uparrow\rangle \otimes |\downarrow\rangle = \begin{cases} |\uparrow\uparrow\rangle \\ |\downarrow\downarrow\rangle \\ |\uparrow\downarrow + \downarrow\uparrow\rangle \\ |\uparrow\downarrow - \downarrow\uparrow\rangle \end{cases} . \tag{5.4}$$

The first three basis states in (5.2) and (5.4) are symmetrical basis states and the last is anti-symmetrical.

Electrons (or holes) obey Fermi-Dirac statistics, so the total wavefunctions (and their basis states) must be anti-symmetrical. The resulting states are summarized in Table 5.2 [1].

5.2.1 Energy level structure of the NV center

The energy structure of an NV center's triplet state can be described by the total Hamiltonian

$$\hat{H}_{\mathrm{NV}} = \hat{H}_S + \hat{H}_{\mathrm{N}} + \hat{H}_B + \hat{H}_{\mathrm{strain}}, \tag{5.5}$$

where $\hat{H}_S$ is the fine-structure spin Hamiltonian, $\hat{H}_{\mathrm{N}}$ describes the hyperfine interaction between the electron spin of the NV center and the nuclear spin of the nitrogen atom

Configuration	State: Orbital	State: Spin	Notation
e^2 (T)	$\lvert e_x e_y - e_y e_x\rangle$	$\otimes \begin{cases} \lvert\downarrow\downarrow\rangle \\ \lvert\uparrow\downarrow + \downarrow\uparrow\rangle \\ \lvert\uparrow\uparrow\rangle \end{cases}$	${}^3A_{2-}$ (E_1) ${}^3A_{20}$ (A_1) ${}^3A_{2+}$ (E_2)
e^2 (S)	$\left.\begin{array}{l} \lvert e_x e_x - e_y e_y\rangle \\ \lvert e_x e_y + e_y e_x\rangle \\ \lvert e_x e_x + e_y e_y\rangle \end{array}\right\}$	$\otimes \lvert\uparrow\downarrow - \downarrow\uparrow\rangle$	${}^1E_1$ (E_1) ${}^1E_2$ (E_2) ${}^1A_1$ (A_1)
ae (T)	$\left.\begin{array}{l} \lvert a e_x - e_x a\rangle \\ \lvert a e_y - e_y a\rangle \end{array}\right\}$	$\otimes \begin{cases} \lvert\downarrow\downarrow\rangle \\ \lvert\uparrow\downarrow + \downarrow\uparrow\rangle \\ \lvert\uparrow\uparrow\rangle \end{cases}$	${}^3E$
ae (S)	$\left.\begin{array}{l} \lvert a e_x + e_x a\rangle \\ \lvert a e_y + e_y a\rangle \end{array}\right\}$	$\otimes \lvert\uparrow\downarrow - \downarrow\uparrow\rangle$	${}^1E$

Table 5.2: Structure of the ground (e^2) and first excited (ae) state orbital configuration of an NV color center [1].

associated with the NV center. $\hat{H}_B$ is the magnetic interaction Hamiltonian and $\hat{H}_{\text{strain}}$ describes the NV center's interaction with strain and the electric field.

The electronic energy-level structure of the NV center consists of a ground-state spin-1 triplet ${}^3A_2$, six excited state levels that form a two-fold triplet ${}^3E$ at room temperature, and two singlet states: ${}^1E$ and ${}^1A_1$ (Figure 5.4). As the current work is focused on NV centers at room temperature, we will not describe low-temperature effects of the NV center's excited-state levels [66].

The ground-state triplet is split by the spin-spin interaction between the two unpaired electrons. It causes the sublevels $m_S = 0$ and $m_S = \pm 1$ of the ground-state triplet to split by $D_g = 2.87$ GHz at zero magnetic field. The excited-state triplet sublevels are similarly split by $D_e = 1.41$ GHz. The excited state is separated from the ground state by 1.95 eV.

The fine-structure spin Hamiltonian of the NV center triplet ground state and excited state at room temperature can be written as [34, 67]

$$\hat{H}_S = \hat{\mathbf{S}}\hat{D}\hat{\mathbf{S}} = D\left[\hat{S}_z^2 - S\left(S+1\right)/3\right]. \tag{5.6}$$

Operators $\hat{S}_x$, $\hat{S}_y$ and $\hat{S}_z$ are the Cartesian components of the electron spin $S = 1$ operator

$$\hat{S}_z = \frac{1}{\sqrt{2}}\begin{pmatrix} 0 & 1 & 0 \\ 1 & 0 & 1 \\ 0 & 1 & 0 \end{pmatrix}, \quad \hat{S}_y = \frac{i}{\sqrt{2}}\begin{pmatrix} 0 & -1 & 0 \\ 1 & 0 & -1 \\ 0 & 1 & 0 \end{pmatrix}, \quad \hat{S}_z = \begin{pmatrix} 1 & 0 & 0 \\ 0 & 0 & 0 \\ 0 & 0 & -1 \end{pmatrix}. \tag{5.7}$$

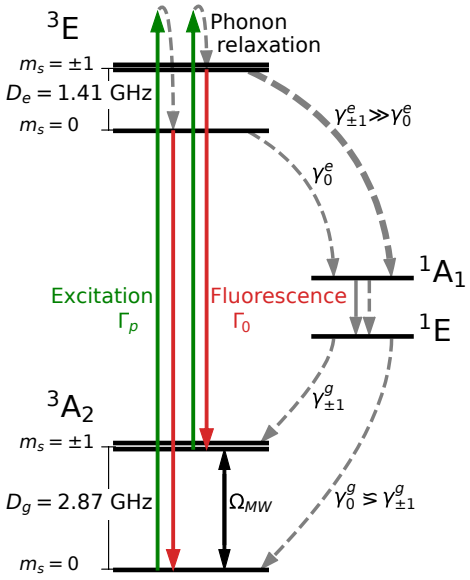

Figure 5.4: Nitrogen-Vacancy center energy-level structure

The parameter $D = D_g = 2.87$ GHz [59] characterizes the zero-field splitting between sublevels in the ground state and $D = D_e = 1.41$ GHz [59] in the excited state.

5.2.2 Hyperfine structure of the NV center

In order to describe fully the level structure of nitrogen-vacancy centers, their interactions with nearby nuclear spins must be considered. In all cases, the nucleus of the nitrogen atom associated with the NV center interacts with the NV electron spin. The vast majority (99.6%) of these nitrogen nuclei are ^{14}N whose nuclear spin is $I = 1$. The Hamiltonian of the ^{14}N nuclear-spin interaction with the electron spin can be written as

$$\begin{aligned} \hat{H}_{\mathrm{N}} &= Q\hat{I}_z^2 + \hat{\mathbf{S}} \cdot \bar{A} \cdot \hat{\mathbf{I}} \\ &= Q\hat{I}_z^2 + A_{\parallel}\hat{S}_z\hat{I}_z + A_{\perp}\left(\hat{S}_x\hat{I}_x + \hat{S}_y\hat{I}_y\right), \end{aligned} \tag{5.8}$$

where $Q = -4.96$ MHz [42] is the nuclear-spin quadrupole interaction parameter and $\bar{A}$ is the hyperfine interaction tensor

$$\bar{A} = \begin{pmatrix} A_{\perp} & 0 & 0 \\ 0 & A_{\perp} & 0 \\ 0 & 0 & A_{\parallel} \end{pmatrix}, \tag{5.9}$$

where $A_{\parallel}$ and $A_{\perp}$ are axial and non-axial hyperfine interaction parameters. In the ground state the values of the parameters are $A^g_{\parallel} = -2.14$ MHz and $A^g_{\perp} = -2.70$ MHz [42]. In the excited state the hyperfine interaction is stronger with the hyperfine interaction parameters being $A^e_{\parallel} = -40$ MHz and $A^e_{\perp} = -23$ MHz [57]. The hyperfine interaction splits each of the electron Zeeman sublevels into 3 levels, so that the ground-state and excited-state triplet systems can be characterized as a 9-state system (Figure 5.5)

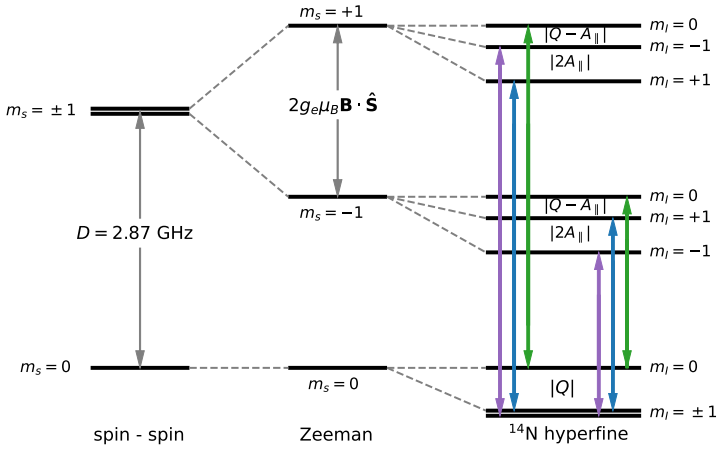

Figure 5.5: Nitrogen-Vacancy center energy level structure

5.2.3 NV center interaction with a magnetic field

The work presented in this thesis exploits the fact that the NV center in diamond exhibit magnetically sensitive energy levels. The ground-state levels are shifted in the magnetic field due to Zeeman interaction. The Hamiltonian of the NV-center interaction with a magnetic field pointed in an arbitrary direction with respect to the NV-center axis can be expressed as [63]

$$\begin{aligned}\hat{H}_B &= g_e\mu_B\mathbf{B}\cdot\hat{\mathbf{S}} - g_I\mu_N\mathbf{B}\cdot\hat{\mathbf{I}} \\ &= g_e\mu_B\left(B_xS_x + B_yS_y + B_zS_z\right) - g_I\mu_N\left(B_xI_x + B_yI_y + B_zI_z\right),\end{aligned} \tag{5.10}$$

where the magnetic field is expressed in Cartesian coordinates in the NV center's principal axis $\mathbf{B} = (B_x, B_y, B_z)$, $g_e = -2.0023$ and $g_I = 0.4037$ are Landé g-factors of an electron and nucleus of ^{14}N and $\mu_B = 1.4$ MHz/G and $\mu_N = 0.76$ kHz/G are the Bohr and the nuclear magnetons. The magnetic field's Cartesian components can be expressed using the angles between the magnetic field's direction and the NV center's principal axis:

$$B_x = B\cdot\sin\theta\cdot\cos\varphi \tag{5.11a}$$

$$B_y = B\cdot\sin\theta\cdot\sin\varphi \tag{5.11b}$$

$$B_z = B\cdot\cos\theta. \tag{5.11c}$$

Due to C_{3v} symmetry the φ can be chosen arbitrarily, e.g., $\varphi = 0$. Leaving one parameter for the magnetic field direction with respect to the NV center's axis $\mathbf{B} = (B\sin\theta, 0, B\cos\theta)$. The Hamiltonian for the interaction between the magnetic field and the electronic spin can be expressed explicitly as

$$g_e\mu_B\mathbf{B}\cdot\hat{\mathbf{S}} = g_e\mu_B\begin{pmatrix} B\cos\theta & \frac{B\sin\theta}{\sqrt{2}} & 0 \\ \frac{B\sin\theta}{\sqrt{2}} & 0 & \frac{B\sin\theta}{\sqrt{2}} \\ 0 & \frac{B\sin\theta}{\sqrt{2}} & -B\cos\theta \end{pmatrix}. \tag{5.12}$$

The interaction between the magnetic field and the nuclear spin $g_I \mu_N \mathbf{B} \cdot \hat{\mathbf{I}}$ can be expressed explicitly in the same way.

5.2.4 NV center interaction with strain

The NV center's electron spin also interacts with crystal stress which is associated with strain and with electric field [63]. As the the strain and electric field terms take the same form, we do not explicitly express the electric field interaction with the electron spin. Consequently, further we consider parameters that do not distinguish between electric field and strain interaction. Assuming that the electric field interaction is small, we refer to the strain and electric field interaction with the electron spin as a strain interaction. The strain Hamiltonian can be expressed as

$$\begin{aligned} \hat{H}_{\text{strain}} = M_z S_z^2 + M_x \left(\hat{S}_x^2 - \hat{S}_y^2 \right) + M_y \left(\hat{S}_x \hat{S}_y + \hat{S}_y \hat{S}_x \right) \\ + N_x \left(\hat{S}_x \hat{S}_z + \hat{S}_z \hat{S}_x \right) + N_y \left(\hat{S}_y \hat{S}_z + \hat{S}_z \hat{S}_y \right), \end{aligned} \tag{5.13}$$

where M_z, M_x, M_y, N_x, N_y are coupling constants [60–62], showing how strain couples different electron spin states. At low magnetic fields < 10 G, terms M_x and M_y couple states $m_S = +1$ and $m_S = -1$, causing a splitting between these states. For larger magnetic field values, these terms are negligible, as the Zeeman effect causes level spitting significantly larger than the coupling rates. If the applied magnetic field reaches the level crossing points, the components N_x and N_y coupling the magnetic sublevels $m_S = 0$ and $m_S = -1$ start to influence the interaction of the states. The strain induced interaction strength between electron spin states in the ground state is on the order of few megahertz and in the excited-state is a few tenths of a megahertz [59, 68].

5.2.5 Optical polarization of the electron spin of the NV center

Optical excitation can be used both to prepare the spin state and to read out the polarization state of an NV center. Electric dipole transitions with subsequent phonon relaxation are spin conserving $\Delta m_S = 0$ (Figure 5.4). It means that both laser excitation transitions (green arrows in Figure 5.4) and fluorescence transitions (red arrows in Figure 5.4) do not change the spin projection state. The NV center is excited with a green-light laser that excites the phonon band of the ^3E state, followed by fast phonon relaxation.

The ^3E excited state then can spontaneously decay back to the $^3A_2$ ground state, emitting fluorescent light. In this channel all of the magnetic sublevels $m_S = 0, \pm 1$ decay with equal probabilities. The other relaxation path of the ^3E state is through nonradiative intersystem crossing to a singlet state $^1A_1$ (dashed lines in Figure 5.4). In this channel the transitions from $m_S = \pm 1$ sublevels are more probable, leading a transition rate around 5 times faster than from the $m_S = 0$ sublevel. The singlet state $^1A_1$ is short lived

($\sim$ 1ns [69]), decaying to the ^1E singlet state via a nonradiative transition or infrared fluorescence. The nonradiative transitions of the intersystem crossing from the ^1E singlet state to the $^3A_2$ triplet ground state have similar transition rates for the $m_S = 0$ and $m_S = \pm 1$ sublevels, with a slightly higher possibility of transitions to the $m_S = 0$ sublevel ($\gamma_0^g \approx 1$ MHz and $\gamma_{\pm 1}^g \approx 0.7$ MHz [69]). After a few optical cycles the difference of intersystem crossing rates between the ^3E sublevels $m_S = 0$ and $m_S = \pm 1$ leads to ground-state electronic spin polarization of the $m_S = 0$ level.

5.2.6 Nuclear spin polarization process

Usually the nuclear spin is difficult to polarize at room temperature because of the small splitting of the hyperfine levels. The methods of achieving high nuclear-spin polarization include low temperatures or using a selective microwave excitation in combination with controlled Larmor precession of the nuclear-spin state [70]. Electron-spin polarization can be also transferred to nuclear spin using a level anti-crossing (LAC) in the ground state (GSLAC) or excited state (ESLAC) [54, 56].

At the magnetic field value that corresponds to a level anticrossing (≈510 G in the excited state (ES) and ≈1025 G in the ground state (GS)), the energy difference between magnetic sublevels $m_S = -1$ and $m_S = 0$ is reduced, and the hyperfine interaction mixes the $|m_S = 0, m_I = -1\rangle$ state with $|m_S = -1, m_I = 0\rangle$ and the $|m_S = 0, m_I = 0\rangle$ state with $|m_S = -1, m_I = +1\rangle$.

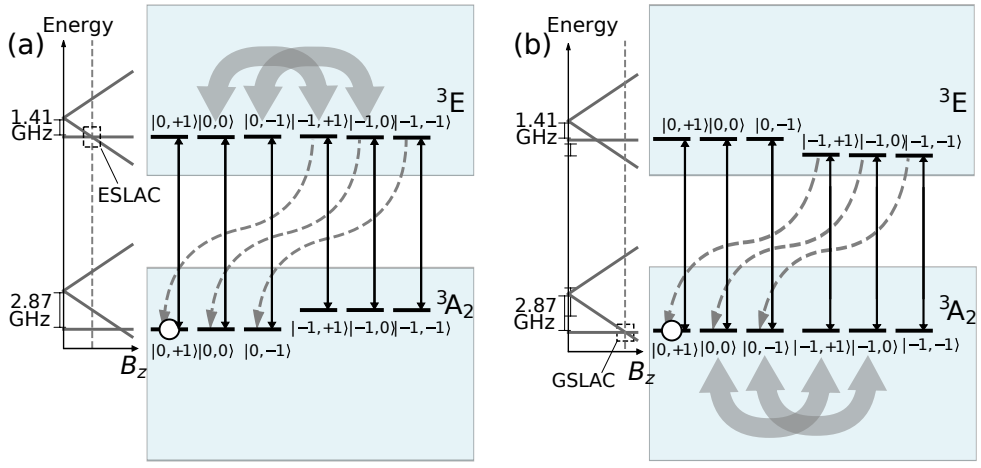

Figure 5.6: (a) Nuclear-spin polarization process at the ESLAC. (b) Nuclear-spin polarization process at the GSLAC.

Figure 5.6 shows a nuclear-spin polarization scheme. The solid arrows describe the direct transitions between the ground and excited states, the dashed arrows show the nonradiative intersystem crossing transitions, and the wide, gray arrows describe the mixing between hyperfine levels. After several cycles of continous optical excitation and

nonradiative decay, the population is accumulated in the state $|m_S = 0, m_I = 1\rangle$, which stays unmixed at all times.

Assuming that the electron spin has been already polarized by the interaction with laser radiation (all of the population is accumulated in the $m_s = 0$ magnetic sublevel, see Section 5.2.5), the nuclear-spin polarization can be described using the following analysis:

1. Emptying the $|0, -1\rangle$ ground state sublevel:
   GS $|0, -1\rangle \xrightarrow{\text{laser excitation}}$ ES $|0, -1\rangle \xrightarrow{\text{mixing}}$ ES $|-1, 0\rangle \xrightarrow{\text{spontaneous decay}}$ GS $|0, 0\rangle$
2. Emptying the $|0, 0\rangle$ ground state sublevel:
   GS $|0, 0\rangle \xrightarrow{\text{laser excitation}}$ ES $|0, 0\rangle \xrightarrow{\text{mixing}}$ ES $|-1, 1\rangle \xrightarrow{\text{spontaneous decay}}$ GS $|0, 1\rangle$
3. Leaving population in the $|0, 1\rangle$ ground state sublevel (no mixing):
   GS $|0, 1\rangle \xrightarrow{\text{laser excitation}}$ ES $|0, 1\rangle \xrightarrow{\text{spontaneous decay}}$ GS $|0, 1\rangle$

The polarization process is similar for excited- and ground-state level mixing. External influences, such as a transverse magnetic field B_x (5.10) or transverse strain N_x (5.13) cause additional level mixing so that the $|m_S = 0, m_I = 1\rangle$ sublevel is also mixed, and nuclear-spin polarization decreases. The ground-state hyperfine interaction is much weaker than the excited-state hyperfine interaction (5.9), so that these external processes have a stronger influence on nuclear spin polarization at the GSLAC compared to the ESLAC.

5.3 A method to examine the energy-level structure in NV centers: ODMR

Applying a microwave (MW) field that is in resonance with the ground-state $m_S = 0 \longrightarrow m_S = -1$ or $m_S = 0 \longrightarrow m_S = 1$ transition, the population can be transferred from $m_S = 0$ to $m_S = -1$ or $m_S = 1$ sublevels. To prepare states or read them out more precisely, different pulse sequences can be used. Nevertheless, in some cases the best approach is to apply continuous-wave (CW) field [71]. The experimental results used to test the models in the following chapters have been obtained with CW microwave radiation (see A.2).

Fluorescence can be used to read the ground-state spin polarization of the NV center. If the population is transferred to the ground state magnetic sublevels $m_S = \pm 1$, the fluorescence intensity drops because the nonradiative transition of the $m_S = \pm 1$ excited-state sublevel is more probable than for the $m_S = 0$ sublevel.

By scanning MW frequency, we can observe a decrease in fluorescence intensity, when the MW frequency is on resonance with a magnetic dipole transition between ground state magnetic sublevels. The achieved signals are called optically detected magnetic resonance (ODMR).

Chapter 6

Modeling ODMR signals in the presence of an external magnetic field

Most applications of NV centers require knowledge of the detailed energy-level structure of the NV center, including hyperfine structure, caused by the interaction of the electron spin with the nuclear spin.

This chapter is dedicated to analyzing the hyperfine structure and level mixing at magnetic field values near the GSLAC. Due to the level mixing in the vicinity of the GSLAC, the transition probabilities between electronic and hyperfine levels are altered. In order to support experimental studies of the hyperfine level structure and transition probabilities at the GSLAC, the ODMR signals were modeled to investigate the ground state $m_s = 0 \longrightarrow m_s = +1$ and $m_s = 0 \longrightarrow m_s = -1$ electron-spin transition manifolds.

The modeling was done by calculating the frequencies and the probabilities of microwave-field-induced transitions between electron-spin states. We investigated the influence of the magnetic field misalignment on the ODMR signals at the GSLAC as well. The impact of the transverse magnetic field is apparent especially for the low-frequency microwave-field range ($m_s = 0 \longrightarrow m_s = -1$ transition manifold). We also analyzed the dependence of the ODMR signal shape on nuclear-spin polarization and the width of the signal. To model the ODMR signals of an ensemble of NV centers, we added the interaction of the ^{13}C atoms in the diamond lattice with the NV center, with the interaction strength dependent on its position in the lattice. The experimental signals were used to test the calculations. The experiment was done by Reinis Lazda, Andris Berzins and Huijie Zheng and is not a part of the dissertation. The experimental setup is described in Appendix A.2. However, the data analysis and fitting procedure was developed as a part of the dissertation. To fit the experimental data with the results of theoretical calculation, we used a parameter-optimization procedure. The fitting procedure allowed

us to determine the nuclear-spin polarization as well as the average angle between the magnetic field direction and NV center's axis.

The results described in this chapter are published in [71] and [72].

6.1 NV centers in an external magnetic field

If the magnetic field is applied along the NV axis (B_z in (5.10)), the energy change of magnetic sublevels can be described by the linear Zeeman effect:

$$E_{m_S} = \gamma_e m_S B_z. \tag{6.1}$$

Thus, the energy of the $m_S = 0$ sublevel does not change, the energy of the $m_S = +1$ sublevel increases, and the energy of the $m_S = -1$ sublevel decreases in the magnetic field B_z with a constant of proportionality $\gamma_e = g_e \mu_B$.

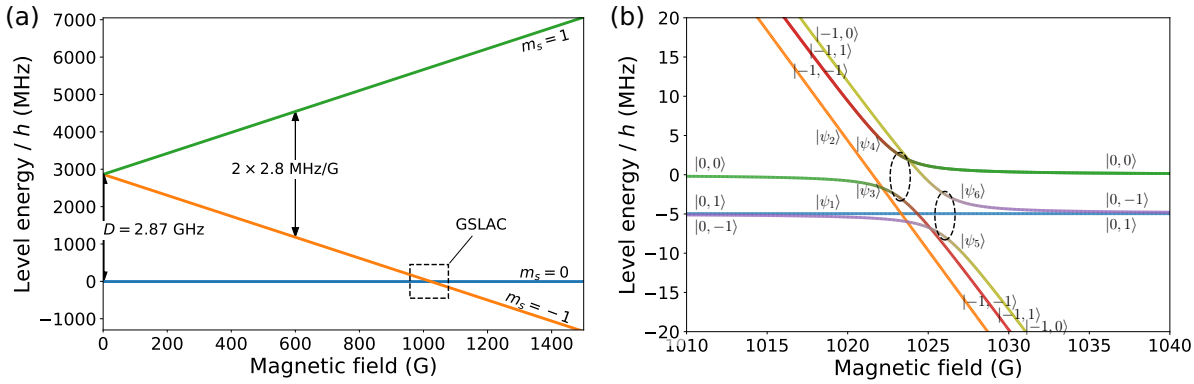

Figure 6.1: Ground-state sublevels in a magnetic field B_Z applied along the NV axis. (a) Level crossing of electron-spin magnetic sublevels in the ground state. (b) Hyperfine level ($|m_S, m_I\rangle$) anticrossing in the vicinity of the GSLAC. The level of mixing near the GSLAC (denoted by the dashed ellipses) is indicated by the relative admixture of the colors in each curve; the lines corresponding to unmixed states do not change color.

6.1.1 Hyperfine-level mixing of the ground-state level anti-crossing

A crossing between magnetic sublevels $m_S = 0$ and $m_S = -1$ of the ground electronic state occurs when the Zeeman splitting at a magnetic field value of $B_z = D_g/g_e\mu_B = 1024$ G compensates the zero-field splitting (Figure 6.1a). Owing to the hyperfine interaction, some of the hyperfine energy levels exhibit avoided crossings (Figure 6.1b). This effect is called the ground-state level anti-crossing (GSLAC). If the nuclear-spin interaction with magnetic field is ignored, the ground-state Hamiltonian (5.5) can be written as

$$\hat{H}_g = D\hat{S}_z^2 + \gamma_e B_z \hat{S}_z + A_\parallel \hat{S}_z \hat{I}_z + A_\perp \left(\hat{S}_x \hat{I}_x + \hat{S}_y \hat{I}_y\right) + Q\hat{I}_z^2, \tag{6.2}$$

and in matrix form it can be written as

$$\hat{H}_g = \left(\begin{array}{ccc:ccc:ccc} \eta_+ + A_\parallel + \beta & 0 & 0 & 0 & 0 & 0 & 0 & 0 & 0 \\ 0 & D+\beta & 0 & \textcircled{$A_\perp$} & 0 & 0 & 0 & 0 & 0 \\ 0 & 0 & \eta_+ - A_\parallel + \beta & 0 & \textcircled{$A_\perp$} & 0 & 0 & 0 & 0 \\ \hdashline 0 & \textcircled{$A_\perp$} & 0 & Q & 0 & 0 & 0 & 0 & 0 \\ 0 & 0 & \textcircled{$A_\perp$} & 0 & 0 & 0 & A_\perp & 0 & 0 \\ 0 & 0 & 0 & 0 & 0 & Q & 0 & A_\perp & 0 \\ \hdashline 0 & 0 & 0 & 0 & A_\perp & 0 & \eta_+ - A_\parallel - \beta & 0 & 0 \\ 0 & 0 & 0 & 0 & 0 & A_\perp & 0 & D-\beta & 0 \\ 0 & 0 & 0 & 0 & 0 & 0 & 0 & 0 & \eta_+ + A_\parallel - \beta \end{array}\right), \tag{6.3}$$

where $\eta_+ = D + Q$, $\eta_- = D - Q$ and $\beta = \gamma_e B_Z$. The operator $\hat{H}_g$ (6.3) is written in the uncoupled basis $|m_S\ m_I\rangle$ with elements in the order $|1\ 1\rangle$, $|1\ 0\rangle$, $|1\ -1\rangle$, $|0\ 1\rangle$, $|0\ 0\rangle$, $|0\ -1\rangle$, $|-1\ 1\rangle$, $|-1\ 0\rangle$, $|-1\ -1\rangle$.

At the GSLAC, the mixing of the $m_S = 0$ and $m_S = -1$ ground-state sublevels is caused by the non-axial term $A_\perp$ of the hyperfine tensor $\bar{A}$. As the $m_S = +1$ sublevel at the GSLAC is separated by an energy corresponding to 5740 MHz from the $m_S = 0$ and $m = -1$ sublevels, the interaction between the $m_S = 0$ and $m_S = +1$ basis states can be ignored as the interaction strength is much smaller than the splitting between $m_S = 0$ and $m_S = +1$. The respective terms (circled) in the Hamiltonian 6.3 are set to zero, leading to a matrix that effectively consists of two independent parts: the upper left block, which describes the hyperfine levels of the $m_S = +1$ sublevel and the middle-to-lower right block, which describes the hyperfine levels of the $m_S = 0$ and $m_S = -1$ sublevels.

$$\hat{H}_g(\text{GSLAC}) = \left(\begin{array}{ccc:ccc:ccc} \eta_+ + A_\parallel + \beta & 0 & 0 & 0 & 0 & 0 & 0 & 0 & 0 \\ 0 & D+\beta & 0 & \textcircled{0} & 0 & 0 & 0 & 0 & 0 \\ 0 & 0 & \eta_+ - A_\parallel + \beta & 0 & \textcircled{0} & 0 & 0 & 0 & 0 \\ \hdashline 0 & \textcircled{0} & 0 & Q & 0 & 0 & 0 & 0 & 0 \\ 0 & 0 & \textcircled{0} & 0 & 0 & 0 & A_\perp & 0 & 0 \\ 0 & 0 & 0 & 0 & 0 & Q & 0 & A_\perp & 0 \\ \hdashline 0 & 0 & 0 & 0 & A_\perp & 0 & \eta_+ - A_\parallel - \beta & 0 & 0 \\ 0 & 0 & 0 & 0 & 0 & A_\perp & 0 & D-\beta & 0 \\ 0 & 0 & 0 & 0 & 0 & 0 & 0 & 0 & \eta_+ + A_\parallel - \beta \end{array}\right), \tag{6.4}$$

Using a modified Hamiltonian for magnetic field values corresponding to the GSLAC (6.4), approximate eigenvalues and eigenvectors of the hyperfine states can be calculated ana-

lytically. The energies E_i of these states are

$$E_1 = Q, \tag{6.5a}$$
$$E_2 = \eta_+ + A_\parallel - \beta, \tag{6.5b}$$
$$E_3 = \frac{1}{2}\left(\eta_+ - A_\parallel - \beta - \sqrt{(2A_\perp)^2 + (\eta_+ - A_\parallel - \beta)^2}\right), \tag{6.5c}$$
$$E_4 = \frac{1}{2}\left(\eta_+ - A_\parallel - \beta + \sqrt{(2A_\perp)^2 + (\eta_+ - A_\parallel - \beta)^2}\right), \tag{6.5d}$$
$$E_5 = \frac{1}{2}\left(\eta_+ - \beta - \sqrt{(2A_\perp)^2 + (\eta_+ - \beta)^2}\right), \tag{6.5e}$$
$$E_6 = \frac{1}{2}\left(\eta_+ - \beta + \sqrt{(2A_\perp)^2 + (\eta_+ - \beta)^2}\right), \tag{6.5f}$$
$$E_7 = \eta_+ + A_\parallel + \beta, \tag{6.5g}$$
$$E_8 = \eta_+ - A_\parallel + \beta, \tag{6.5h}$$
$$E_9 = D + \beta. \tag{6.5i}$$

The respective wave functions can be written in the uncoupled basis $|m_S, m_I\rangle$ as follows:

$$|\psi_1\rangle = |0,1\rangle, \tag{6.6a}$$
$$|\psi_2\rangle = |-1,-1\rangle, \tag{6.6b}$$
$$|\psi_3\rangle = \frac{1}{|\alpha_1^+|}|-1,1\rangle - \frac{1}{|\alpha_1^+|}\left(\kappa_1 + \sqrt{\kappa_1^2+1}\right)|0,0\rangle, \tag{6.6c}$$
$$|\psi_4\rangle = \frac{1}{|\alpha_1^-|}|-1,1\rangle - \frac{1}{|\alpha_1^-|}\left(\kappa_1 - \sqrt{\kappa_1^2+1}\right)|0,0\rangle, \tag{6.6d}$$
$$|\psi_5\rangle = \frac{1}{|\alpha_2^+|}|-1,0\rangle - \frac{1}{|\alpha_2^+|}\left(\kappa_2 + \sqrt{\kappa_2^2+1}\right)|0,-1\rangle, \tag{6.6e}$$
$$|\psi_6\rangle = \frac{1}{|\alpha_2^-|}|-1,0\rangle - \frac{1}{|\alpha_2^-|}\left(\kappa_2 - \sqrt{\kappa_2^2+1}\right)|0,-1\rangle, \tag{6.6f}$$
$$|\psi_7\rangle = |1,1\rangle, \tag{6.6g}$$
$$|\psi_8\rangle = |1,-1\rangle, \tag{6.6h}$$
$$|\psi_9\rangle = |1,0\rangle, \tag{6.6i}$$

where

$$\kappa_1 = \frac{\eta_+ - A_\parallel - \gamma_e B}{2A_\perp}, \tag{6.7a}$$
$$\kappa_2 = \frac{\eta_- - \gamma_e B}{2A_\perp} \tag{6.7b}$$

and

$$|\alpha_{1,2}^\pm| = \sqrt{\left(\kappa_{1,2} \pm \sqrt{\kappa_{1,2}^2+1}\right)^2 + 1}. \tag{6.8}$$

It can be seen that only basis states with equal $m_S + m_I$ are mixed at GSLAC. Anticrossing occurs between two pairs of states. One pair consists of states $|\psi_3\rangle$ and $|\psi_4\rangle$,

the other of states $|\psi_5\rangle$ and $|\psi_6\rangle$. The states $|\psi_1\rangle = |0,1\rangle$ and $|\psi_2\rangle = |-1,-1\rangle$ do not mix at the GSLAC.

From the wave functions (6.6), we can determine the exact magnetic field value at which the strongest mixing happens. For levels $|\psi_3\rangle$ and $|\psi_4\rangle$ anticrossing appears when $\kappa_1 = 0$, which implies a magnetic field value $B = \frac{1}{\gamma_e}\left(D_g + Q - A_\parallel\right) = 1023.08$ G. At this point the wave functions of these states are

$$|\psi_3\rangle = \frac{1}{\sqrt{2}}|-1,1\rangle - \frac{1}{\sqrt{2}}|0,0\rangle \tag{6.9a}$$

$$|\psi_4\rangle = \frac{1}{\sqrt{2}}|-1,1\rangle + \frac{1}{\sqrt{2}}|0,0\rangle \ . \tag{6.9b}$$

The second anticrossing is between states $|\psi_5\rangle$ and $|\psi_6\rangle$. Similarly, we can determine the exact magnetic field at which the strongest mixing happens. In this case it is $\kappa_2 = 0$, which leads to a magnetic field value of $B = \frac{1}{\gamma_e}(D_g - Q) = 1025.86$ G. And the wave functions of these states at the anticrossing are

$$|\psi_5\rangle = \frac{1}{\sqrt{2}}|-1,0\rangle - \frac{1}{\sqrt{2}}|0,-1\rangle \tag{6.10a}$$

$$|\psi_6\rangle = \frac{1}{\sqrt{2}}|-1,0\rangle + \frac{1}{\sqrt{2}}|0,-1\rangle \ . \tag{6.10b}$$

The information about the state mixing will be important when analyzing which transitions are allowed and what are the transition probabilities when the magnetic field value is close to 1024 G.

6.2 Modeling ODMR signals in NV centers with HFS

Magnetic dipole transitions between the microwave (MW) field. The selection rules of these transitions are $\Delta m_S = \pm 1$ and $\Delta m_I = 0$ [73–75]. The MW transitions between levels $m_S = 0$ and $m_S = \pm 1$ can be described with raising and lowering operators:

$$\hat{S}_\pm = \hat{S}_x \pm i\hat{S}_y, \tag{6.11}$$

where S_X and S_Y are spin operators for the $S = 1$ state (5.7). However there are a total of nine wave functions: three electron spin states, each coupled to a nuclear spin of $I = 1$ from the ^{14}N nucleus. To construct the allowed transitions for this manifold, we must take an outer product with the three-dimensional identity matrix $\mathbb{1}(3)$ and fold in the 9×9 matrix of wave functions Ψ, whose columns are the ground-state eigenvectors $|\psi_i\rangle$ from (6.6)

$$\hat{S}'_\pm = \Psi^\dagger \left[\hat{S}_\pm \otimes \mathbb{1}(3)\right] \Psi \ . \tag{6.12}$$

Then the interaction term with the microwave field can be written as

$$\hat{H}^{(m)}_{INT} = \frac{\Omega_{MW}}{2}\left(\hat{S}'_+ + \hat{S}'_-\right) = \begin{pmatrix} \mu'_{00} & \mu'_{0-1} & \mu'_{01} \\ \mu'_{-10} & \mu'_{-1-1} & \mu'_{-11} \\ \mu'_{10} & \mu'_{1-1} & \mu'_{11} \end{pmatrix} \otimes \mathbb{1}(3) \ , \tag{6.13}$$

where Ω_{MW} is the Rabi frequency of the microwave radiation. The matrix elements μ'_{ij} are the terms proportional to magnetic-dipole transition matrix elements and describe the transition probabilities p'_{ij} between levels i and j:

$$p'_{ij} = |\mu'_{ij}|^2 \, . \tag{6.14}$$

While scanning the microwave frequency, the intensity of the microwave field is assumed to be constant. Furthermore, the microwave intensity is also assumed to be independent of the microwave field polarization, based on the specifics of the microwave antenna used in the experiment, described in Section 6.3. Therefore, as both calculated and experimental signals are normalized, the microwave field intensity is not a parameter in the calculations.

The rate of the transitions depends not only on the transition probabilities, but also on the population of the hyperfine substates. The nuclear-spin polarization of ^{14}N means that the hyperfine basis states are not populated equally. To account for nuclear-spin polarization we introduce a fitting parameter that corresponds to relative populations of the hyperfine basis states. The resonance transition rate t_{ij} can be expressed as a product of the transition probabilities p'_{ij} and the relative populations $N_i(m_I)$ of basis states m_I:

$$t_{ij} = p'_{ij} \cdot N_i(m_I) \tag{6.15}$$

The populations of hyperfine-basis states are normalized with the respect to $m_I = 1$, so that $N(+1) = 1$, which leaves two fitting parameters $0 \leq N(0), N(-1) \leq 1$ for nuclear spin polarization in the model.

The nuclear spin polarization then can be calculated as

$$P_{exp} = \frac{\sum_i m_I N_i(m_I)}{I \sum_i N_i(m_I)}, \tag{6.16}$$

where m_I is the nuclear spin projection of the basis states, and I is the nuclear spin. The summation is performed over all of the fitted resonances of the experimental ODMR.

The calculated transition frequencies and resonance transition rates were used to simulate the ODMR spectrum as a sum of Lorentzian curves for each hyperfine transition:

$$f(\omega) = \sum_{\substack{i,j \\ j>i}} \frac{t_{ij} \cdot \gamma^2}{(\omega - \omega_{ij})^2 + \gamma^2}, \tag{6.17}$$

where γ is the Lorentzian width, ω_{ij} is a transition frequency, and t_{ij} is a resonance transition rate.

The change of the transition rates due to level mixing is illustrated in Figure 6.2, where first row shows all of the possible transitions in the $|m_S = 0\rangle \longrightarrow |m_S = +1\rangle$ manifold, and the second row shows all of the transition in the $|m_S = 0\rangle \longrightarrow |m_S = -1\rangle$ manifold. At magnetic field values below and above the GSLAC, where the hyperfine levels are not mixed, there are three equally strong hyperfine transitions caused by the

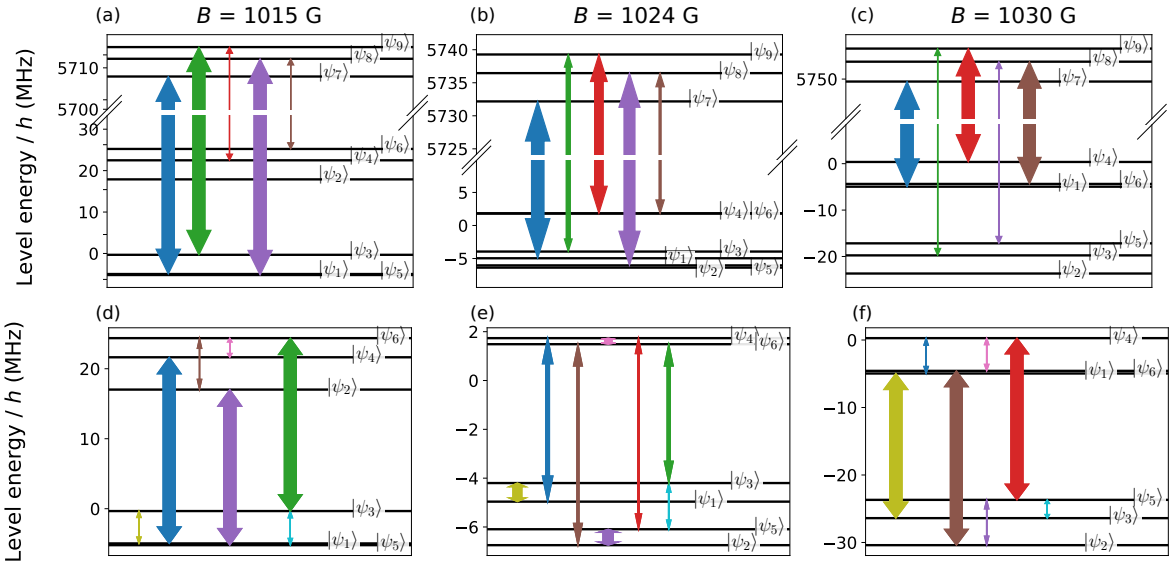

Figure 6.2: Hyperfine transitions of mixed states. The width of the arrows correspond to the transition probability. The states are labeled according to (6.6).

microwave field at frequencies corresponding to both, the $|m_S = 0\rangle \longrightarrow |m_S = +1\rangle$ (high frequency) and $|m_S = 0\rangle \longrightarrow |m_S = -1\rangle$ (low frequency) transitions. At the magnetic field value corresponding to the GSLAC, the hyperfine levels are mixed, and additional transitions appear. For the high frequency microwave regime, there is a total of five transitions (Figure 6.2b):

1. $|\psi_1\rangle \longrightarrow |\psi_7\rangle$ $(m_I = +1)$
2. $|\psi_3\rangle \longrightarrow |\psi_9\rangle$ $(m_I = 0)$
3. $|\psi_4\rangle \longrightarrow |\psi_9\rangle$ $(m_I = 0)$
4. $|\psi_5\rangle \longrightarrow |\psi_8\rangle$ $(m_I = -1)$
5. $|\psi_6\rangle \longrightarrow |\psi_8\rangle$ $(m_I = -1)$

The probabilities of these transitions depend on the strength of the magnetic field. At lower frequencies a total of eight transitions, the strength of which depends on the magnetic field, can be observed:

1. $|\psi_1\rangle \longrightarrow |\psi_4\rangle$ $(m_I = +1)$
2. $|\psi_1\rangle \longrightarrow |\psi_3\rangle$ $(m_I = +1)$
3. $|\psi_2\rangle \longrightarrow |\psi_5\rangle$ $(m_I = -1)$
4. $|\psi_2\rangle \longrightarrow |\psi_6\rangle$ $(m_I = -1)$
5. $|\psi_3\rangle \longrightarrow |\psi_5\rangle$ $(m_I = 0)$

6. $|\psi_3\rangle \longrightarrow |\psi_6\rangle$ $(m_I = 0)$

7. $|\psi_4\rangle \longrightarrow |\psi_5\rangle$ $(m_I = 0)$

8. $|\psi_4\rangle \longrightarrow |\psi_6\rangle$ $(m_I = 0)$

The difference between these cases is determined by the fact that in the first case, only one level of the transition is mixed by the magnetic field, but in the second case, the transition occurs between two levels that are both mixed by the magnetic field.

6.2.1 Modeled ODMR signal for $|m_S = 0\rangle \longrightarrow |m_S = +1\rangle$ transition manifold

The ODMR signals were modeled for different parameters: the transition width, the angle between the magnetic field and the NV center axis, and the nuclear-spin polarization. In this section we analyze the ODMR signals near the GSLAC for the microwave frequencies that correspond to the NV center ground-state $|m_S = 0\rangle \longrightarrow |m_S = +1\rangle$ transition manifold.

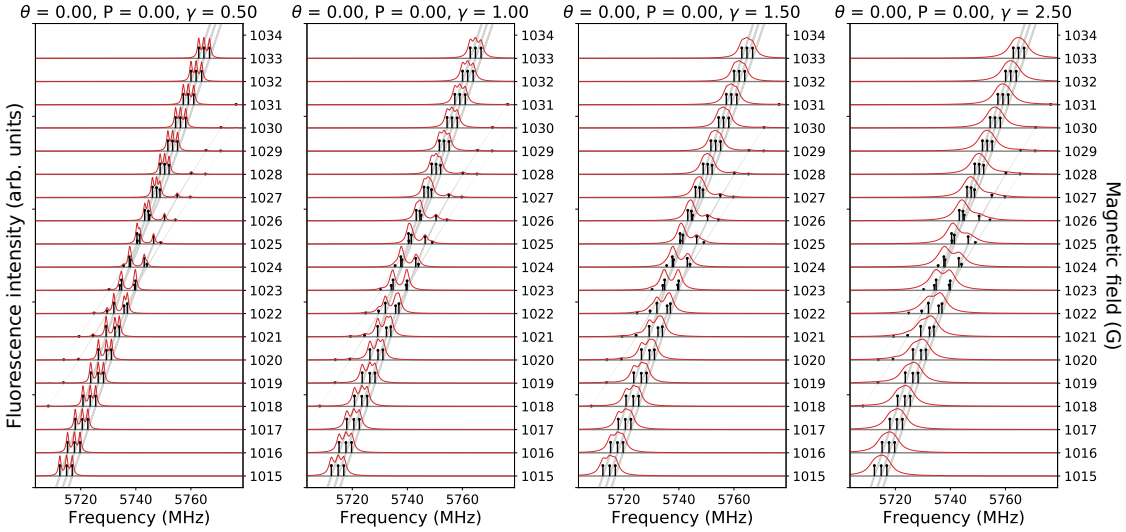

Figure 6.3: Modeled dependence of the shape of ODMR signals for the high-frequency region on the transition width. Left to right: $\gamma = 0.5$ MHz, $\gamma = 1.0$ MHz, $\gamma = 1.5$ MHz, $\gamma = 2.5$ MHz. The nuclear spin polarization is $P = 0\%$ and the angle between the NV center's axis and the magnetic-field direction is $\theta = 0°$.

Figure 6.3 shows the dependence of the shape of ODMR signals on the widths of the Lorentzians (left to right) for the $|m_S = 0\rangle \longrightarrow |m_S = +1\rangle$ transition manifold. The width of the signal corresponds to the excited-state coherence time T_2^*, which can be very different depending on the characteristics of the diamond. In this case it was assumed that there is no nuclear spin polarization $P = 0\%$ and the NV axis is parallel to the magnetic field ($\theta = 0°$).

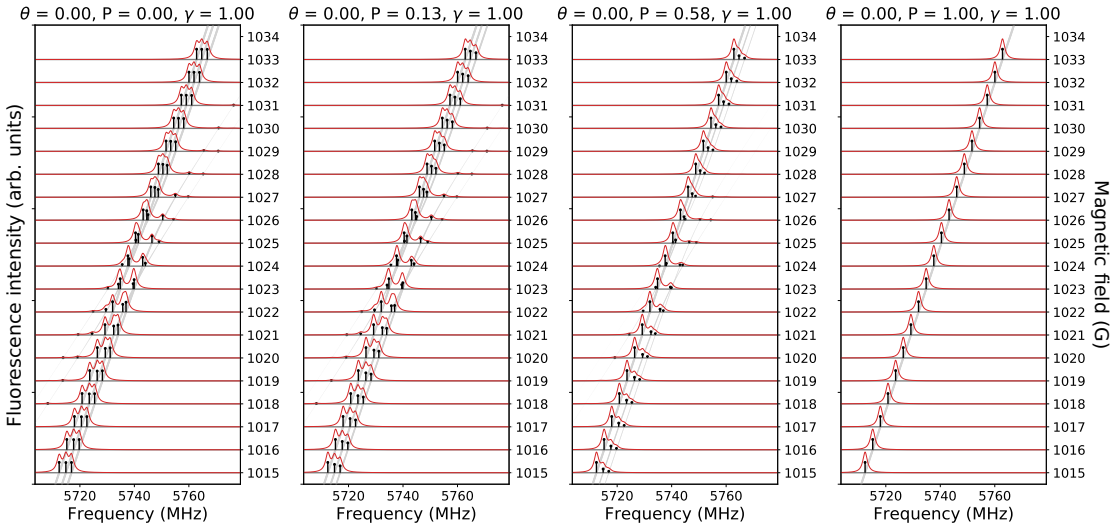

Figure 6.4: Dependence of the modeled ODMR signals for the high-frequency region dependence on the the nuclear-spin polarization. Left to right: $P = 0\%$, $P = 13\%$, $P = 58\%$, $P = 100\%$. The angle between the NV center's axis and the magnetic-field direction is $\theta = 0°$ and the profile width is $\gamma = 1.0$ MHz.

Another parameter that influences the shape of the ODMR signal is nuclear-spin polarization. Figure 6.4 shows theh dependence of the shape of ODMR signals on the nuclear-spin polarization. If the nuclear-spin polarization is at 100%, the level anticrossing is not observed. It was assumed that the NV axis is parallel to the magnetic field ($\theta = 0°$), and the width was chosen to be $\gamma = 1.0$ MHz.

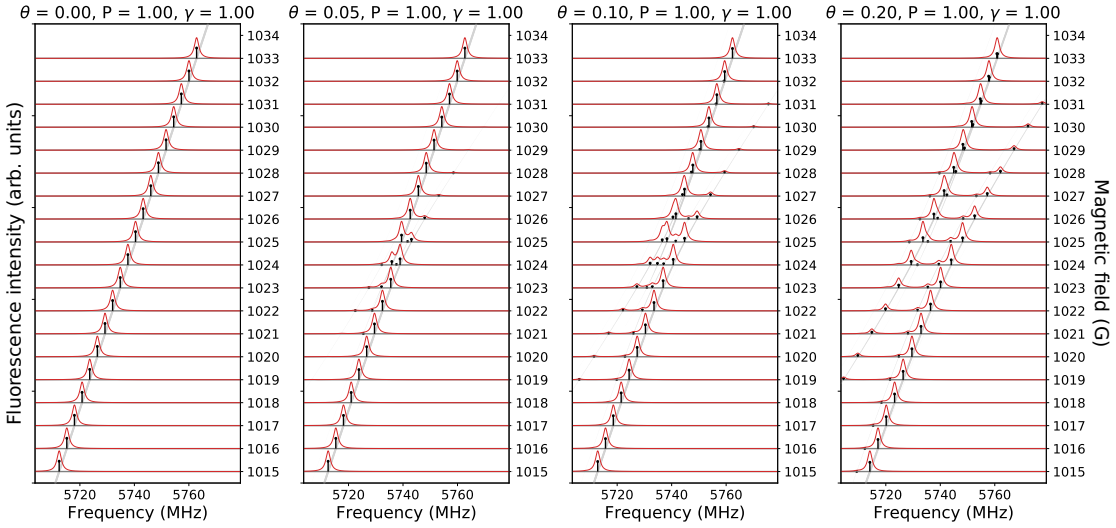

Figure 6.5: Dependence of the shape of modeled ODMR signals for the high-frequency region on the angle between the NV center's axis and the magnetic-field direction. The angle θ is in degrees of arc. Left to right: $\theta = 0.00°$, $\theta = 0.05°$, $\theta = 0.10°$, $\theta = 0.2°$. The nuclear-spin polarization is $P = 100\%$, and the profile width is $\gamma = 1.0$ MHz.

Figure 6.5 shows the dependence of the shape of ODMR signals on the angle θ between the magnetic-field direction and the NV center's principal axis (5.11). It can be seen that even a small magnetic-field angle can lead to a noticeable divergence of the ODMR signal near the GSLAC. This happens because the $|m_S = 0\rangle$ and $|m_S = -1\rangle$ states undergo extra mixing due to the transverse component of the magnetic field; thus, even more transitions can be observed. In this case it was assumed that the nuclear-spin polarization is $P = 100\%$ and the width was chosen to be $\gamma = 1.0$ MHz.

6.2.2 Modeled ODMR signal for the $|m_S = 0\rangle \longrightarrow |m_S = -1\rangle$ transition

When analyzing the modeled ODMR signals for a microwave-field range that corresponds to the ground-state $|m_S = 0\rangle \longrightarrow |m_S = -1\rangle$ transition manifold, it is evident that there are more transitions possible at the GSLAC than for high-frequency transitions. This is because the hyperfine levels of the two states between which the transitions are observed, $|m_S = 0\rangle$ and $|m_S = -1\rangle$, are involved in the anticrossing (Figure 6.2).

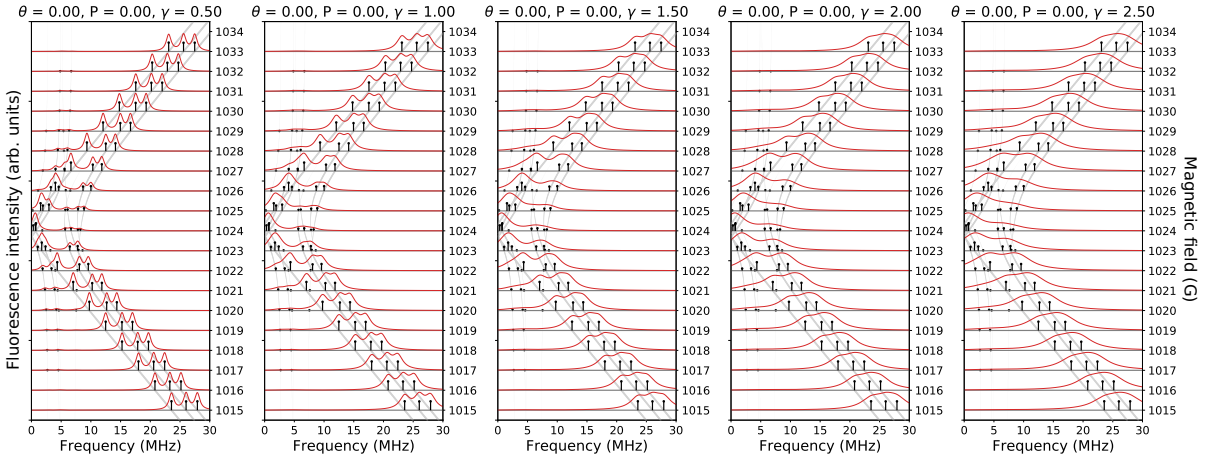

Figure 6.6: Dependence of the modeled ODMR signals for the low-frequency region on the transition width. Left to right: $\gamma = 0.5$ MHz, $\gamma = 1.0$ MHz, $\gamma = 1.5$ MHz, $\gamma = 2.0$ MHz, $\gamma = 2.5$ MHz. The nuclear-spin polarization is $P = 0\%$, and the angle between the NV center axis and magnetic field is $\theta = 0°$.

Figure 6.6 shows how the ODMR signal dependens on the width of the Lorentzian (left to right) for the $|m_S = 0\rangle \longrightarrow |m_S = -1\rangle$ transition manifold. If the width is increased, the hyperfine structure becomes unresolved.

Figure 6.7 shows the dependence of the ODMR signal on nuclear-spin polarization. The GSLAC can be still observed in the ODMR signals even for 100% nuclear-spin polarization, which is not the case for the the high-frequency region (Figure 6.4, where the anticrossing could not be observed when $P = 100\%$. The reason is that the population

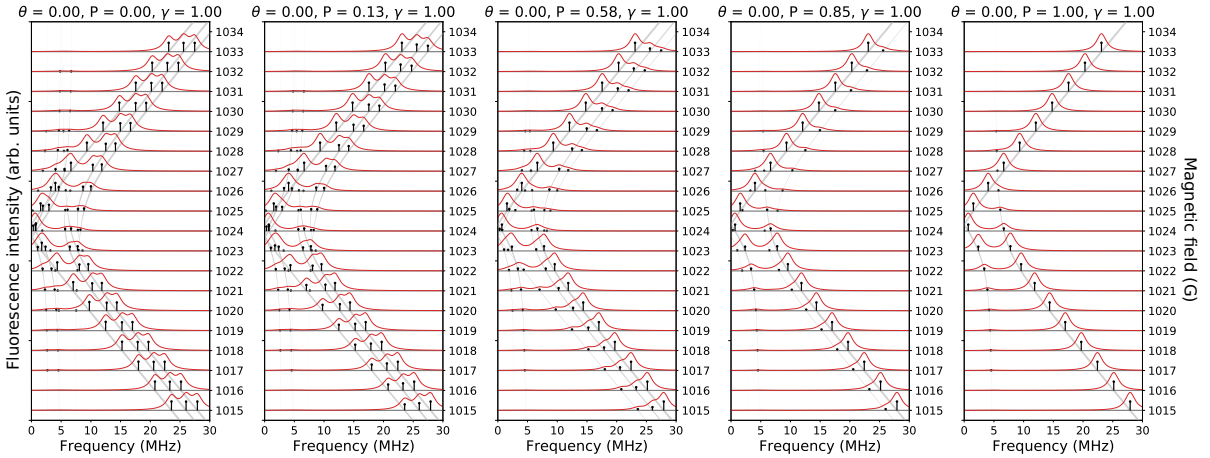

Figure 6.7: Dependence of the modeled ODMR signals for the low-frequency region on the nuclear spin polarization. Left to right: $P = 0\%$, $P = 13\%$, $P = 58\%$, $P = 85\%$ $P = 100\%$. The angle between the NV-center axis and the magnetic-field direction is $\theta = 0°$, and the profile width is $\gamma = 1.0$ MHz.

accumulates in the level $|\psi_1\rangle = |m_S = 0, m_I = +1\rangle$, and in the low-frequency region we can observe transitions from this level to both $|\psi_3\rangle$ and $|\psi_4\rangle$ with a transition strength depending on magnetic field intensity.

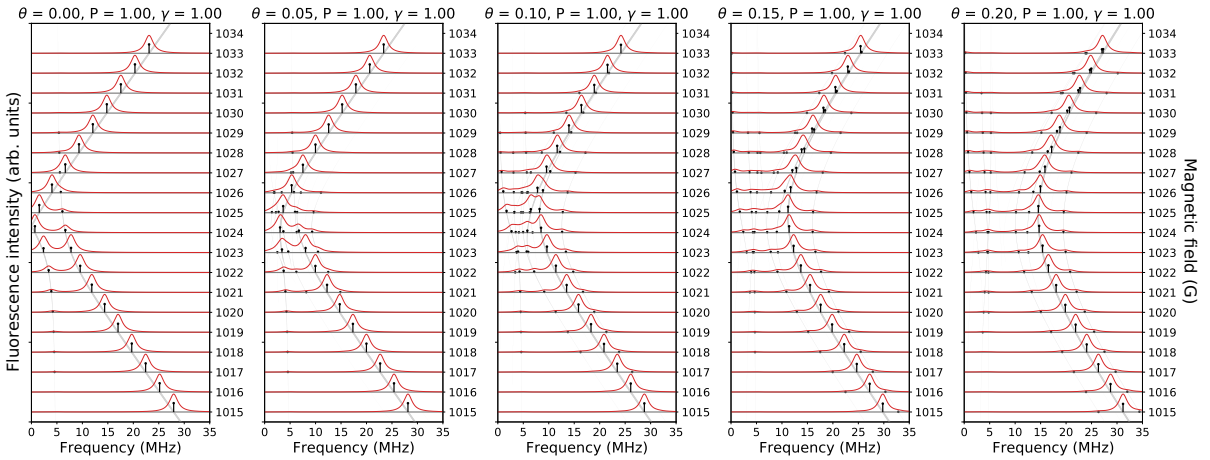

Figure 6.8: Dependence of the modeled ODMR signals for the low-frequency region on angle the between the NV-center axis and the magnetic-field direction. The angle θ is in arc degrees. Left to right: $\theta = 0.00°$, $\theta = 0.05°$, $\theta = 0.10°$, $\theta = 0.15°$, $\theta = 0.2°$. The nuclear-spin polarization is $P = 100\%$, and the profile width is $\gamma = 1.0$ MHz.

Figure 6.8 shows the dependence of ODMR signals on the angle θ between the magnetic-field direction and the NV center's principal axis. Even a small magnetic-field angle influences the ODMR signals at the GSLAC. When the angle between the magnetic field and NV center's principal axis is increased, the minimal transition frequency increases, meaning that the interaction of the transverse magnetic field also causes the

mixing of levels that were not previously involved into the anticrossings. All of the levels are mixed at this point, and there are no real crossings, so the transition frequencies cannot approach 0 MHz. As the transverse magnetic field is increased, the interaction between the levels increases and the transition frequencies move away from the zero frequency.

6.2.3 Modeling ODMR signals with proximal C13 nuclear spins

Diamond crystals consist mostly of the ^{12}C carbon isotope. As the nucleus of ^{12}C has spin $I = 0$, ^{12}C nuclei from the crystal lattice do not interact with NV centers. However, 1.1% of carbon atoms in the diamond lattice are belong to the ^{13}C isotope. The nuclear spin of ^{13}C is $I = \frac{1}{2}$. To analyze the influence of ^{13}C atoms on nuclear-spin polarization, the interaction between NV centers and ^{13}C nuclei must be considered [67] in addition to the regular NV-center Hamiltonian (5.5):

$$H_{\mathrm{NV+13C}} = \Sigma_j \left(\hat{\mathbf{S}} \cdot \hat{A}'_{\mathrm{13C},j} \cdot \hat{\mathbf{I}}_{\mathrm{13C},j} + \hat{H}_{\mathrm{13C},j} \right) , \tag{6.18}$$

where $\hat{\mathbf{I}}_{\mathrm{13C},j}$ labels the nuclear spin of the j-th ^{13}C nucleus and $\hat{H}_{\mathrm{13C},j} = \gamma_{\mathrm{13C}} \mathbf{B} \cdot \hat{\mathbf{I}}_{\mathrm{13C},j}$ is the Hamiltonian that corresponds to the j-th ^{13}C nucleus. Ignoring the strain interaction, the total Hamiltonian of the NV center (5.5) and the ^{13}C nuclear spin (6.18) is:

$$\hat{H}_g = \hat{H}_S + \hat{H}_{\mathrm{N}} + \hat{H}_B + H_{\mathrm{NV+13C}}. \tag{6.19}$$

The hyperfine-interaction tensor $\hat{A}_{\mathrm{13C},j}$ in the basis of the principal axes has the same form as the ^{14}N hyperfine-interaction tensor (5.8). For the nearest ^{13}C nucleus to the vacancy (three equivalent positions), the values of $\hat{A}_{\mathrm{13C},j=1}$ are $A_\perp = A_{xx} = A_{yy} =$ 121.1 MHz and $A_\parallel = A_{zz} = 199.21$ MHz [76]. As the tensor is given in the basis of the principal axes of the carbon nucleus, it has to be rotated to the coordinate system of the NV center with the Z-axis parallel to the [111] crystal direction. The rotated tensor is

$$\hat{A}' = \hat{U} \hat{A} \hat{U}^T, \tag{6.20}$$

where $\hat{U}$ is the rotation matrix about x-axis that rotates the z-axis in the frame of the carbon nucleus by an angle α_{zZ} into the frame of the [111] crystal direction [67]:

$$\hat{U} = \begin{pmatrix} 1 & 0 & 0 \\ 0 & \cos\alpha_{zZ} & -\sin\alpha_{zZ} \\ 0 & \sin\alpha_{zZ} & \cos\alpha_{zZ} \end{pmatrix} . \tag{6.21}$$

To describe the ^{13}C nuclear-spin interaction one needs to take into account the influence of the ^{13}C atoms in other lattice positions as well. The lattice positions can be classified into families that have the same tensor values [77]. The tensor values and the value of the angle between the vector pointing from the NV center to the ^{13}C atom and

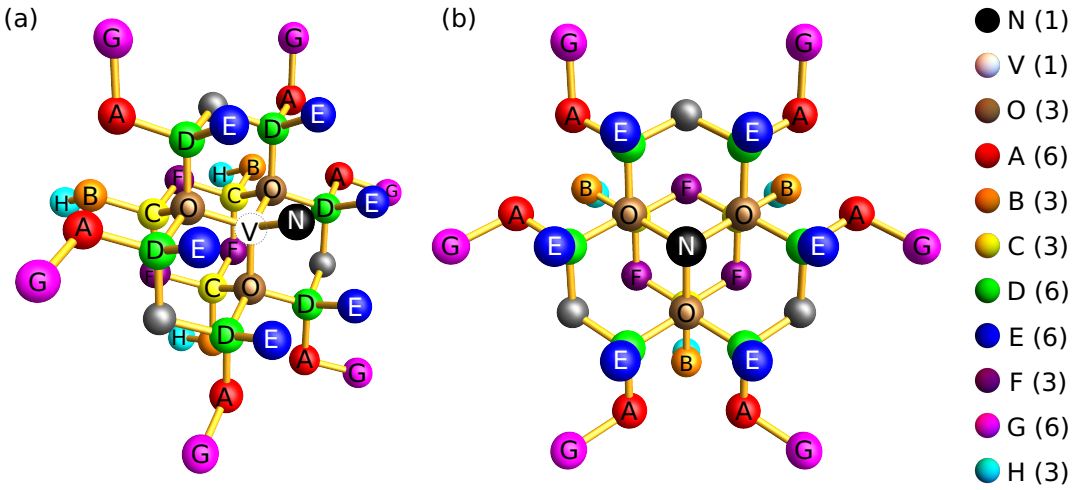

Figure 6.9: Lattice with C13 sites. (a) Side view. (b) Top view of the [111] direction.

the NV center's principal axis α_{zZ} were taken from the results of density functional theory (DFT) calculations [2, 3]. In the simulation of the ODMR signal, we used the nearest neighbor (O) as well as families from A through H (Table 6.1), which correspond to 39 lattice sites. Other lattice sites provide an insignificant contribution.

Family	N_{C}	A_{xx}	A_{yy}	A_{zz}	$\lvert\cos(\alpha_{zZ})\rvert$
O	3	121.1	121.1	199.21	0.274
A	6	13.5	14.2	19.4	0.288
B	3	12.8	12.8	18	0.412
C	3	-7.4	-7.3	-5.8	0.907
D	6	-4.8	-3.7	-1.5	0.296
E	6	2.8	3.3	4.6	0.848
F	3	3.4	4.7	4.9	0.829
G	6	2.6	2.7	3.8	0.247
H	3	1.5	1.5	2.2	0.956

Table 6.1: Principal values of the hyperfine tensor [2] and the rotation angle [3] used in the simulation of the ODMR signal. The positions of the ^{13}C families are shown in Figure 6.9.

Next, the Monte Carlo method was used to average over the different lattice sites where ^{13}C atoms could be located. The program iterated through the 39 lattice sites, each of which had a 1.1% probability of hosting a ^{13}C atom. The lattice sites that contained a ^{13}C atom were added to the Hamiltonian in (6.18) with the hyperfine tensor values based on the lattice site (Table 6.1). With each ^{13}C added to the equation, the number of energy levels of the system triples as $N_{levels} = 3 \times 3 \times 2^{N_{\mathrm{C13}}}$. Using the eigenvalues and eigenvectors of the total system Hamiltonian (6.19), the ODMR spectra were simulated

as described in Section 6.2. The spectrum depends on the locations of the ^{13}C atoms as well as the number of ^{13}C atoms in the lattice, resulting in a different spectrum for each iteration. Taking into account all statistically relevant configurations of ^{13}C nuclei in the vicinity of the NV center required averaging over several hundreds of iterations.

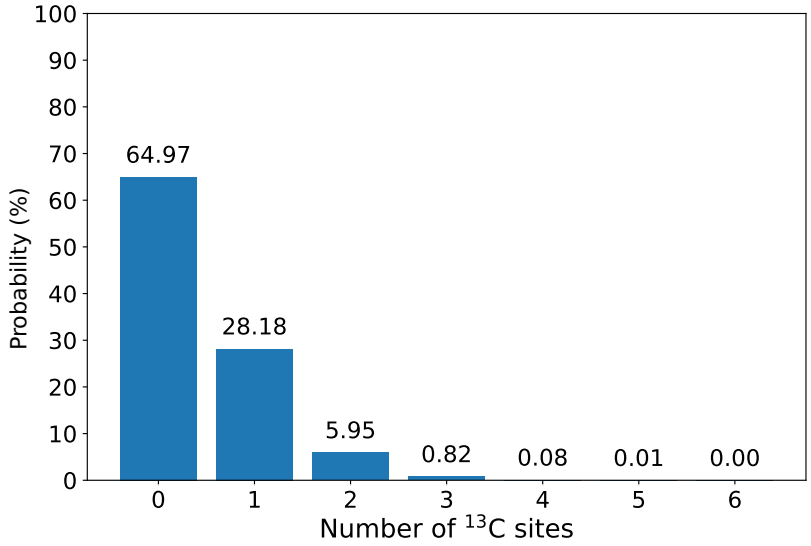

Figure 6.10: Probability distribution of the number of lattice sites with a ^{13}C atom.

Figure 6.10 shows the calculated probability of the number of ^{13}C sites in the volume of the lattice considered by the simulation (Fig. 6.9). Most of the time ($\sim$65 %) these lattice sites do not contain any ^{13}C atom. Around 28 % of the time there is one ^{13}C in the lattice and 6 % of the time, there are two ^{13}C. Only occasionally three or more ^{13}C are found in the lattice at the same time (less than 1 %).

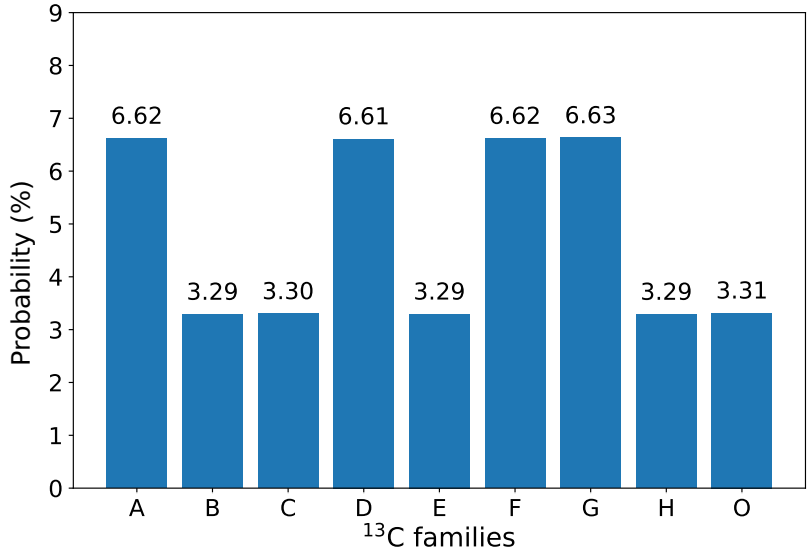

Figure 6.11: Probability of ^{13}C by lattice site families.

To analyze the structure of the signal, we calculate the impact of each of the ^{13}C families, simplifying the system by limiting the number of ^{13}C atoms to one ^{13}C atom in the lattice. Figure 6.11 shows the probability of finding the ^{13}C atoms in the lattice site of each family. The distribution among the lattice sites of ^{13}C families can be described by $P(^{13}\text{C family}) = 1 - (1 - 0.011)^{N_C}$, where N_C is the number of equivalent ^{13}C lattice sites and 0.011 is the probability of the atom in the lattice site being ^{13}C.

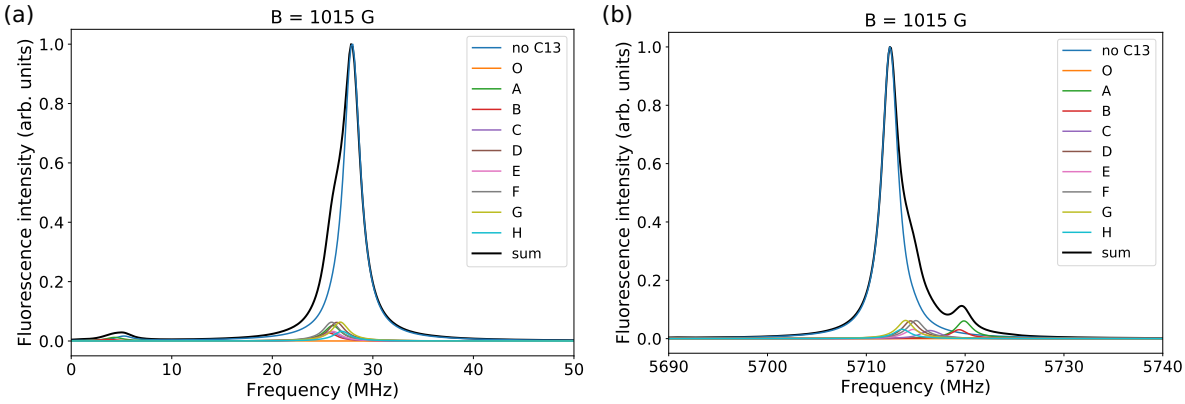

Figure 6.12: ODMR with C13 interaction for transitions in the (a) $|m_s = 0\rangle \longrightarrow |m_s = -1\rangle$ manifold, (b) $|m_s = 0\rangle \longrightarrow |m_s = +1\rangle$ manifold. The nuclear spins of both ^{14}N and ^{13}C are fully polarized in the calculation.

Figure 6.12 shows calculated ODMR signals for the $|m_s = 0\rangle \longrightarrow |m_s = -1\rangle$ (Figure 6.12a) and $|m_s = 0\rangle \longrightarrow |m_s = +1\rangle$ (Figure 6.12b) transition manifolds, taking into account the interaction with ^{13}C nuclear spins. Each curve in Figure 6.12 was calculated using the hyperfine tensor of each ^{13}C family by the method described in Section 6.2. The height of each curve was divided by $P(^{13}\text{C family})$ to account for the probability of finding a ^{13}C in a particular lattice site. To have a better distinction between the curves of different lattice-site families, the nuclear spin polarization of both ^{14}N and ^{13}C was set to be 100% in the calculations. The influence of ^{13}C nuclear spin interaction can be seen clearly for the $|m_s = 0\rangle \longrightarrow |m_s = +1\rangle$ transition manifold as a feature to the right of the main peak. This feature corresponds to the nuclear spins of ^{13}C that occupy lattice site families "A" and "B" (see Figure 6.9 and Table 6.1). The hyperfine-interaction strength of these ^{13}C nuclear spins are 13.5 MHz and 12.8 MHz, respectively. The ^{13}C nuclear spins with hyperfine interaction less than 10 MHz are unresolved in the calculated signals. Although the nuclear spin at the nearest site "O" is resolved, the feature is too small to be visible in the signal.

6.3 Comparison of the modeled signals with experimentally measured signals

The results of the following section have been published in [71] and [72]. The experimental measurements were mostly done by Reinis Lazda, Andris Berzins and Huijie Zheng. The experimental setup is described in the appendix and is not part of the dissertation (see A.2). At the same time the analysis of the experimental data was crucial to developing a model that could be used for fitting the experimental signals. Therefore, a description of the data analysis and fitting procedures is included as a part of the dissertation.

The majority of the experimental data analyzed in this section were obtained by measuring the ODMR signals from ensembles of NV centers in two samples with different nitrogen concentrations. Thus, it was possible to apply the model calculation using different parameters, such as the width of the signal, which characterizes the coherence relaxation time T_2^*, the nuclear spin polarization and the angle between the magnetic field and the NV center's axis. One sample was produced by chemical vapor deposition (CVD) with a nitrogen concentration of around 1 ppm (low-density sample). The other sample was a dense, high-pressure, high-temperature (HPHT) crystal with a relatively high concentration of nitrogen of around 200 ppm (high-density sample). The measurements with the low-density sample were performed at the Johannes Gutenberg-University in Mainz, whereas the measurements with the high-density sample were performed at the Laser Centre of the University of Latvia in Riga. The NV centers were irradiated with green 532 nm light and optically polarized to the $m_S = 0$ state while the red fluorescence from the ^3E state was monitored (see the transition diagram in Figure 5.4). Following the ODMR method (Section 5.3), a microwave field was applied to induce transitions between the ground-state sublevels. The NV centers' electrons were continuously pumped to the $m_S = 0$ state. When a MW field is on resonance with a transition from an $m_S = 0$ hyperfine component to an $m_S = \pm 1$ hyperfine component, the fluorescence intensity decreases.

Another set of measurements, analyzed in this section, was performed using a diamond crystal obtained through CVD with a nitrogen ^{14}N concentration of about 5–20 ppm. The experimental results shown in Figure 6.19 describe the ODMR signal dependence on the angle between the magnetic-field direction and the NV center's axis. The setup for this experiment is described in A.3.

6.3.1 Data analysis and fitting procedure

Before applying the theoretical model to the experimental results, the raw data had to be processed. The magnetic field in the experiment was applied using an electromagnet whose magnetic field was proportional to the applied electric current. To ensure the

precision of the applied magnetic field, the magnetic field had to be calibrated first. The initial calibration of the electromagnet with a Hall probe did not provide the required precision, so we used the peak positions of the measured ODMR signals.

The precise value of the magnetic field for calibration was determined from the peak position of the ODMR signal for the $|m_S = 0\rangle \longrightarrow |m_S = +1\rangle$ transition manifold as $B = \frac{\omega_{peak} - D - A_\parallel}{\gamma_e}$ and for the $|m_S = 0\rangle \longrightarrow |m_S = -1\rangle$ transitions as $B = \frac{D - A_\parallel - \omega_{peak}}{\gamma_e}$ at magnetic fields values below the level-anticrossing point and $B = \frac{D - A_\parallel + \omega_{peak}}{\gamma_e}$ at magnetic field values above the anticrossing point.

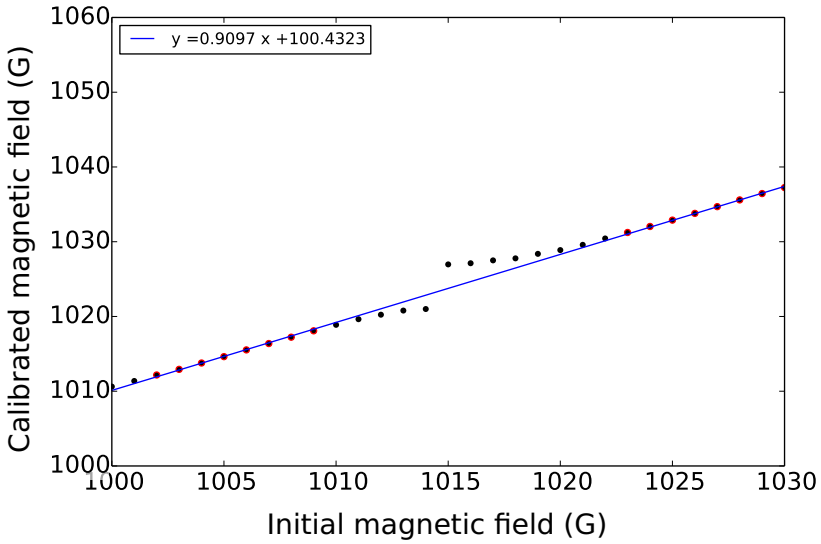

Figure 6.13: Magnetic-field calibration for the $|m_S = 0\rangle \longrightarrow |m_S = +1\rangle$ transition manifold. The black dots are the magnetic field values determined from the experimental peak positions (vertical axis) with regard to the initial calibration of the electromagnet (horizontal axis). The blue line is the linear approximation of the calibrated magnetic field values that does not deviate from the line (red dots).

At the GSLAC the magnetic field cannot be determined by these equation due to the level mixing, so it is important to take into account the linear relation between calibrated and initial magnetic field (Figure 6.13). The black dots are the calculated magnetic field values as described above. It can be seen that close to the GSLAC, these values deviate from the straight line. The x-axis is the initial assessment of magnetic field, which is proportional to the current set to the electromagnet. To determine the linear connection between the initial assessment of magnetic field and calibrated magnetic field, we only used the points that lie on the straight line (red dots in Figure 6.13) for linear approximation. The calibrated magnetic field values at the GSLAC were then calculated using this linear function.

Experimental data were fitted using the model described in Section 6.2 using the method `Model` of the `python` library `lmfit` [78]. While fitting an experimental ODMR

signal, the magnetic field value is allowed to vary a little bit, because nuclear spin polarization can shift the peak position for signals with only partially resolved and unresolved hyperfine structure. The fitting parameters are Lorentzian width (6.17), nuclear spin polarization (6.16), magnetic field value and magnetic field angle (5.10). To determine all of these parameters from the data, the fitting was done iteratively using a parameter optimization procedure based on the χ^2 test. The χ^2 is defined as

$$\chi^2 = \frac{1}{N} \sum_i \left(\frac{f_i - d_i}{\sigma_i} \right)^2 , \tag{6.22}$$

where N is the degree of freedom, the d_i are the measured data points, the f_i are the results of the model, and the σ_i are the mean square errors on the data points, which were set to unity here.

6.3.2 ODMR signals for the $|m_S = 0\rangle \longrightarrow |m_S = +1\rangle$ transition

Figure 6.14 shows ODMR signals in the frequency range 5.6−5.9 GHz, in which transitions occur between a hyperfine-level manifold of mixed $m_S = 0$ and $m_S = -1$ levels and the hyperfine-level manifold of $m_S = +1$.

Figures 6.14a–6.14c depict magnetic sublevels at a given magnetic field. The arrows indicate the allowed microwave transitions, based on the selection rules and mixed wave functions (6.6). The width of each arrow indicates the transition strength.

In the rest of the figures experimental signals are depicted together with the fitted curves that have been obtained from the fitting procedure as explained above. The middle row (Figures 6.14d–6.14f) shows signals for the low-density sample (1 ppm), and the bottom row (Figures 6.14g–6.14i) shows signals for high-density sample (200 ppm).

In Figures 6.14d and 6.14g signals were recorded at a magnetic field value that is below the GSLAC. In this case the mixing of levels is small, and only three transitions contribute to the signal: $|0,1\rangle \longrightarrow |1,1\rangle$ (blue), $|0,-1\rangle \longrightarrow |1,-1\rangle$ (purple), and $|0,0\rangle \longrightarrow |1,0\rangle$ (green). The transition strengths for there transitions were equal, which is shown in 6.14a. Nevertheless, the relative transition rates of each transition may differ due to differences in the populations of the three ground states involved, $|0,+1\rangle$, $|0,0\rangle$, and $|0,-1\rangle$, which correspond to the nuclear-spin polarization of ^{14}N. The color bars in 6.14d and 6.14g are transition rates obtained from model fitting. The color of each bar corresponds to the color of the arrow that represents the corresponding transition in Fig. 6.14a. Near the GSLAC (Figures 6.14e and 6.14h) there are more transitions that need to be considered due to level mixing (6.6). The possible transition are show in (Figure 6.14b). At magnetic field values above the GSLAC position, mixing of states decreases again, which can be seen in Figures 6.14f and 6.14i where three transitions contribute to the overall signal.

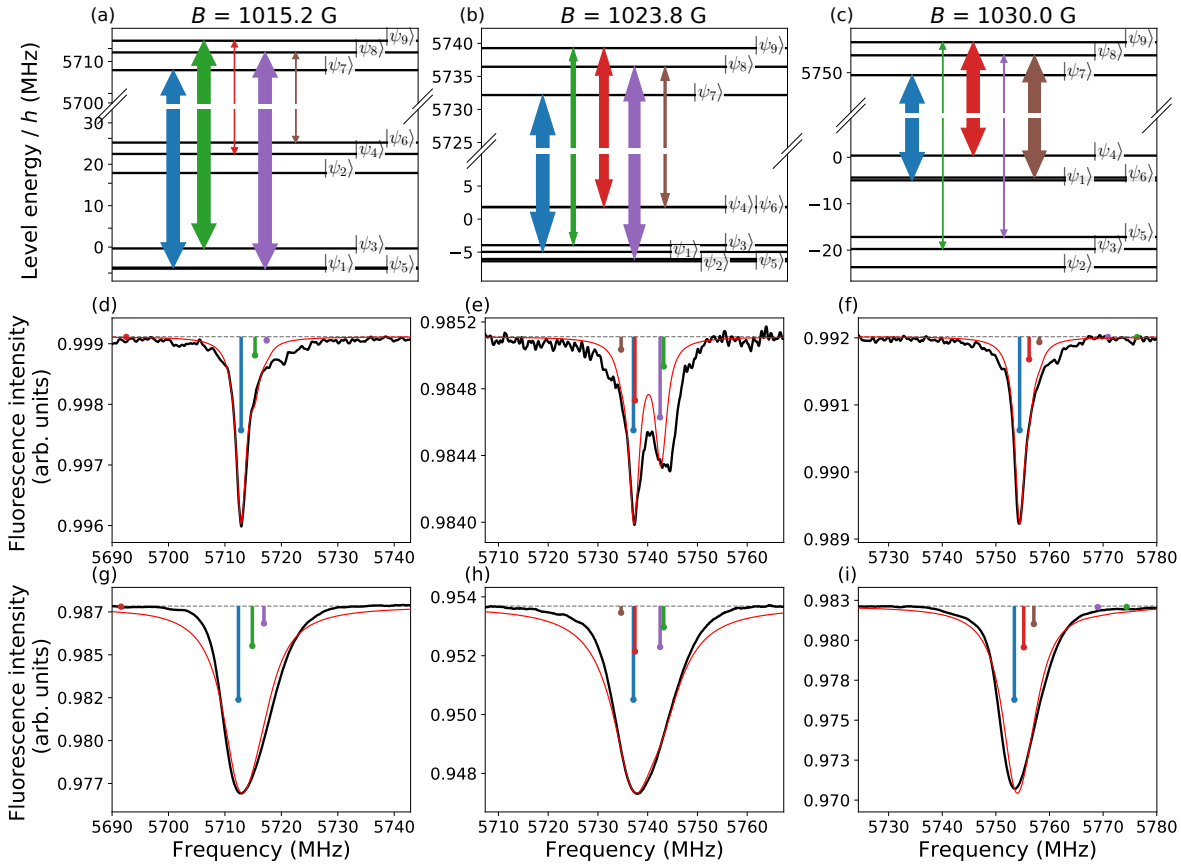

Figure 6.14: ODMR signals at high microwave field frequencies. The top row (a)–(c) shows transitions between the levels (6.6). The arrow width corresponds to the transition probability. The middle row (d)–(f) shows signals for the low-density sample, and the bottom row shows signals for the high-density sample. The black curves are experimental data; the red curves show the results of the theoretical calculations with the parameters from the fitting procedure. The vertical bars in (d)–(i) correspond to the transitions depicted by the arrows in (a)–(c) of the same color, and their length determines the contribution to the overall lineshape of that transition, which is proportional to the product of the level population and the transition strength.

6.3.3 ODMR signals for the $|m_S = 0\rangle \longrightarrow |m_S = -1\rangle$ transition

The same analysis can be carried out for the $|m_S = 0\rangle \longrightarrow |m_S = -1\rangle$ transition, which corresponds to microwave frequencies below 40 MHz. The results of measured and calculated ODMR signals are plotted in Figure 6.15. The top row (Figures 6.15a–6.15c) shows the magnetic sublevel structure for a particular magnetic field. The arrows indicate the allowed transitions, and the arrow widths indicate the relative transition strengths.

The middle row (Figures 6.15d–6.15f) shows signals for the low-density sample, and the bottom row (Figures 6.15g–6.15i) shows signals for high-density sample.

Similar to the high-frequency signals (Figure 6.14), for magnetic-field values ~ 10 G

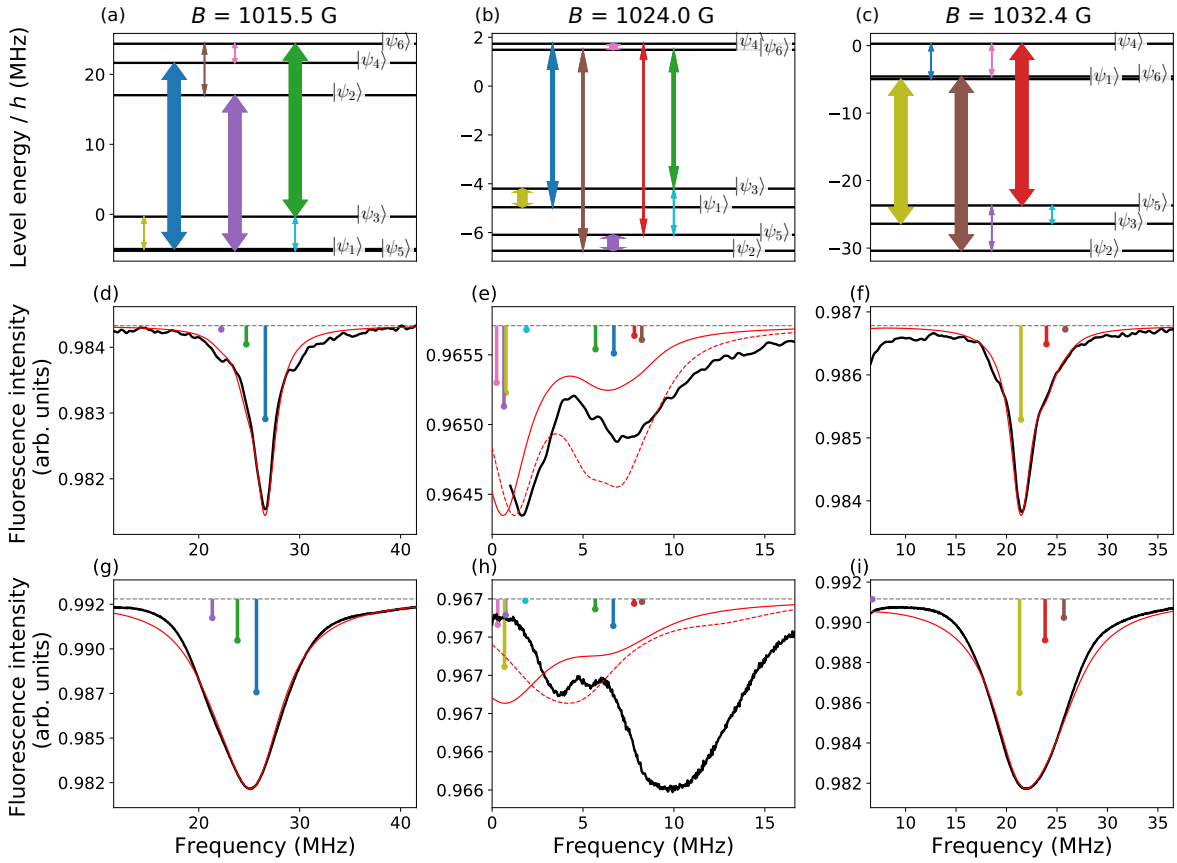

Figure 6.15: ODMR signals at low microwave-field frequencies. The top row (a)–(c) shows transitions between the different levels (6.6). The width of the arrows corresponds to the relative transition probabilities. The middle row (d)–(f) shows signals for the low-density sample, and the bottom row shows signals for the high-density sample. The black curves are experimental data, the red curves show the results of the theoretical calculations with the parameters from the fitting procedure. The vertical bars correspond to the transitions depicted by the arrows in (a)–(c) of the same color, and their length determines the contribution to the overall lineshape of that transition, which is proportional to the product of the level population and the transition strength. The dashed red lines in (e) and (h) show the calculated signal for an angle between the NV axis and the magnetic-field **B** direction of $\theta = 0.015°$. The vertical bars in (d)–(i) correspond to the transitions depicted by the arrows in (a)–(c) of the same color for $\theta = 0°$.

away from the GSLAC position, the signals consist of three components (Figures 6.15d and 6.15g for magnetic-field values less than the GSLAC position, and Figures 6.15e and 6.15h for magnetic-field values larger than the GSLAC position).

As can be seen in Figure 6.15b, there are more allowed transitions than in the case of high-frequency transitions. This happens because the initial and final levels connected by microwave transitions are from the same mixed-level manifold ($m_S = 0$ and $m_S = -1$). As a result, the ODMR signal is more complicated. For the low-density sample, the

model qualitatively describes the experimental ODMR signal (Fig. 6.15e). The solid red line is the modeled signal for the ideal case when the magnetic field is parallel to the NV axis ($\theta = 0°$). The red dashed line is modeled assuming a small deviation between the magnetic-field direction and the NV center's axis ($\theta = 0.015°$). Introduction of a small angle shifts the peak away from zero frequency, bringing it closer to experimental peak. The same was done for the high-density sample (Figure 6.15h). The solid red line in this case does not describe the experimental signal at all. Introducing an angle between magnetic field direction and NV axis ($\theta = 0.1°$) only partially improves the agreement. There is a larger peak at $\sim$ 10 MHz that cannot be explained by the model. Possible reasons for the discrepancies might be interaction with other nearby spins in the crystal, such as substitutional nitrogen (P1) centers or ^{13}C nuclei. There might also be some inhomogeneities in microwave power or in the diamond crystal lattice, or in the magnetic field.

6.3.4 Influence of the angle between the magnetic-field direction and the principal axis of the NV center

We observed that even small misalignment of the magnetic-field direction and the NV center's axis can noticeably influence signals near the GSLAC. Figure 6.16 shows the transition frequencies for the $|m_S = 0\rangle \longrightarrow |m_S = -1\rangle$ transition for magnetic-field angle $\theta = 0°$ (Fig. 6.16a) and $\theta = 0.1°$ (Fig. 6.16b), as well as transition frequencies for the $|m_S = 0\rangle \longrightarrow |m_S = +1\rangle$ transitions. The black dots and red squares correspond to experimental ODMR peak frequencies of the high-density and low-density samples, respectively. The gray lines correspond to theoretically calculated transition frequencies for all hyperfine levels. The widths of the gray lines show the transition strengths based on level mixing (6.14).

Figures 6.17 (low NV-density sample) and 6.18 (high NV-density sample) show experimentally measured and modeled ODMR signals near the GSLAC in more detail. For better readability, signals are arranged in order of descending magnetic field, and each curve is normalized separately with its relative intensity depicted at the right side of the graph. The gray lines show how the energy and the intensity of the transitions change in the magnetic field. Comparing Figures 6.17a, where $\theta = 0°$, and 6.17b with $\theta = 0.015°$, one sees that agreement between the model and the experiment improves noticeably when a small angle is introduced into the model. The improvement is even more evident in Figures 6.18a and 6.18b for the high-density sample. From these signals, we have estimated that the angle between the magnetic-field direction and the NV axis for this sample was around $\theta = 0.1°$, which corresponds to a transverse magnetic field at the GSLAC of $B_x = 1.85$ G, which on the order of of magnitude of the Earth's magnetic field, which was not compensated in the experiment. Low-frequency transitions

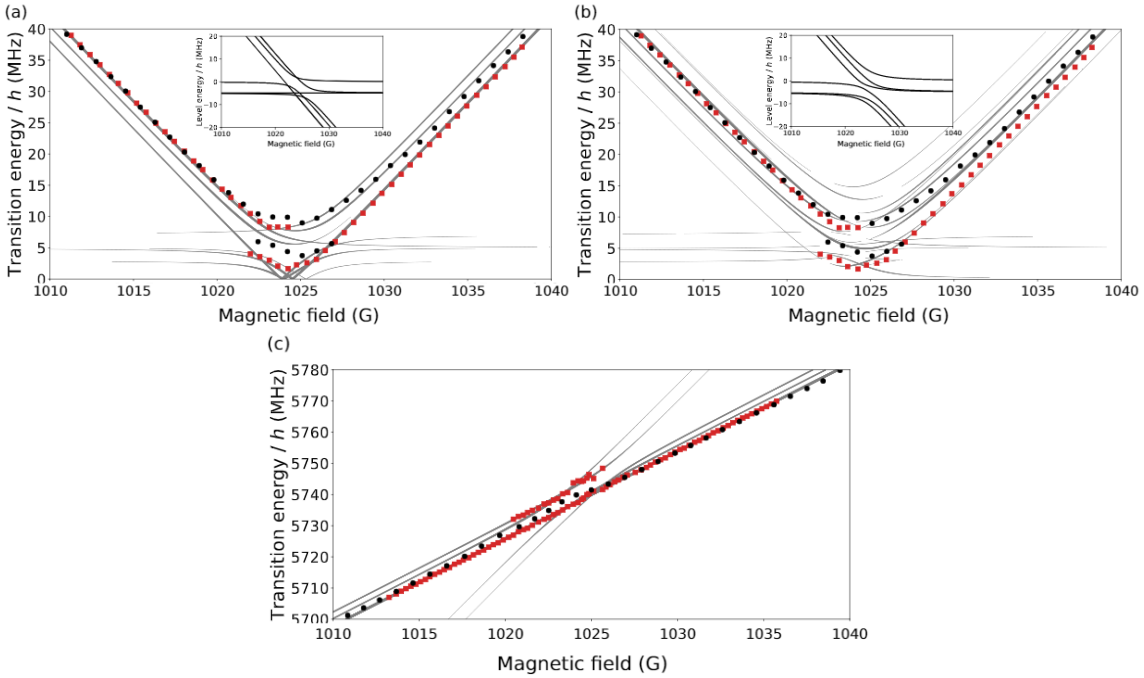

Figure 6.16: Transition frequencies for the $|m_S = 0\rangle \longrightarrow |m_S = -1\rangle$ transition manifold for magnetic-field angle (a) $\theta = 0°$ and (b) $\theta = 0.1°$. (c) Transition frequencies for the $|m_S = 0\rangle \longrightarrow |m_S = +1\rangle$ transition manifold for magnetic-field angle $\theta = 0°$. The black dots and red squares correspond to the experimental ODMR peak frequencies of the high-density and low-density samples, respectively. The gray lines correspond to theoretically calculated transition frequencies for all of the hyperfine levels. The width of gray lines show the transition strengths based on level mixing.

between $|m_S = 0\rangle$ and $|m_S = -1\rangle$ are more sensitive to level mixing and magnetic-field angle because both of the levels that are involved in the transitions are mixed states. For high-frequency transitions (Figures 6.17c and 6.18c), the calculated signals with or without transverse magnetic field did not show a noticeable difference.

Another set of measurements were made to evaluate how the shape of an ODMR signal changes with respect to the angle between the magnetic-field vector and the principal axis of the NV center. For this experiment a sample with a nitrogen concentration of 5–20 ppm was used. In the experiments the angle between the magnetic field and the crystal was changed by adjusting the orientation of the sample holder with respect to magnetic field. The angle between the magnetic-field vector and the NV axis was determined by fitting the ODMR signal as described in Section 6.3.1. Figure 6.19 shows the dependence of the ODMR signal on the experimentally measured magnetic-field angle at the GSLAC in the ground-state $m_S = 0$ and $m_S = -1$ microwave transition manifold. Our fitting procedure allowed us to determine the angle of the magnetic field with a precision of 0.02°. Figure 6.19a shows the ODMR signal for the best experimentally achieved alignment with respect to the external magnetic field direction, which was deter-

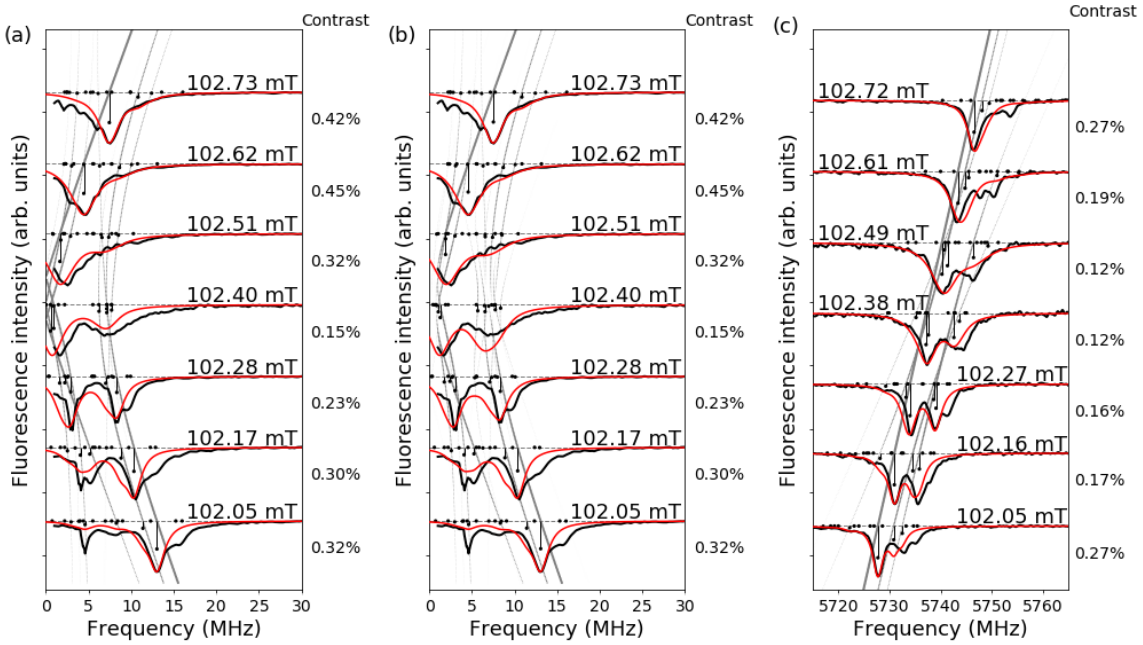

Figure 6.17: Experimental signals (black) obtained from the low-density sample with theoretical calculations (red) in the ground-state $m_S = 0 \longrightarrow m_S = -1$ microwave transition manifold for different magnetic-field values and for an angle between the NV axis and the magnetic-field **B** direction of (a) $\theta = 0°$ and (b) $\theta = 0.015°$ (transverse magnetic field 0.25 G). (c) Experimental signal with the calculated signal at $\theta = 0°$ in the ground-state $m_S = 0 \longrightarrow m_S = +1$ microwave-transition manifold for different magnetic-field values.

mined by the fitting procedure to be 0.11°. Increasing the angle between the NV axis and the external magnetic-field direction causes the ODMR structure to transform into two groups of peaks. This structure is explained by the mixing of the $|m_S = 0\rangle$ and $|m_S = -1\rangle$ hyperfine levels (Figure 6.1b), which are energetically close at the GSLAC point. At angles from 0.21° to 0.46° two distinct groups of peaks can be seen in the ODMR signals (Figure 6.19b–d).

6.3.5 ODMR signals with C13 interaction

The calculated ODMR signals obtained from the model with ^{13}C are shown in Fig. 6.20a for the $m_S = 0 \longrightarrow m_S = -1$ transition and in Fig. 6.20b for the $m_S = 0 \longrightarrow m_S = +1$ transition. The blue curves show the calculation without the ^{13}C interaction, and the red curves show the calculation taking into account interaction with the spins of nearby ^{13}C nuclei. The black line shows the experimental measurements [71]. Inclusion of the ^{13}C interaction improves the agreement with the calculations, but some discrepancies for magnetic-field values close to the GSLAC still remain. Including the ^{13}C hyperfine interaction (6.19) allows some new transitions to appear in the simulated signals. The new transitions are most apparent in Figure 6.20b to the right of the main peak for magnetic field values that range from 1017.4 G to 1020.2 G and from 1028.6 G to 1030.0 G.

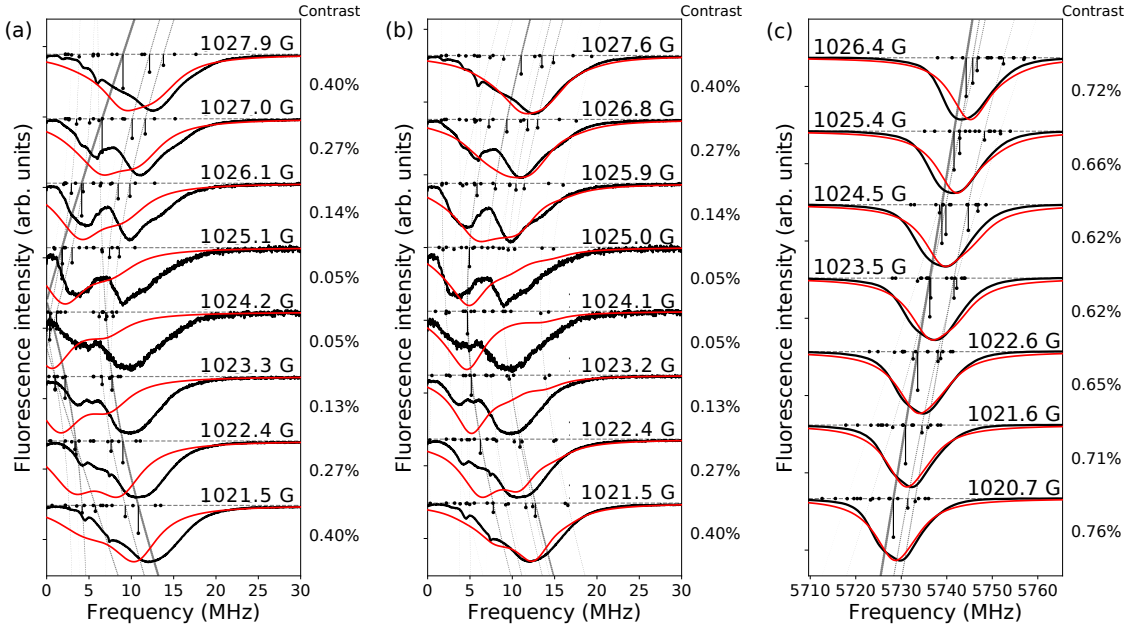

Figure 6.18: Experimental signals from the high-density sample (black) with theoretical calculations (red) in the ground-state $m_S = 0 \longrightarrow m_S = -1$ microwave-transition manifold for different magnetic-field values and for an angle between the NV axis and the magnetic-field **B** direction of (a) $\theta = 0°$ and (b) $\theta = 0.1°$ (transverse magnetic field of 1.85 G). (c) Experimental signal with the calculated signal at $\theta = 0°$ in the ground-state $m_S = 0 \longrightarrow m_S = +1$ microwave transition manifold for different magnetic-field values.

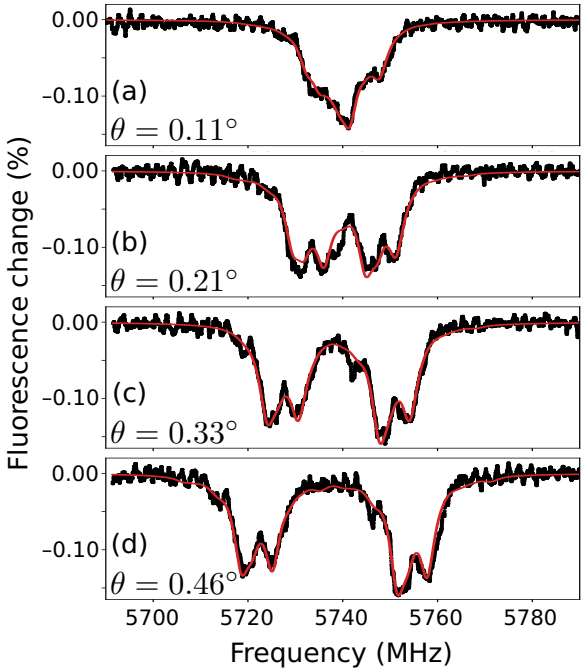

Figure 6.19: Experimental (black dots) and fitted (red curves) ODMR signals at the GSLAC (1024 G) for different angles between the magnetic field and the NV axis.

Without the ^{13}C interaction these features could not be described. A similar effect can be observed in Figure 6.20a), but the improvement is not as impressive. The interaction

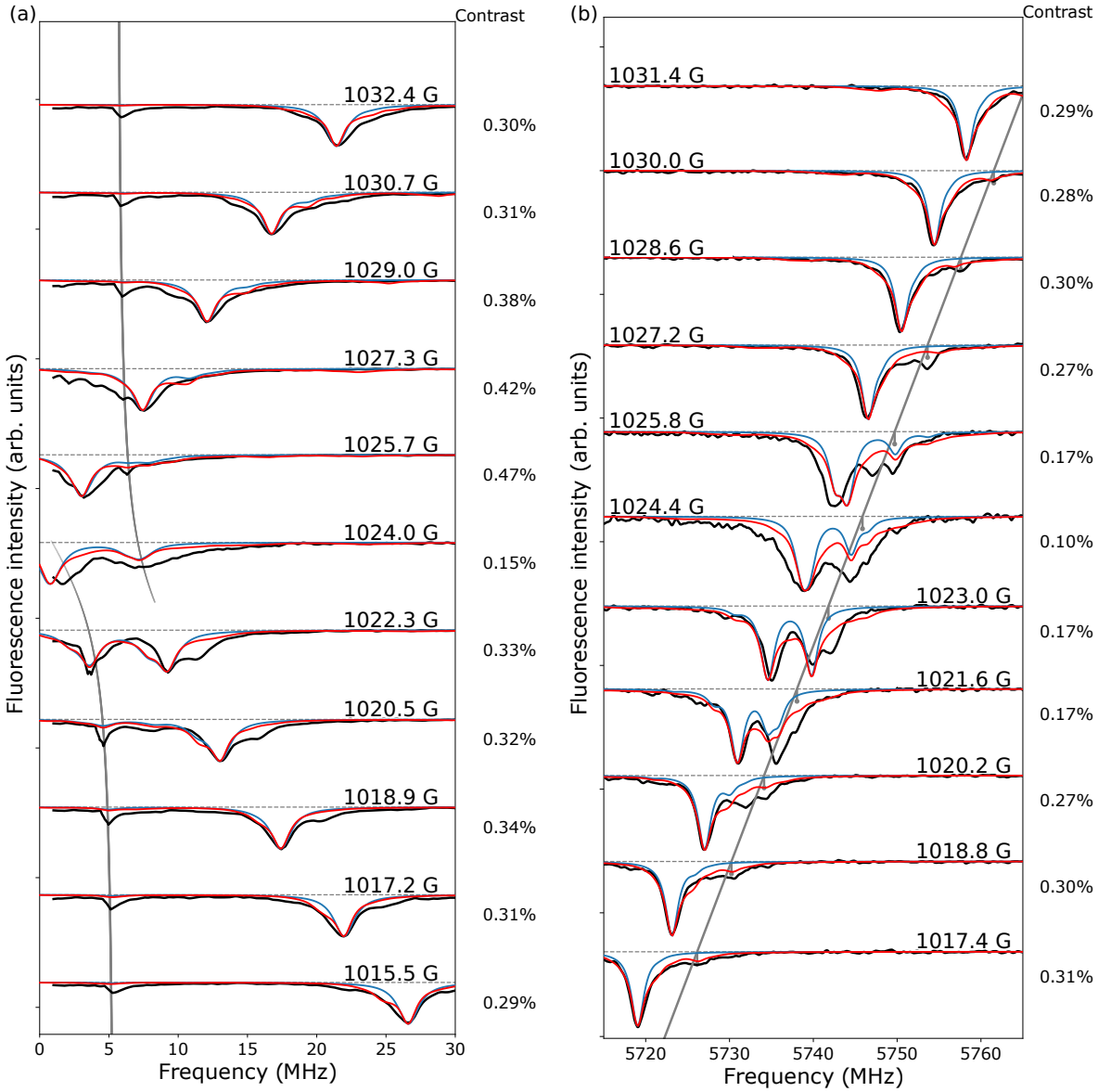

Figure 6.20: (a) Experimental signals (black) for the low-density sample with theoretical calculations that include the effects of ^{13}C (red) (6.19) and without the effects of ^{13}C (blue) for the ground-state $m_S = 0 \longrightarrow m_S = -1$ microwave transitions for different magnetic-field values. The gray line tracks the position of the nominal $|0,1\rangle \longrightarrow |0,0\rangle$ transition. (b) Experimental signals (black) for the low-density sample with theoretical calculations that include the effects of ^{13}C (red) (6.19) and without the effects of ^{13}C (blue) for the ground-state $m_S = 0 \longrightarrow m_S = +1$ microwave transitions for different magnetic-field values. The gray line tracks the position of the nominal $|0,1\rangle \longrightarrow |1,0\rangle$ transition.

of ^{13}C nuclear spin not only creates more energy levels for the system, but also allows otherwise forbidden transitions because of level mixing. Level mixing effectively changes the angular-momentum selection rules [79].

The gray curve across all graphs in Figure 6.20a tracks the nominal $|0,1\rangle \longrightarrow |0,0\rangle$ transition. This transition is clearly visible in the experimental signal. This peak also appears in the simulation, but it is so weak, that it cannot be distinguished in Figure 6.20a. The gray curve in Figure 6.20b tracks the $|0,1\rangle \longrightarrow |1,0\rangle$ transition, which appears in the experimentally measured signals but was not reproduced by any of the theoretical models.

The inclusion of ^{13}C nuclei into the model influences the strengths of the transitions that can take place and reveals important aspects of the underlying physics. As the samples used in the experiment are not chemically pure, there could be other defects and interactions that are not included in the model.

6.4 Conclusions

In this chapter we studied microwave-induced transitions between the hyperfine components of the $^3A_2$ ground-state electron-spin magnetic sublevels of the NV center in diamond by modeling the ODMR signals. The model describes the ODMR signals for magnetic field values in the vicinity of the GSLAC, where the hyperfine levels are mixed, as well as away from it. We analyzed the ODMR signal dependence on nuclear spin polarization, the width of the transitions and the angle between the magnetic field direction and NV center axis. The effects of the nearby ^{13}C nuclei were also included in the model.

The fitting of the experimentally measured data with the calculated signals was done for three diamond samples with a nitrogen concentration of 1 ppm, 200 ppm and 5–20 ppm, allowing us to determine such parameters as nuclear-spin polarization and magnetic-field angle. Moreover, the addition of the ^{13}C interaction into the model significantly improves the agreement between the experimentally measured signals and the calculations.

Within 5 G of the GSLAC, the experimentally measured ODMR spectrum becomes rather complicated with some features that we have not been able to describe fully, but the general features are reproduced at least in the case of the low-density sample. The analysis of the hyperfine-level mixing allows us to track the $|0,1\rangle \longrightarrow |1,0\rangle$ and $|0,1\rangle \longrightarrow |0,0\rangle$ transitions, although they are not reproduced by the model, which is based on selection rules $\Delta m_S = \pm 1$ and $\Delta m_I = 0$.

Possible reasons for the discrepancies in the high-density sample (Figure 6.18) might be inhomogeneity in the microwave power, in the diamond crystal lattice or in the magnetic field. Interactions with nearby spins and unknown defects might be one more reason for the failure of the model at the GSLAC for the high-density sample.

The method for determining nuclear-spin polarization in the case of the mixed states is used in the Chapter 7 to extract the nuclear-spin polarization from the experimental data.

Chapter 7

Dynamic ^{14}N nuclear spin polarization in nitrogen–vacancy centers in diamond

The sensitivity of NV centers used as a probe could be dramatically enhanced if the surrounding nuclear spins could be polarized [52], a process referred to as hyperpolarization or dynamic nuclear polarization (DNP). Success in achieving dynamic polarization of nuclei has been achieved near the excited-state level anti-crossing (ESLAC) around 512 G for single ^{15}N spins [54, 55], single ^{14}N and ^{15}N spins, and ensembles of ^{14}N and ^{13}C spins [56, 57]. The hyperfine interaction creates additional states that are strongly coupled near the level anticrossing. Previously, when nuclear-spin polarization was measured, the experimental signals have been described successfully with models based on the master equation for the density matrix [55–57], combined with the Lindblad operator [58] or even simpler rate equations [54]. Nuclear polarization is very sensitive to any angular deviations of the magnetic field from the NV axis [54], which is important to take into account in any practical applications and useful as a signal for aligning the diamond crystal in the external magnetic field. The possibilities of achieving nuclear-spin polarization at magnetic field values near the ground-state level anti-crossing (GSLAC) magnetic field region has been studied much less than, for example, the ESLAC region. Models have predicted that in the case of ^{15}N the polarization should fall as the magnetic field is increased from the ESLAC to the GSLAC, with a narrower peak at the GSLAC [55].

As was shown in Section 5.2.5, the electron spin of the NV center can be polarized through optical pumping, and the electron spin can remain polarized for a long time [41]. The polarization can be transferred from the electron spin to the nuclear spin via DNP (see Section 5.2.6). The relaxation time of the nuclear spin is even longer, which can be useful for many applications.

In this chapter we describe a model based on the Liouville equation with a Lindblad

operator, which we developed in order to calculate the nuclear-spin polarization over a wide range of magnetic-field values, including both the ESLAC and GSLAC magnetic-field regions. We calculated the dependence of nuclear-spin polarization on such parameters as the angle between the applied magnetic-field vector and the NV center's axis, the absorption rate, the transverse strain, and the relaxation rate of the intersystem-crossing. The results of the calculations were then compared with experimental results obtained at the Laser Centre of University of Latvia. The experiments were done by Reinis Lazda and Andris Berzins and are not a part of the dissertation. Nevertheless, the fitting of the experimental data was done using the procedure described in Section 6.2, and is a part of the dissertation.

The results show that nuclear-spin polarization is sensitive to transverse strain and magnetic-field angle at the level-crossing points. Because the hyperfine interaction is weaker in the ground state than in the excited state [57, 80, 81], the DNP is especially sensitive to these parameters at the GSLAC. The results of this chapter have been published in [72].

7.1 Lindblad equation model

The numerical model takes into account both the $^3A_2$ ground state and the ^3E excited state with nuclear spin $I = 1$ from the NV center's ^{14}N nucleus. The system is described using a density operator ρ in the form of a density matrix of dimension 21, which consists of nine levels in the ground states, nine in excited state, and in three the singlet state (Figure 7.1). The nine levels that compose the the ground and excited states consist of three magnetic sublevels, each of which splits into three hyperfine levels, and the singlet level consists of three hyperfine levels.

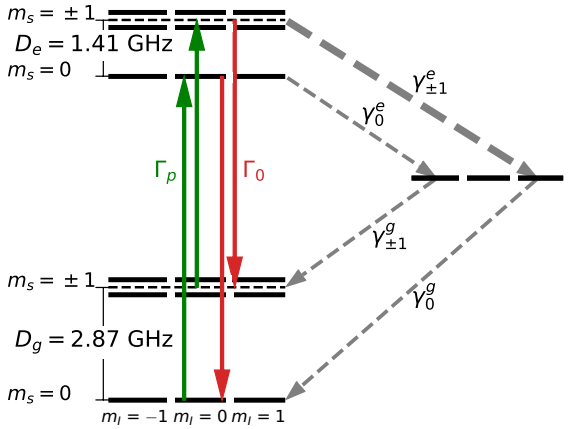

Figure 7.1: Level scheme of the NV center used in the density matrix model. Each of the electron-spin magnetic sublevels is split into three hyperfine levels, leading to 21 levels.

The density matrix is calculated from a steady-state solution of the Liouville equation (2.14) with the relaxation described by the Lindblad operator [58]:

$$\frac{\partial \rho}{\partial t} = -\frac{i}{\hbar}\left[\hat{H}, \rho\right] + \hat{L}\rho = 0, \tag{7.1}$$

where $\hat{H}$ is the Hamiltonian of the excited and ground states. (5.5). The Lindblad superoperator $\hat{L}$ [82] describes depopulation and decoherence processes of the electron spin of the NV center and the nuclear spin of the ^{14}N nucleus:

$$\hat{L}\rho = \sum_k \Gamma_k \left(\hat{L}_k \rho \hat{L}_k^\dagger - \frac{1}{2}\left\{ \hat{L}_k^\dagger \hat{L}_k, \rho \right\} \right), \tag{7.2}$$

where the indices k describe each of the relaxation processes and are denoted as $k \in \{(g_{m_S} \to e_{m_S}), \quad (e_{m_S} \to g_{m_S}), \quad (e_{m_S} \to s), \quad (s \to g_{m_S}), \quad (g_{m_S} \to g_{m'_S}), \quad (e_{m_S} \to e_{m'_S}), \quad (g_{m_I} \to g_{m'_I}), \quad (e_{m_I} \to e_{m'_I}), \quad (g_{m_S}, z_{\pm 10}), \quad (e_{m_S}, z_{\pm 10}), \quad (g_{m_I}, z_{\pm 10}), \quad (e_{m_I}, z_{\pm 10})\}$, where g, e and s stand for the ground, excited and singlet states, respectively. The indices $m_S,\ m'_S,\ m_I,\ m'_I = +1, 0, -1$ denote the projection of the electron and nuclear spins, respectively. And $z_{\pm 10}$ denotes the Pauli-z operator in the $(m_{S(I)} = \pm 1, m'_{S(I)} = 0)$ subspace, which corresponds to dephasing of these states. Γ_k are the rates of the relaxation processes and the operators $\hat{L}_k$ describe the depopulation and dephasing of the states. The quantum jump operator $\hat{L}_k = |i\rangle\langle j|$ describes the transitions between the states $|i\rangle$ and $|j\rangle$ that account for depopulation (the operator annihilates a particle in level j and creates a particle in level i). This operator describes such processes as transitions between triplet excited and ground states (fluorescence with rate Γ_0 and pumping with rate Γ_p), non-radiative transitions (intersystem crossing between triplet and singlet states) with rates γ_0^e and $\gamma_{\pm 1}^e$ from the excited triplet state to the singlet state and rates γ_0^g and $\gamma_{\pm 1}^g$ from singlet state to ground triplet state. This operator describes also the processes related to relaxation time T_1 (population transfer between magnetic sublevels in the excited and ground states for electron and nuclear spins). These operators can be written explicitly as

$$\begin{aligned}
\hat{L}_{g_{m_S} \to e_{m_S}} &= |e, m_S, m_I\rangle\langle g, m_S, m_I| \\
\hat{L}_{e_{m_S} \to g_{m_S}} &= |g, m_S, m_I\rangle\langle e, m_S, m_I| \\
\hat{L}_{e_{m_S} \to s} &= |s, m_I\rangle\langle e, m_S, m_I| \\
\hat{L}_{s \to g_{m_S}} &= |g, m_S, m_I\rangle\langle s, m_I| \\
\hat{L}_{g_{m_S} \to g_{m'_S}} &= |g, m_S, m_I\rangle\langle g, m'_S, m_I| \\
\hat{L}_{e_{m_S} \to e_{m'_S}} &= |e, m_S, m_I\rangle\langle e, m'_S, m_I| \\
\hat{L}_{g_{m_I} \to g_{m'_I}} &= |g, m_S, m_I\rangle\langle g, m_S, m'_I| \\
\hat{L}_{e_{m_I} \to e_{m'_I}} &= |e, m_S, m_I\rangle\langle e, m_S, m'_I| \,.
\end{aligned} \tag{7.3}$$

For example, we can look at the transitions between the ground-state electron-spin magnetic sublevels $m_S = 0$ and $m_s = +1$, which in this case governed by the ground-state relaxation time T_1 of the NV center's electron spin (Table 7.1). In this example, we look at a seven-level system without hyperfine structure. The state of the whole systems is written as a generalized vector with elements (in order) $|g, m_S = +1\rangle$, $|g, m_S = 0\rangle$, $|g, m_S = -1\rangle$, $|e, m_S = +1\rangle$, $|e, m_S = 0\rangle$, $|e, m_S = -1\rangle$, $|s\rangle$. The first three elements correspond to the ground state, the next three to the excited state, and the last one to the singlet state. In the model all of these levels were split into three hyperfine levels. The state $|g, m_S = 0\rangle$ can be written in generalized vector form as $(0, 1, 0, 0, 0, 0, 0)^T$, and the state $|g, m_S = +1\rangle$ as $(1, 0, 0, 0, 0, 0, 0)^T$. The jump operator then can be written in matrix form as

$$\hat{L}'_{g_{m_S=0} \to g_{m_S=+1}} = |g, m_S = 0\rangle\langle g, m_S = +1| = \begin{pmatrix} 0 & 0 & 0 & 0 & 0 & 0 & 0 \\ 1 & 0 & 0 & 0 & 0 & 0 & 0 \\ 0 & 0 & 0 & 0 & 0 & 0 & 0 \\ 0 & 0 & 0 & 0 & 0 & 0 & 0 \\ 0 & 0 & 0 & 0 & 0 & 0 & 0 \\ 0 & 0 & 0 & 0 & 0 & 0 & 0 \\ 0 & 0 & 0 & 0 & 0 & 0 & 0 \end{pmatrix} \tag{7.4}$$

To include the hyperfine levels, we use the Kronecker product

$$\hat{L}_{g_{m_S=0} \to g_{m_S=+1}} = \hat{L}'_{g_{m_S=0} \to g_{m_S=+1}} \otimes \hat{\mathbb{1}}(3),$$

where $\hat{\mathbb{1}}(3)$ is a three-dimensional identity matrix, which adds hyperfine levels and provides the selection rule for the relaxation: $\Delta m_I = 0$.

The operator $\hat{L}_k = |i\rangle\langle i| - |j\rangle\langle j|$ describes the T_2-related processes in the ground and excited states for electronic and nuclear spin, which corresponds to dephasing of the $|i\rangle$ and $|j\rangle$ states. The dephasing operators are

$$\begin{aligned} \hat{L}_{g_{m_S}, z_{\pm 10}} &= |g, \pm 1, m_I\rangle\langle g, \pm 1, m_I| - |g, 0, m_I\rangle\langle g, 0, m_I| \\ \hat{L}_{e_{m_S}, z_{\pm 10}} &= |e, \pm 1, m_I\rangle\langle e, \pm 1, m_I| - |e, 0, m_I\rangle\langle e, 0, m_I| \\ \hat{L}_{g_{m_I}, z_{\pm 10}} &= |g, m_S, \pm 1\rangle\langle g, m_S, \pm 1| - |g, m_S, 0\rangle\langle g, m_S, 0| \\ \hat{L}_{e_{m_I}, z_{\pm 10}} &= |e, m_S, \pm 1\rangle\langle e, m_S, \pm 1| - |e, m_S, 0\rangle\langle e, m_S, 0| \,. \end{aligned} \tag{7.5}$$

To take a similar example, we can look at a dephasing between ground-state electron-spin levels $m_S = 0$ and $m_S = +1$. In matrix form it can be written as

$$\hat{L}'_{g_{m_S}, z_{\pm 10}} = |g, m_S = +1\rangle\langle g, m_S = +1| - |g, m_S = 0\rangle\langle g, m_S = 0| = \begin{pmatrix} 1 & 0 & 0 & 0 & 0 & 0 & 0 \\ 0 & -1 & 0 & 0 & 0 & 0 & 0 \\ 0 & 0 & 0 & 0 & 0 & 0 & 0 \\ 0 & 0 & 0 & 0 & 0 & 0 & 0 \\ 0 & 0 & 0 & 0 & 0 & 0 & 0 \\ 0 & 0 & 0 & 0 & 0 & 0 & 0 \\ 0 & 0 & 0 & 0 & 0 & 0 & 0 \end{pmatrix} \tag{7.6}$$

Similarly as before, we can use the Kronecker product to include hyperfine levels $\hat{L}_{g_{m_S},z_{\pm 10}} = \hat{L}'_{g_{m_S},z_{\pm 10}} \otimes \hat{\mathbb{1}}(3)$.

Table 7.1 shows the values of the transition rates [69, 83] and the time constants T_1 and T_2 [84, 85] used in the calculations. The relaxation rates associated with T_1 and T_2 processes are $1/T_1$ and $1/T_2$.

Process	Operator $\hat{L}_k$	Rate Γ_k (Time)	
Spin conserving transitions Γ_0	$\|g, m_S, m_I\rangle\langle e, m_S, m_I\|$	66 MHz	[69]
Excited state to singlet $\gamma^e_{\pm 1}$	$\|s, m_I\rangle\langle e, \pm 1, m_I\|$	53 MHz	[69]
Excited state to singlet γ^e_0	$\|s, m_I\rangle\langle e, 0, m_I\|$	7.9 MHz	[69]
Singlet to ground state γ^g_0	$\|g, 0, m_I\rangle\langle s, m_I\|$	1.0 MHz	[69]
Singlet to ground state $\gamma^g_{\pm 1}$	$\|g, \pm 1, m_I\rangle\langle s, m_I\|$	0.7 MHz	[69]
Ground state NV electron spin depopulation (T_1)	$\|g, m_S, m_I\rangle\langle g, m'_S, m_I\|$	0.1 kHz (10 ms)	[84]
Ground state NV electron spin dephasing (T_2)	$\|g, 0, m_I\rangle\langle g, 0, m_I\| - \|g, \pm 1, m_I\rangle\langle g, \pm 1, m_I\|$	10 kHz (100 µs)	[84]
Ground state ^{14}N nuclear spin depopulation (T_1)	$\|g, m_S, m_I\rangle\langle g, m_S, m'_I\|$	0.1 Hz (10 s)	[84]
Ground state ^{14}N nuclear spin dephasing (T_2)	$\|g, m_S, 0\rangle\langle g, m_S, 0\| - \|g, m_S, \pm 1\rangle\langle g, m_S, \pm 1\|$	0.1 kHz (10 ms)	[84]
Excited state NV electron spin depopulation (T_1)	$\|e, m_S, m_I\rangle\langle e, m'_S, m_I\|$	1 kHz (1 ms)	[85]
Excited state NV electron spin dephasing (T_2)	$\|e, 0, m_I\rangle\langle e, 0, m_I\| - \|e, \pm 1, m_I\rangle\langle e, \pm 1, m_I\|$	92 MHz (11.9 ns)	[86]
Excited state ^{14}N nuclear spin depopulation (T_1)	$\|e, m_S, m_I\rangle\langle e, m_S, m'_I\|$	10 Hz (100 ms)	[85]
Excited state ^{14}N nuclear spin dephasing (T_2)	$\|e, m_S, 0\rangle\langle e, m_S, 0\| - \|e, m_S, \pm 1\rangle\langle e, m_S, \pm 1\|$	1kHz (1 ms)	[85]

Table 7.1: Transition and decoherence rates used in the calculation.

The nuclear-spin polarization of the $m_S = 0$ electron state is calculated from the steady-state solution of the density matrix as

$$P_{th} = \frac{\rho_{01} - \rho_{0-1}}{\rho_{01} + \rho_{00} + \rho_{0-1}}, \tag{7.7}$$

where $\rho_{m_S m_I} = \langle g, m_S, m_I | \rho_{SS} | g, m_S, m_I \rangle$ is the population of the ground-state basis state $|g, m_S, m_I\rangle$. The calculations of the Lindblad equation model let us explore the influence of different system parameters on nuclear-spin polarization.

The system of linear equations was solved using the `Python` library `QuTip` [87].

7.1.1 Dependence of nuclear-spin polarization on magnetic field angle

One of the parameters that was explored through the calculations was the angle between the magnetic-field direction and the NV center's principal axis.

If the NV center axis is aligned along the magnetic field, high nuclear-spin polarization can be achieved. However, a precise alignment is not always easy to achieve because of difficult-to-control factors such a magnetic-field inhomogeneities. Thus, it is important to examine the influence of the angle between the magnetic-field direction and the NV center's principal axis.

As can be seen in Figure 7.2, the magnetic-field angle influences the nuclear-spin polarization both at the ESLAC and the GSLAC. The transverse magnetic field introduces

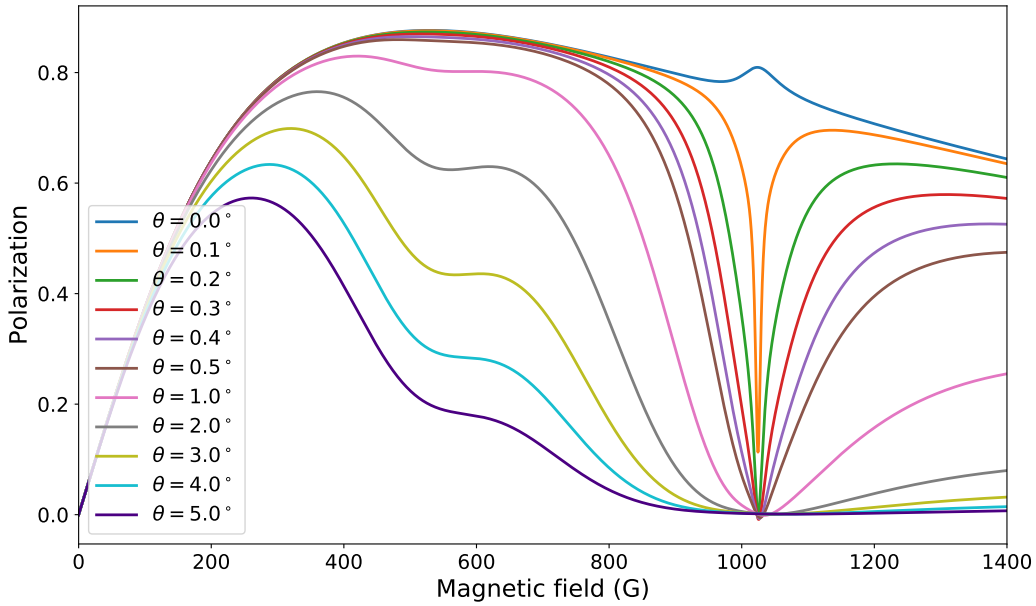

Figure 7.2: Calculation of nuclear-spin polarization for different magnetic-field angles. Sweeping the magnetic-field angle over the range $\theta = 0° - -0.5°$ with step size 0.1° causes rapid changes in nuclear-spin polarization at GSLAC. Further increasing the angle from $\theta = 1°$ to $\theta = 5°$ with step size 1° causes changes at the ESLAC, but more slowly.

additional interaction between the hyperfine levels, leading to more hyperfine levels being mixed, which strongly modifies the polarization process.

If we look more closely at the GSLAC region, it can be seen that polarization at the GSLAC is $\sim 85\%$ for a magnetic-field angle of $\theta = 0°$. The polarization decreases significantly at $\theta = 0.1°$ and approaches almost 0% for $\theta = 0.2°$. The excited state has much a stronger hyperfine interaction [57], so the ESLAC region is not as sensitive to such small angles. A noticeable dip at the ESLAC can be seen for a magnetic-field angle of $\theta = 1°$. When the magnetic-field angle is increased even more, the nuclear spin polarization decreases, and the maximum is shifted to lower magnetic field values.

7.1.2 Dependence of nuclear-spin polarization on transition rates

The electron-spin polarization depends on the intersystem transition rates γ_0^e, $\gamma_\pm^e$, γ_0^g, and $\gamma_\pm^g$. These rates determine the transfer of population between the $m_S = 0$ and $m_S = \pm 1$ sublevels. This process can be explained by looking at the transition rates shown in Figure 7.3b. The electron-spin polarization is determined by the rate of transitions between ground-state magnetic sublevels $m_S = \pm 1 \rightarrow m_S = 0$ and $m_S = 0 \rightarrow m_S = \pm 1$, which are indicated by $\gamma_{\pm 1 \rightarrow 0}$ and $\gamma_{0 \rightarrow \pm 1}$, respectively. These rates can be expressed

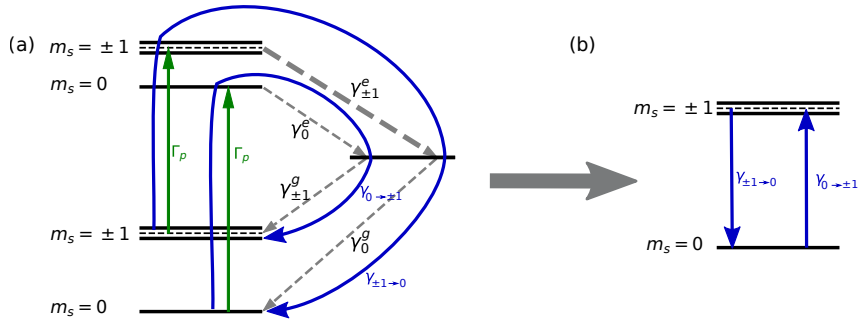

Figure 7.3: Visualization of the influence of transition rates on electron-spin polarization.

(Figure 7.3a) as

$$\begin{aligned} \gamma_{\pm 1\to 0} &= \Gamma_p \cdot \gamma^e_{\pm 1} \cdot \gamma^g_0 \\ \gamma_{0\to\pm 1} &= \Gamma_p \cdot \gamma^e_0 \cdot \gamma^g_{\pm 1} \end{aligned} \tag{7.8}$$

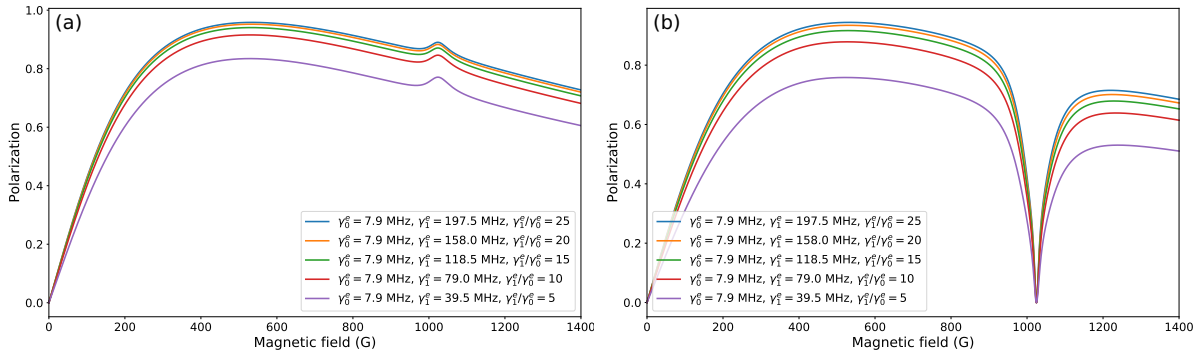

Figure 7.4: Theoretical nuclear-spin polarization for different ratios of transition rates $\frac{\gamma^e_{\pm 1}}{\gamma^e_0}$ with the angle between the NV center's axis and the magnetic-field vector: (a) $\theta = 0.0°$, (b) $\theta = 0.2°$. The pumping rate for numerical calculations was $\Gamma_p = 5$ MHz. The transition rates from the singlet state to the ground-state sublevel $m_S = 0$ and from the singlet state to ground-state sublevels $m_S = \pm 1$ are $\gamma^g_0 = 1$ MHz and $\gamma^g_\pm = 1$ MHz.

As the transition rates γ^e_0, $\gamma^e_\pm$, γ^g_0 and $\gamma^g_\pm$ are not precisely known and can differ between diamond samples, it is important to investigate the influence of the ratio of the rates from the ground-state magnetic sublevels $m_S = \pm 1$ to the ground-state magnetic sublevel $m_S = 0$ versus ground-state magnetic sublevel $m_S = 0$ to ground-state magnetic sublevel $m_S = \pm 1$. The ratio between these transition rates can be expressed as

$$\frac{\gamma_{\pm 1\to 0}}{\gamma_{0\to\pm 1}} = \frac{\Gamma_p \cdot \gamma^e_{\pm 1} \cdot \gamma^g_0}{\Gamma_p \cdot \gamma^e_0 \cdot \gamma^g_{\pm 1}} = \frac{\gamma^e_{\pm 1} \cdot \gamma^g_0}{\gamma^e_0 \cdot \gamma^g_{\pm 1}}. \tag{7.9}$$

As the transition rates from singlet state to ground-state sublevels $m_S = 0$ and from the singlet state to ground-state sublevels $m_S = \pm 1$ are typically on the order of 1 MHz

and their ratio $\frac{\gamma_0^g}{\gamma_\pm^g}$ is typically in the range $1.1-2.0$ [57, 69], both of these transitions rates were set to $\gamma_0^g = 1$ MHz and $\gamma_\pm^g = 1$ MHz in the calculations for Figure 7.4. Then, the calculations were performed for different ratios of transition rates from the excited state to the singlet state $\frac{\gamma_{\pm1}^e}{\gamma_0^e}$, which is equivalent to the ratio $\frac{\gamma_{\pm1\to0}}{\gamma_{0\to\pm1}}$ (7.9). Figure 7.4 shows the influence of the ratio of transition rates from the excited state to the singlet state $\frac{\gamma_{\pm1}^e}{\gamma_0^e}$ on the nuclear-spin polarization. As the ratio increases, so the electron-spin polarization increases (Figure 7.3b), and, in turn, the nuclear-spin polarization also increases. The ratio of transition rates influences the nuclear spin polarization proportionally for the whole range of magnetic-field values. Figure 7.4 shows the theoretical nuclear-spin polarization for different transition-rate ratios $\frac{\gamma_{\pm1}^e}{\gamma_0^e}$ with the angle between the NV center axis and magnetic field vector being $\theta = 0.0°$ (Figure 7.4a) and $\theta = 0.2°$ (Figure 7.4b).

7.1.3 Dependence of nuclear-spin polarization on transverse strain

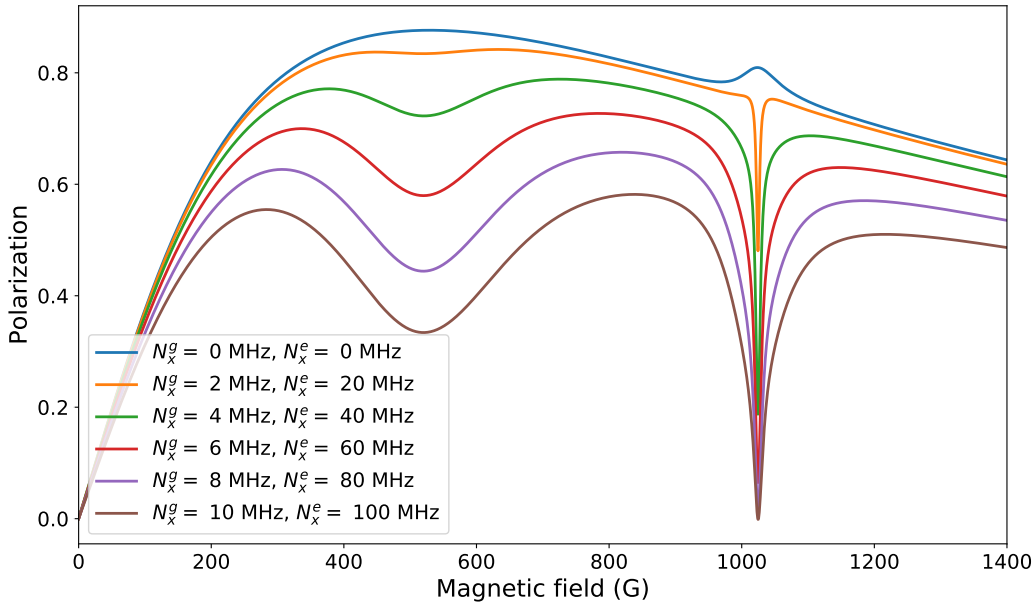

Figure 7.5: Theoretical nuclear-spin polarization for different transverse strain values. The pumping rate for the numerical calculations was $\Gamma_p = 5$ MHz.

The spin-strain interaction [59–63] can cause a similar effect as the transverse magnetic field. A transverse spin-strain coupling constants N_x and N_y (5.13) couples magnetic sublevels $m_s = 0$ and $m_s = \pm1$. Due to the C_{3v} symmetry of the NV center, we can choose the coordinate system such that only the term N_x is non-zero. At the level-crossing points, where the energy difference between levels $m_s = 0$ and $m_s = -1$ is small, the spin-strain

interaction component N_x leads to level mixing similar to what is produced by a transverse magnetic field. The strain induced interaction component N_x influences the nuclear-spin polarization at both the ESLAC and the GSLAC as can be seen in Figure 7.5. The strain induced interaction strength between electron spin states in the ground state is typically in the range of a few megahertz, whereas in the excited-state it is on the order of a few tens of megahertz [68, 88]. To calculate the influence of strain on nuclear-spin polarization at the level crossing points, the excited-state spin-strain coupling constant was set to be $N_x^e = 10N_x^g$, which corresponds to the different order of magnitude of strain coupling constants in the ground and excited states. Even small transverse strain can significantly decrease the nuclear-spin polarization at GSLAC and ESLAC regions.

7.1.4 Dependence of the nuclear-spin polarization on pumping rate

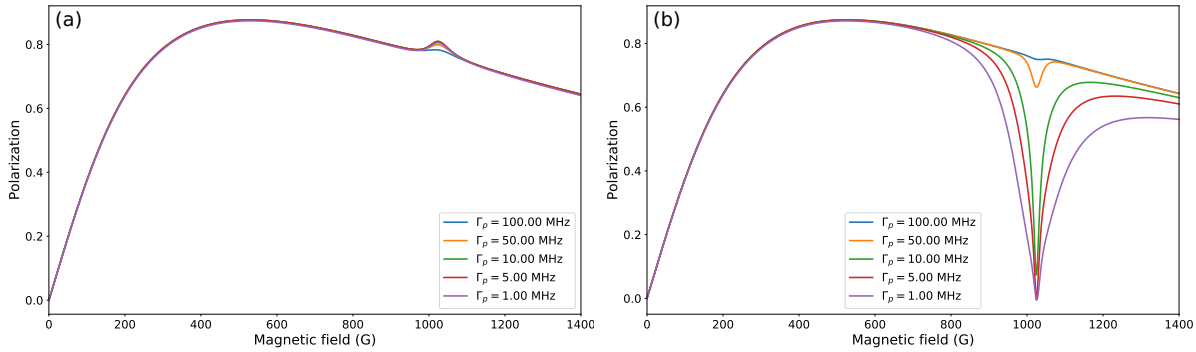

Figure 7.6: Theoretical nuclear-spin polarization for different pumping rates with the angle between the NV center axis and magnetic field being (a) $\theta = 0.0°$ and (b) $\theta = 0.2°$.

For an ideal NV center whose principal axis is aligned along the magnetic field direction, the nuclear-spin polarization is not strongly influenced by the pumping rate Γ_p, which characterizes the power of the pumping laser (Figure 7.6a). However, if the magnetic field is only slightly misaligned, the nuclear-spin polarization at the GSLAC is sensitive to the pumping rate. The calculated nuclear spin polarization for different pumping rates with an angle between the magnetic-field vector and the NV-center axis of $\theta = 0.2°$ can be seen in Figure 7.6b.

7.2 Testing the model against experimental data

The experiment was carried out by Reinis Lazda and Andris Berzins at the Laser Centre of the University of Latvia. The experimental setup is described in Appendix A.3.

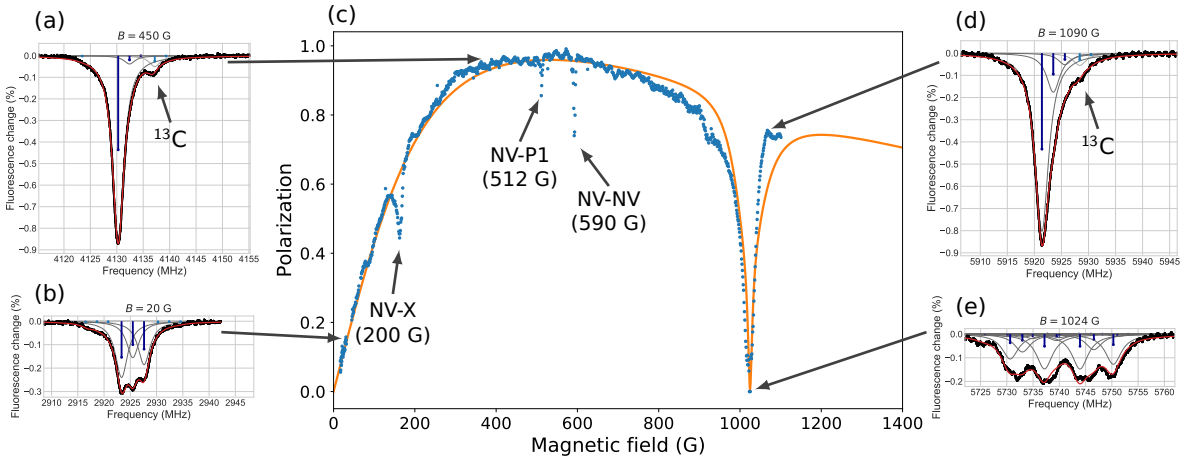

Figure 7.7: (a), (b), (d), (e): Experimental (black dots) and fitted (red curves) ODMR signals at individual magnetic field values. (c): Experimental (blue dots) and theoretical (orange curve) nuclear spin polarization. The pumping rate used in the theoretical calculations was $\Gamma_p = 5$ MHz. The magnetic-field angle $\theta = 0.2°$ was determined from the ODMR curve fit.

The nuclear-spin polarization was determined from the ODMR signals of the $|m_s = 0\rangle \longrightarrow |m_s = +1\rangle$ transition (Figure 7.7a,b,d,e) by fitting the experimental signals (black dots) with a modeled ODMR curve (red curve). The model of the ODMR signals is described in detail in Section 6.2. The modeled curve is a sum of Lorentzian curves each of whose central frequencies are the corresponding hyperfine transition frequencies ω_i (6.17). The resonance amplitudes t_i (6.15) are expressed as a product of the transition probabilities p_i and the relative populations $N_i(m_I)$ of hyperfine basis states.

The hyperfine-level transition probabilities p_i and transition frequencies ω_i were calculated from the eigenfunctions and eigenvalues of the ground-state Hamiltonian (5.5), while taking into account the selection rules for the electron- and nuclear-spin magnetic dipole transitions $\Delta m_S = \pm 1$ and $\Delta m_I = 0$ (see Section 6.2).

The experimental signals were fitted as described in Section 6.3.1, whiche made it possible to determine the relative populations of the basis states, to calculate the experimental nuclear-spin polarization (6.16), and to determine the angle θ between magnetic field vector and the NV center's axis (5.11).

Far from the GSLAC, we can observe three hyperfine transitions in each ODMR signal, so that each of the basis states m_I is involved in a single transition. When the ground state's magnetic sublevels $|m_S = 0\rangle$ and $|m_s = -1\rangle$ are mixed at the GSLAC, more than three components are observed (Figure 7.7e), so it is crucial to take the mixing into account when fitting the experimental signals. Extracting the relative populations of the basis states from the experimental signals allowed us to directly compare the ex-

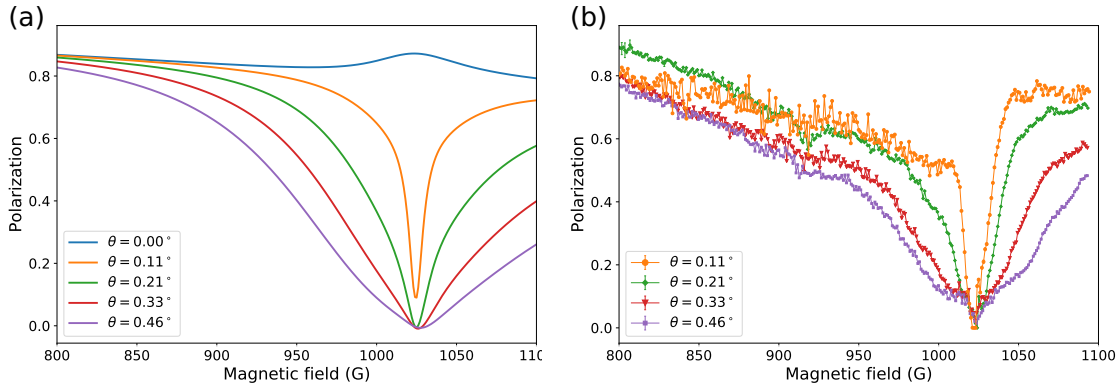

Figure 7.8: (a) Calculated and (b) experimentally determined nuclear spin polarization for different magnetic field angles. Pumping rate for numerical calculations was $\Gamma_p = 5$ MHz.

perimentally determined nuclear-spin polarization (6.16) with the theoretically calculated nuclear-spin polarization (7.7).

As can be seen in Figure 7.7b, at low magnetic field values (around 20 G), the amplitudes of the three hyperfine-transition amplitudes are almost equal, which indicates that the ^{14}N nuclei are largely unpolarized. At magnetic-field values near the ESLAC (Figure 7.7a) there is one dominant transition, and the ODMR signal contrast has increased by a factor of around three. The large, single peak can be explained by population accumulation in the $m_I = +1$ state, which leads to a high ^{14}N nuclear-spin polarization of $96 \pm 2\%$. The ODMR signal at the GSLAC (Figure 7.7e) was used to determine the experimental magnetic field angle, which was found to be $\theta = 0.2°$.

As the diamond crystal used in the experiment had a natural abundance of carbon, 1.1% of carbon atoms were ^{13}C isotopes (Section 6.2.3). The influence of ^{13}C can be seen in the ODMR signal as an extra feature next to the main peak (Figure 7.7a).

The experiment was performed in the magnetic field range from 0 to 1100 G, including both the ESLAC and GSLAC regions. Each of the blue dots in Figure 7.7c correspond to a measurement of the ODMR signal, which was then fitted using the model described in Section 6.2 to calculate the experimental nuclear-spin polarization. At 512 G a drop in polarization can be observed, which is due to the NV center interaction with substitutional nitrogen (P1 center) in the crystal lattice and cross-relaxation between the NV and P1 centers [51, 89, 90]. At around 590 G a drop in polarization occurs due to the ground-state energy matching of NV centers with principal axis along the **B** direction and the NV centers that point along the other three possible directions in the diamond crystal [91]. The decrease in polarization around 200 G is thought to be due to cross-relaxation with other unknown paramagnetic defect centers in the crystal [91–93].

To calculate the orange curve of Figure 7.7c, the T_1, and T_2 times, as well as transition rate Γ_0 were taken from the Table 7.1, but the intersystem transition rates were

fitted to match the typical electronic spin polarization observed in experiments [94]. As explained in Section 7.1.2, the ratio of singlet to triplet ground states was set to $\frac{\gamma_0^g}{\gamma_\pm^g} = 1$, and the ratio of transitions of the excited state to the singlet state $\frac{\gamma_{\pm1}^e}{\gamma_0^e}$ was adjusted. To achieve the best fit with the experimental data, it was set to be $\frac{\gamma_{\pm1}^e}{\gamma_0^e} = 20$ in the calculation. It is close to the value used in [56], but deviates from the transition rates in [69]. The pumping rate for the numerical calculations was determined from the fit to be $\Gamma_p = 5$ MHz. The magnetic-field angle used to calculate the theoretical curve was $\theta = 0.2°$.

The dependence of nuclear-spin polarization on magnetic-field angle was measured in the vicinity of the GSLAC. The experimental data exhibit the same tendency as the theoretically predicted curves, showing that even a small magnetic-field angle strongly influences the nuclear spin polarization at the GSLAC (Figure 7.8).

7.3 Conclusions

Aside from the intrinsic interest in dynamic nuclear-spin polarization as an effect that takes place in NV centers, it has the potential to be used in important applications. For example, nuclear-spin polarization strongly increases the sensitivity of NMR methods could be of use in quantum technologies [95]. Thus, the motivation to investigate the DNP in detail was twofold. In order to understand better this effect and be able to simulate potential applications, we developed a model based on the Liouville equations with a Lindblad operator that describes DNP over a wide range of magnetic-field values, including the hyperfine interaction of both the ground and excited states. We investigated the influence on the nuclear-spin polarization of the angle between the magnetic-field direction and the NV center's principal axis, transverse strain, internal transition rates and pumping rate. The level mixing in the ground state due to the hyperfine interaction is weaker than in the excited state, which leads to higher sensitivity to the external parameters at the GSLAC compared to the ESLAC. The calculation as well as experimental data show that even a small magnetic-field angle of $\sim 0.1°$ almost completely destroys the nuclear-spin polarization at the GSLAC, while a $\sim 1°$ angle causes only a small dip in the nuclear polarization curve at the ESLAC (Figure 7.2). The transverse strain can cause an effect that is similar to magnetic-field misalignment as it mixes the same hyperfine levels as the transverse component of magnetic field.

The results of the calculations were compared with experimental results obtained from ODMR signals using the fitting procedure described in Section 6.3.1. In this way we could validate again the model for microwave transitions over a wide range of magnetic-field values, and determine the nuclear-spin polarization from experimental signals. The

results of this research shed light on nuclear-spin polarization, particularly near the less studied GSLAC. The results contribute to understanding nuclear-spin polarization processes. They also underlined the influence of magnetic field and strain on the achievable polarization; these effects must be taken into account in order to improve the efficiency of NV-center applications.

Main results

The main results of this thesis are:

1. It was shown that the theoretical model of nonlinear magneto-optical rotation, based on the analysis of the resolved and unresolved hyperfine structure and accounting for Doppler broadening, can be adapted to describe the experimental measurements of blue-light NMOR in rubidium vapor in the presence of an external magnetic field.

    - It was established that the repopulation of the ground state through spontaneous processes can be characterized by a single parameter, replacing the cascade transition rates through intermediate states with a single parameter that corresponds to a direct transition. This simplification is possible, because in each subsequent transition involved in the cascade, atomic angular momentum polarization significantly decreases.
    - The analysis of experimental parameters showed that after adapting the model by taking into account the beam profile, the model described experimental results well.

2. The analysis of the ODMR signals of NV centers in the vicinity of ground-state hyperfine-level anticrossing provided an understanding of the hyperfine-level mixing due to joint action of internal interactions in the NV centers and the external magnetic field.

    - The probabilities of microwave-field induced transition between electron level hyperfine components were significantly altered due to the level mixing leading to more complex ODMR signals, which can be modeled by taking into account the level mixing.
    - The analysis of the modeled signals showed that the shape of the ODMR signals is affected by nitrogen nuclear-spin polarization, the characterizing relaxation time T_2^*, and magnetic-field misalignment with respect to the NV center's principal axis.

3. Employing the numerical model based on the Liouville equation with a Lindblad operator, it was shown that strong ^{14}N nuclear-spin polarization can be observed

over a wide range of magnetic-field values, including both excited- and ground-state level anticrossing magnetic-field regions.

- Nevertheless, even a small misalignment of the magnetic field with respect to the NV center's principal axis destroys almost completely the nuclear-spin polarization in the vicinity of the GSLAC.
- Transverse strain can also cause an effect similar to that of magnetic-field misalignment.

Theses

1. It is necessary to take into account the beam-profile distribution in order to provide a more precise theoretical description of nonlinear magneto-optical rotation, based on the analysis of the resolved and unresolved hyperfine structure that describes the experimental measurements of blue light nonlinear magneto-optical rotation in rubidium vapor in the presence of an external magnetic field.

2. The mixing of hyperfine levels is responsible for the peak structure of optically detected magnetic resonance signals in the vicinity of the ground-state level anti-crossing, and these signals can be used to estimate the ^{14}N nuclear-spin polarization, relaxation time T_2^* (signal width) and magnetic-field misalignment with nitrogen–vacancy center's principal axis.

3. A numerical model based on the Lindblad equation, applicable over wide range of magnetic-field-strength values, shows that a high degree of ^{14}N dynamic nuclear-spin polarization in the vicinity of the ground-state level anti-crossing is possible in principle, but a tiny misalignment of the magnetic field with nitrogen–vacancy center principal axis or transverse strain almost completely destroys the dynamic nuclear polarization.

Bibliography

[1] J. R. Maze, A. Gali, E. Togan, Y. Chu, A. Trifonov, E. Kaxiras, and M. D. Lukin, "Properties of nitrogen-vacancy centers in diamond: The group theoretic approach," New Journal of Physics, vol. 13, p. 30, 10 2011.

[2] A. Gali, M. Fyta, and E. Kaxiras, "Ab initio supercell calculations on nitrogen-vacancy center in diamond: Electronic structure and hyperfine tensors," Physical Review B, vol. 77, p. 155206, 4 2008.

[3] A. P. Nizovtsev, S. Ya Kilin, A. L. Pushkarchuk, V. A. Pushkarchuk, and F. Jelezko, "Theoretical study of hyperfine interactions and optically detected magnetic resonance spectra by simulation of the C 291 [NV] - H 172 diamond cluster hosting nitrogen-vacancy center," New Journal of Physics, vol. 16, p. 083014, 8 2014.

[4] D. Budker and M. Romalis, "Optical magnetometry," Nature Physics, vol. 3, no. 4, pp. 227–234, 2007.

[5] S. Pustelny, M. Koczwara, L. Cincio, and W. Gawlik, "Tailoring quantum superpositions with linearly polarized amplitude-modulated light," Phys. Rev. A, vol. 83, p. 43832, 4 2011.

[6] T. Zigdon, a. D. Wilson-Gordon, S. Guttikonda, E. J. Bahr, O. Neitzke, S. M. Rochester, and D. Budker, "Nonlinear magneto-optical rotation in the presence of a radio-frequency field.," Optics express, vol. 18, pp. 25494–508, 12 2010.

[7] M. Auzinsh, D. Budker, and S. M. Rochester, "Light-induced polarization effects in atoms with partially resolved hyperfine structure and applications to absorption, fluorescence, and nonlinear magneto-optical rotation," Physical Review A - Atomic, Molecular, and Optical Physics, vol. 80, pp. 1–22, 11 2009.

[8] M. Auzinsh, D. Budker, and S. M. Rochester, Optically Polarized Atoms: Understanding Light–Atom Interactions. Oxford University Press, 2010.

[9] D. Budker, W. Gawlik, D. F. Kimball, S. M. Rochester, V. Yashchuk, and A. Weis, "Resonant nonlinear magneto-optical effects in atoms," Reviews of Modern Physics, vol. 74, pp. 1153–1201, 11 2002.

[10] V. V. Yashchuk, D. Budker, W. Gawlik, D. F. Kimball, Y. P. Malakyan, and S. M. Rochester, "Selective Addressing of High-Rank Atomic Polarization Moments," p. 25, 2003.

[11] A. Wojciechowski, E. Corsini, J. Zachorowski, and W. Gawlik, "Nonlinear Faraday rotation and detection of superposition states in cold atoms," PHYSICAL REVIEW A, vol. 81, p. 53420, 2010.

[12] W. Gawlik and A. Wojciechowski, "Experiments on quantum coherence with cold atoms," Optics and Spectroscopy (English translation of Optika i Spektroskopiya), vol. 111, pp. 626–632, 10 2011.

[13] K. Takahashi, B. J. Anderson, and K. Yumoto, "Upper Atmosphere Research Satellite observation of a Pi2 pulsation," Journal of Geophysical Research: Space Physics, vol. 104, no. A11, pp. 25035–25045, 1999.

[14] M. Gajdacz, P. L. Pedersen, T. Mørch, A. J. Hilliard, J. Arlt, and J. F. Sherson, "Non-destructive Faraday imaging of dynamically controlled ultracold atoms," Review of Scientific Instruments, vol. 84, p. 083105, 8 2013.

[15] D. Budker, L. Hollberg, D. F. Kimball, J. Kitching, S. Pustelny, and V. V. Yashchuk, "Microwave transitions and nonlinear magneto-optical rotation in anti-relaxation-coated cells*,"

[16] S. Pustelny, D. Jackson Kimball, S. Rochester, V. Yashchuk, W. Gawlik, and D. Budker, "Pump-probe nonlinear magneto-optical rotation with frequency-modulated light," Physical Review A, vol. 73, p. 023817, 2 2006.

[17] M. V. Balabas, K. Jensen, W. Wasilewski, H. Krauter, L. S. Madsen, J. H. Müller, T. Fernholz, and E. S. Polzik, "High quality anti-relaxation coating material for alkali atom vapor cells," Optics Express, vol. 18, p. 5825, 3 2010.

[18] W. Chalupczak, P. Josephs-Franks, R. M. Godun, and S. Pustelny, "Radio-frequency spectroscopy in the dark," PHYSICAL REVIEW A, vol. 88, p. 52508, 2013.

[19] S. Knappe, P. Schwindt, V. Shah, L. Hollberg, J. Kitching, L. Liew, and J. Moreland, "A chip-scale atomic clock based on 87Rb with improved frequency stability.," Optics express, vol. 13, pp. 1249–53, 2 2005.

[20] A. Cerè, V. Parigi, M. Abad, F. Wolfgramm, A. Predojević, and M. W. Mitchell, "Narrowband tunable filter based on velocity-selective optical pumping in an atomic vapor," Opt. Lett., vol. 34, pp. 1012–1014, 4 2009.

[21] L. Krzemień, K. Brzozowski, A. Noga, M. Witkowski, J. Zachorowski, M. Zawada, and W. Gawlik, "Laser frequency stabilization by magnetically assisted rotation spectroscopy," Optics Communications, vol. 284, pp. 1247–1253, 3 2011.

[22] L. R. HUNTER, "Tests of Time-Reversal Invariance in Atoms, Molecules, and the Neutron," Science, vol. 252, no. 5002, pp. 73–79, 1991.

[23] M. A. Bouchiat, J. Guéna, P. Jacquier, M. Lintz, and M. D. Plimmer, "Two-beam linear magneto-optical spectroscopy of atomic transitions between short lived states," Zeitschrift für Physik D Atoms, Molecules and Clusters, vol. 33, no. 2, pp. 89–95, 1995.

[24] P. Herczeg, C. M. Hoffman, and H. V. Klapdor-Kleingrothaus, Physics Beyond the Standard Model: Proceedings of the Fifth International Wein Symposium High Energy Physics Series, World Scientific Publishing Company, Incorporated, 1999.

[25] A. Yoshimi, T. Nanao, T. Inoue, T. Furukawa, M. Uchida, M. Tsuchiya, H. Hayashi, M. Chikamori, and K. Asahi, "Development of NMOR magnetometer for spin-maser EDM experiment," in Physics Procedia, vol. 17, pp. 245–250, Elsevier B.V., 1 2011.

[26] H. Ravi, M. Bhattarai, A. Y. D, U. Momeen, and V. Natarajan, "Permanent EDM measurement in Cs using nonlinear magneto-optic rotation," 1 2015.

[27] S. Pustelny, D. F. Jackson Kimball, C. Pankow, M. P. Ledbetter, P. Wlodarczyk, P. Wcislo, M. Pospelov, J. R. Smith, J. Read, W. Gawlik, and D. Budker, "The Global Network of Optical Magnetometers for Exotic physics (GNOME): A novel scheme to search for physics beyond the Standard Model," Ann. Phys., no. 525, p. 659–670, 2013.

[28] J. Barrat and C. Cohen-Tannoudji, "Étude Du Pompage Optique Dans Le Formalisme De La Matrice Densité," Journal de Physique et le Radium, vol. 22, no. 6, pp. 329–336, 1961.

[29] S. Pustelny, L. Busaite, M. Auzinsh, A. Akulshin, N. Leefer, and D. Budker, "Nonlinear magneto-optical rotation in rubidium vapor excited with blue light," Physical Review A, vol. 92, no. 5, 2015.

[30] M. Auzinsh, R. Ferber, F. Gahbauer, A. Jarmola, L. Kalvans, and A. Atvars, "Cascade coherence transfer and magneto-optical resonances at 455 nm excitation of cesium," pp. 1–12, 2010.

[31] S. J. Huard, "Polarized Light, Basic Concepts of," in digital Encyclopedia of Applied Physics, American Cancer Society, 2004.

[32] E. Pfleghaar, J. Wurster, S. I. Kanorsky, and A. Weis, "Time of flight effects in nonlinear magneto-optical spectroscopy," Optics Communications, vol. 99, pp. 303–308, 6 1993.

[33] D. Budker, D. Kimball, S. Rochester, V. Yashchuk, and M. Zolotorev, "Sensitive magnetometry based on nonlinear magneto-optical rotation," Physical Review A, vol. 62, p. 043403, 9 2000.

[34] J. H. N. Loubser and J. A. V. Wyk, "Electron spin resonance in the study of diamond," Reports on Progress in Physics, vol. 41, pp. 1201–1248, 8 1978.

[35] N. Reddy, N. Manson, and E. Krausz, "Two-laser spectral hole burning in a colour centre in diamond," Journal of Luminescence, vol. 38, pp. 46–47, 12 1987.

[36] D. A. Redman, S. Brown, R. H. Sands, and S. C. Rand, "Spin dynamics and electronic states of N- V centers in diamond by EPR and four-wave-mixing spectroscopy," Physical Review Letters, vol. 67, pp. 3420–3423, 12 1991.

[37] P. Delaney, J. C. Greer, and J. A. Larsson, "Spin-Polarization Mechanisms of the Nitrogen-Vacancy Center in Diamond," Nano Letters, vol. 10, pp. 610–614, 2 2010.

[38] L. Robledo, H. Bernien, T. V. D. Sar, and R. Hanson, "Spin dynamics in the optical cycle of single nitrogen-vacancy centres in diamond," New Journal of Physics, vol. 13, p. 025013, 2 2011.

[39] M. L. Goldman, M. W. Doherty, A. Sipahigil, N. Y. Yao, S. D. Bennett, N. B. Manson, A. Kubanek, and M. D. Lukin, "State-selective intersystem crossing in nitrogen-vacancy centers," Physical Review B, vol. 91, p. 165201, 4 2015.

[40] V. M. Acosta, E. Bauch, M. P. Ledbetter, C. Santori, K.-M. C. Fu, P. E. Barclay, R. G. Beausoleil, H. Linget, J. F. Roch, F. Treussart, S. Chemerisov, W. Gawlik, and D. Budker, "Diamonds with a high density of nitrogen-vacancy centers for magnetometry applications," Physical Review B, vol. 80, p. 115202, 9 2009.

[41] G. Balasubramanian, P. Neumann, D. Twitchen, M. Markham, R. Kolesov, N. Mizuochi, J. Isoya, J. Achard, J. Beck, J. Tissler, V. Jacques, P. R. Hemmer, F. Jelezko, and J. Wrachtrup, "Ultralong spin coherence time in isotopically engineered diamond," Nature Materials, vol. 8, pp. 383–387, 5 2009.

[42] J. D. A. Wood, D. A. Broadway, L. T. Hall, A. Stacey, D. A. Simpson, J.-P. Tetienne, and L. C. L. Hollenberg, "Wide-band nanoscale magnetic resonance spectroscopy using quantum relaxation of a single spin in diamond," Physical Review B, vol. 94, p. 155402, 10 2016.

[43] J. Smits, J. T. Damron, P. Kehayias, A. F. McDowell, N. Mosavian, I. Fescenko, N. Ristoff, A. Laraoui, A. Jarmola, and V. M. Acosta, "Two-dimensional nuclear magnetic resonance spectroscopy with a microfluidic diamond quantum sensor," Science Advances, vol. 5, p. eaaw7895, 7 2019.

[44] T. Wolf, P. Neumann, K. Nakamura, H. Sumiya, T. Ohshima, J. Isoya, and J. Wrachtrup, "Subpicotesla Diamond Magnetometry," Physical Review X, vol. 5, p. 041001, 10 2015.

[45] I. Fescenko, A. Jarmola, I. Savukov, P. Kehayias, J. Smits, J. Damron, N. Ristoff, N. Mosavian, and V. M. Acosta, "Diamond magnetometer enhanced by ferrite flux concentrators," Physical Review Research, vol. 2, p. 023394, 6 2020.

[46] Y. Schlussel, T. Lenz, D. Rohner, Y. Bar-Haim, L. Bougas, D. Groswasser, M. Kieschnick, E. Rozenberg, L. Thiel, A. Waxman, J. Meijer, P. Maletinsky, D. Budker, and R. Folman, "Wide-Field Imaging of Superconductor Vortices with Electron Spins in Diamond," Physical Review Applied, vol. 10, p. 034032, 9 2018.

[47] D. R. Glenn, R. R. Fu, P. Kehayias, D. Le Sage, E. A. Lima, B. P. Weiss, and R. L. Walsworth, "Micrometer-scale magnetic imaging of geological samples using a quantum diamond microscope," Geochemistry, Geophysics, Geosystems, vol. 18, pp. 3254–3267, 8 2017.

[48] I. Fescenko, A. Laraoui, J. Smits, N. Mosavian, P. Kehayias, J. Seto, L. Bougas, A. Jarmola, and V. M. Acosta, "Diamond Magnetic Microscopy of Malarial Hemozoin Nanocrystals," Physical Review Applied, vol. 11, p. 034029, 3 2019.

[49] D. Le Sage, K. Arai, D. R. Glenn, S. J. DeVience, L. M. Pham, L. Rahn-Lee, M. D. Lukin, A. Yacoby, A. Komeili, and R. L. Walsworth, "Optical magnetic imaging of living cells," Nature, vol. 496, pp. 486–489, 4 2013.

[50] H. Clevenson, M. E. Trusheim, C. Teale, T. Schröder, D. Braje, and D. Englund, "Broadband magnetometry and temperature sensing with a light-trapping diamond waveguide," Nature Physics, vol. 11, pp. 393–397, 5 2015.

[51] M. Negyedi, J. Palotás, B. Gyüre, S. Dzsaber, S. Kollarics, P. Rohringer, T. Pichler, and F. Simon, "An optically detected magnetic resonance spectrometer with tunable

laser excitation and wavelength resolved infrared detection," Review of Scientific Instruments, vol. 88, p. 013902, 1 2017.

[52] J. P. King, K. Jeong, C. C. Vassiliou, C. S. Shin, R. H. Page, C. E. Avalos, H.-J. Wang, and A. Pines, "Room-temperature in situ nuclear spin hyperpolarization from optically pumped nitrogen vacancy centres in diamond," Nature Communications, vol. 6, p. 8965, 12 2015.

[53] P. Fernández-Acebal, O. Rosolio, J. Scheuer, C. Müller, S. Müller, S. Schmitt, L. McGuinness, I. Schwarz, Q. Chen, A. Retzker, B. Naydenov, F. Jelezko, and M. Plenio, "Toward Hyperpolarization of Oil Molecules via Single Nitrogen Vacancy Centers in Diamond," Nano Letters, vol. 18, pp. 1882–1887, 3 2018.

[54] V. Jacques, P. Neumann, J. Beck, M. Markham, D. Twitchen, J. Meijer, F. Kaiser, G. Balasubramanian, F. Jelezko, and J. Wrachtrup, "Dynamic Polarization of Single Nuclear Spins by Optical Pumping of Nitrogen-Vacancy Color Centers in Diamond at Room Temperature," Physical Review Letters, vol. 102, p. 057403, 2 2009.

[55] V. Ivády, K. Szász, A. L. Falk, P. V. Klimov, D. J. Christle, E. Janzén, I. A. Abrikosov, D. D. Awschalom, and A. Gali, "Theoretical model of dynamic spin polarization of nuclei coupled to paramagnetic point defects in diamond and silicon carbide," Physical Review B, vol. 92, p. 115206, 9 2015.

[56] R. Fischer, A. Jarmola, P. Kehayias, and D. Budker, "Optical polarization of nuclear ensembles in diamond," Physical Review B, vol. 87, p. 125207, 3 2013.

[57] F. Poggiali, P. Cappellaro, and N. Fabbri, "Measurement of the excited-state transverse hyperfine coupling in NV centers via dynamic nuclear polarization," Physical Review B, vol. 95, p. 195308, 5 2017.

[58] G. Lindblad, "On the generators of quantum dynamical semigroups," Communications in Mathematical Physics, vol. 48, pp. 119–130, 6 1976.

[59] M. W. Doherty, F. Dolde, H. Fedder, F. Jelezko, J. Wrachtrup, N. B. Manson, and L. C. L. Hollenberg, "Theory of the ground-state spin of the NV- center in diamond," Physical Review B, vol. 85, p. 205203, 5 2012.

[60] P. Udvarhelyi, V. O. Shkolnikov, A. Gali, G. Burkard, and A. Pályi, "Spin-strain interaction in nitrogen-vacancy centers in diamond," Physical Review B, vol. 98, p. 075201, 8 2018.

[61] A. Barfuss, M. Kasperczyk, J. Kölbl, and P. Maletinsky, "Spin-stress and spin-strain coupling in diamond-based hybrid spin oscillator systems," Physical Review B, vol. 99, p. 174102, 5 2019.

[62] P. Kehayias, M. J. Turner, R. Trubko, J. M. Schloss, C. A. Hart, M. Wesson, D. R. Glenn, and R. L. Walsworth, "Imaging crystal stress in diamond using ensembles of nitrogen-vacancy centers," Physical Review B, vol. 100, p. 174103, 11 2019.

[63] J. F. Barry, J. M. Schloss, E. Bauch, M. J. Turner, C. A. Hart, L. M. Pham, and R. L. Walsworth, "Sensitivity optimization for NV-diamond magnetometry," REVIEWS OF MODERN PHYSICS, vol. 92, 2020.

[64] N. B. Manson, J. P. Harrison, and M. J. Sellars, "Nitrogen-vacancy center in diamond: Model of the electronic structure and associated dynamics," Physical Review B - Condensed Matter and Materials Physics, vol. 74, p. 104303, 9 2006.

[65] M. W. Doherty, N. B. Manson, P. Delaney, and L. C. L. Hollenberg, "The negatively charged nitrogen-vacancy centre in diamond: The electronic solution," New Journal of Physics, vol. 13, p. 025019, 2 2011.

[66] A. Batalov, V. Jacques, F. Kaiser, P. Siyushev, P. Neumann, L. J. Rogers, R. L. McMurtrie, N. B. Manson, F. Jelezko, and J. Wrachtrup, "Low Temperature Studies of the Excited-State Structure of Negatively Charged Nitrogen-Vacancy Color Centers in Diamond," Physical Review Letters, vol. 102, p. 195506, 5 2009.

[67] A. P. Nizovtsev, S. Y. Kilin, V. A. Pushkarchuk, A. L. Pushkarchuk, and S. A. Kuten', "Quantum registers based on single NV + n 13C centers in diamond: I. The spin Hamiltonian method," Optics and Spectroscopy, vol. 108, no. 2, pp. 230–238, 2010.

[68] G. Fuchs, V. Dobrovitski, R. Hanson, a. Batra, C. Weis, T. Schenkel, and D. Awschalom, "Excited-State Spectroscopy Using Single Spin Manipulation in Diamond," Physical Review Letters, vol. 101, p. 117601, 9 2008.

[69] Y. Dumeige, M. Chipaux, V. Jacques, F. Treussart, J.-F. Roch, T. Debuisschert, V. M. Acosta, A. Jarmola, K. Jensen, P. Kehayias, and D. Budker, "Magnetometry with nitrogen-vacancy ensembles in diamond based on infrared absorption in a doubly resonant optical cavity," Physical Review B, vol. 87, p. 155202, 4 2013.

[70] M. V. Gurudev Dutt, L. Childress, L. Jiang, E. Togan, J. Maze, F. Jelezko, A. S. Zibrov, P. R. Hemmer, and M. D. Lukin, "Quantum register based on individual electronic and nuclear spin qubits in diamond," Science, vol. 316, pp. 1312–1316, 6 2007.

[71] M. Auzinsh, A. Berzins, D. Budker, L. Busaite, R. Ferber, F. Gahbauer, R. Lazda, A. Wickenbrock, and H. Zheng, "Hyperfine level structure in nitrogen-vacancy centers

near the ground-state level anticrossing," Physical Review B, vol. 100, p. 075204, 8 2019.

[72] L. Busaite, R. Lazda, A. Berzins, M. Auzinsh, R. Ferber, and F. Gahbauer, "Dynamic 14N nuclear spin polarization in nitrogen-vacancy centers in diamond," Physical Review B, vol. 102, p. 224101, 12 2020.

[73] E. R. Macquarrie, T. A. Gosavi, N. R. Jungwirth, S. A. Bhave, and G. D. Fuchs, "Mechanical spin control of nitrogen-vacancy centers in diamond," Physical Review Letters, vol. 111, no. 22, 2013.

[74] A. B. Sannigrahi, "Derivation of selection rules for magnetic dipole transitions," Journal of Chemical Education, vol. 59, no. 10, p. 819, 1982.

[75] D. Lee, K. W. Lee, J. V. Cady, P. Ovartchaiyapong, and A. C. Jayich, "Topical review: Spins and mechanics in diamond," 2017.

[76] A. Gali, "Identification of individual C13 isotopes of nitrogen-vacancy center in diamond by combining the polarization st," Physical Review B, vol. 80, p. 241204, 12 2009.

[77] B. Smeltzer, L. Childress, and A. Gali, "13 C hyperfine interactions in the nitrogen-vacancy centre in diamond," New Journal of Physics, vol. 13, p. 025021, 2 2011.

[78] M. Newville, A. Ingargiola, T. Stensitzki, and D. B. Allen, "LMFIT: Non-Linear Least-Square Minimization and Curve-Fitting for Python," Zenodo, pp. –, 9 2014.

[79] H.-J. Wang, C. S. Shin, C. E. Avalos, S. J. Seltzer, D. Budker, A. Pines, and V. S. Bajaj, "Sensitive magnetic control of ensemble nuclear spin hyperpolarization in diamond," Nature Communications, vol. 4, p. 1940, 10 2013.

[80] B. Smeltzer, J. McIntyre, and L. Childress, "Robust control of individual nuclear spins in diamond," Physical Review A, vol. 80, p. 050302, 11 2009.

[81] S. Felton, A. M. Edmonds, M. E. Newton, P. M. Martineau, D. Fisher, D. J. Twitchen, and J. M. Baker, "Hyperfine interaction in the ground state of the negatively charged nitrogen vacancy center in diamond," Physical Review B, vol. 79, p. 075203, 2 2009.

[82] F. Ticozzi and L. Viola, "Analysis and synthesis of attractive quantum Markovian dynamics," Automatica, vol. 45, pp. 2002–2009, 9 2009.

[83] J.-P. Tetienne, L. Rondin, P. Spinicelli, M. Chipaux, T. Debuisschert, J.-F. Roch, and V. Jacques, "Magnetic-field-dependent photodynamics of single NV defects in

diamond: an application to qualitative all-optical magnetic imaging Related content New Journal of Physics Magnetic-field-dependent photodynamics of single NV defects in diamond: an applicatio," New Journal of Physics, vol. 14, no. 15pp, p. 103033, 2012.

[84] B. Scharfenberger, W. J. Munro, and K. Nemoto, "Coherent control of an NV center with one adjacent 13 C," New Journal of Physics, vol. 16, p. 093043, 9 2014.

[85] R. Fischer, C. O. Bretschneider, P. London, D. Budker, D. Gershoni, and L. Frydman, "Bulk Nuclear Polarization Enhanced at Room Temperature by Optical Pumping," Physical Review Letters, vol. 111, p. 057601, 7 2013.

[86] G. D. Fuchs, V. V. Dobrovitski, D. M. Toyli, F. J. Heremans, C. D. Weis, T. Schenkel, and D. D. Awschalom, "Excited-state spin coherence of a single nitrogen–vacancy centre in diamond," Nature Physics, vol. 6, pp. 668–672, 7 2010.

[87] J. R. Johansson, P. D. Nation, and F. Nori, "QuTiP 2: A Python framework for the dynamics of open quantum systems," Computer Physics Communications, vol. 184, pp. 1234–1240, 4 2013.

[88] M. W. Doherty, N. B. Manson, P. Delaney, F. Jelezko, J. Wrachtrup, and L. C. Hollenberg, "The nitrogen-vacancy colour centre in diamond," Physics Reports, vol. 528, pp. 1–45, 7 2013.

[89] L. T. Hall, P. Kehayias, D. A. Simpson, A. Jarmola, A. Stacey, D. Budker, and L. C. L. Hollenberg, "Detection of nanoscale electron spin resonance spectra demonstrated using nitrogen-vacancy centre probes in diamond," Nature Communications, vol. 7, p. 10211, 4 2016.

[90] R. Lazda, L. Busaite, A. Berzins, J. Smits, F. Gahbauer, M. Auzinsh, D. Budker, and R. Ferber, "Cross-relaxation studies with optically detected magnetic resonances in nitrogen-vacancy centers in diamond in external magnetic field," Physical Review B, vol. 103, p. 134104, 2021.

[91] S. V. Anishchik, V. G. Vins, and K. L. Ivanov, "Level-crossing spectroscopy of nitrogen-vacancy centers in diamond: sensitive detection of paramagnetic defect centers," arXiv, 9 2016.

[92] E. van Oort and M. Glasbeek, "Cross-relaxation dynamics of optically excited N - V centers in diamond," Physical Review B, vol. 40, pp. 6509–6517, 10 1989.

[93] S. V. Anishchik and K. L. Ivanov, "Sensitive detection of level anticrossing spectra of nitrogen vacancy centers in diamond," Physical Review B, vol. 96, p. 115142, 9 2017.

[94] J. Harrison, M. Sellars, and N. Manson, "Measurement of the optically induced spin polarisation of N-V centres in diamond," Diamond and Related Materials, vol. 15, pp. 586–588, 4 2006.

[95] I. Aharonovich, A. D. Greentree, and S. Prawer, "Diamond photonics," Nature Photonics, vol. 5, pp. 397–405, 7 2011.

[96] D. Budker and M. Romalis, Optical Magnetometry, vol. 3 of Optical Magnetometry. Cambridge University Press, 2007.

Appendix

Appendix A

The experimental setups

A.1 The experimental setup for the NMOR experiment

The experimental results of Section 3.3 were achieved by Szymon Pustelny at the University of California, Berkeley [29].

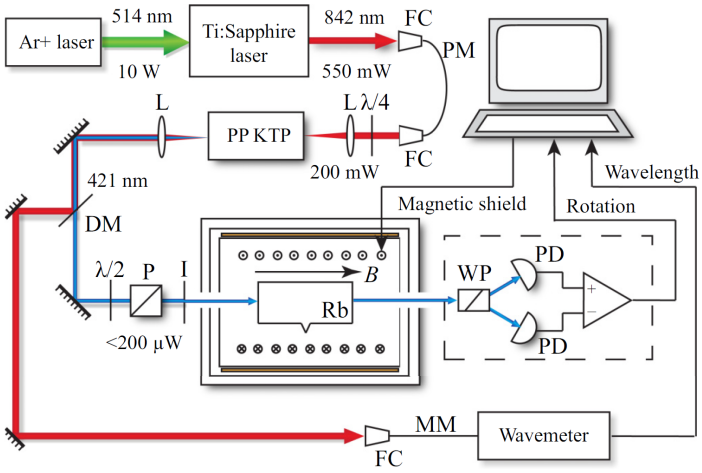

Figure A.1: The experimental setup. P is the polarizer, WP stands for the Wollastone prism, $\lambda/2$ is the half-wave plate, L is the lens, DM stands for the dichroic mirror, I is the iris, FC denotes the fiber coupler, PD is the photodiode, and PM and MM denote polarization-maintaining and multimode fiber, respectively.

A schematic of experimental setup is shown in Figure A.1. Argon (Ar+) laser, emitting 10 W continuous-wave (CW) radiation with wavelength 514 nm, was used to pump the titanium-sapphire laser. The titanium-sapphire laser emits 550 mW near IR radiation (842 nm), which was guided to the site of the main experiment through a single-mode optical fiber. The light coming from the fiber was focused on a periodically poled potassium titanyl phosphate (PP KTP) crystal. The nonlinear properties of the

crystal enable the frequency doubling, converting the IR light (200 mW) into a 0.2 mW blue light (421 nm) beam. The frequency of the blue light was controlled by tuning the frequency of the titanium-sapphire laser. This allowed tuning the blue light in resonance of transition $5^2S_{1/2} \longrightarrow 6^2P_{1/2}$ for both rubidium isotopes (^{85}Rb and ^{87}Rb) (Figure A.2). For the measurements of NMOR dependence on laser power, the frequency of the blue

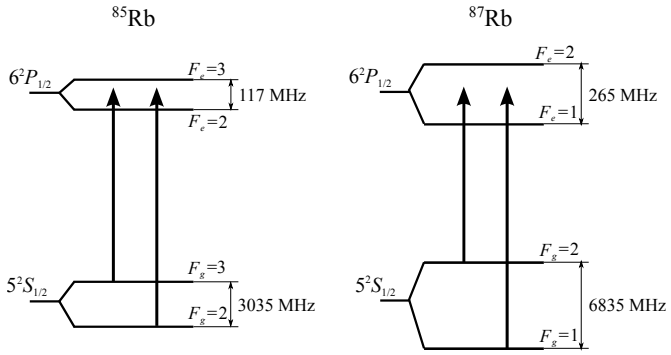

Figure A.2: Energy level diagram of the $5^2S_{1/2} \longrightarrow 6^2P_{1/2}$ transitions in ^{85}Rb and ^{87}Rb.

light was stabilized by referencing the titanium-sapphire laser to an optical cavity and using a wavemeter for monitoring. For additional reference an absorption-spectroscopy setup with an independent reference, cell containing rubidium vapor heated to 70°C, was used.

Rubidium vapor was contained in a cylindrical glass cell (diameter 50 mm, length 100 mm), placed inside a four-layer cylindrical magnetic shield made of μ-metal. The shield provided a passive attenuation of external magnetic fields of 10^6 [96]. A set of additional coils inside the shield were used to compensate the residual magnetic field as well as to provide the bias magnetic field in the direction of light propagation. The generation process of the bias magnetic field provided the magnetic field up to 1-G field [29]. The layers of the shield were thermally isolated and the inner layer along with the cell was heated to about 90°C, reaching the atomic vapor density of 2.4×10^{12} cm^{-3} and the Doppler with of 600 MHz.

In front of the shield, the blue light was spectrally filtered and linearly polarized using a high-quality crystal polarizer. The diameter of the laser beam was controlled with an iris, which not only changed the diameter but also the profile of the beam (3.22). On the other side of the cell, the polarization of light was detected, using a polarimeter which consisted of Wollaston polarizer and two photodiodes. The angle of nonlinear magneto-optical rotation was calculated by dividing the differential photocurrent of the photodiodes by twice the sum of the photocurrents:

$$\phi = \frac{I_1 - I_2}{2(I_1 + I_2)}, \tag{A.1}$$

if the angle of the rotation is considered to be small enough ($\phi \ll 1$). The signals were stored and the magnetic field was controlled using a computer.

A.2 The experimental setup for the GSLAC experiment

Two different samples were used in the experiments to achieve the results described in Section 6.3. The low density sample with nitrogen concentration of 1 ppm was produced by CVD. The high density sample with nitrogen concentration of around 200 ppm was a HPHT crystal. The experiments with the low density sample were performed at the Johannes Gutenberg-University in Mainz by Reinis Lazda, Andris Berzins and Huijie Zheng, and the measurements with the high-density sample were obtained at the Laser Centre of the University of Latvia in Riga by Reinis Lazda and Andris Berzins. A Nd:YAG laser (Coherent Verdi), producing green 532 nm light, was used to irradiate and optically polarize the NV centers (Section 5.3). The luminescence emitted from the ^3E state of the NV center was them monitored. The microwave field was applied to prompt the transition between the ground-state magnetic sublevels.

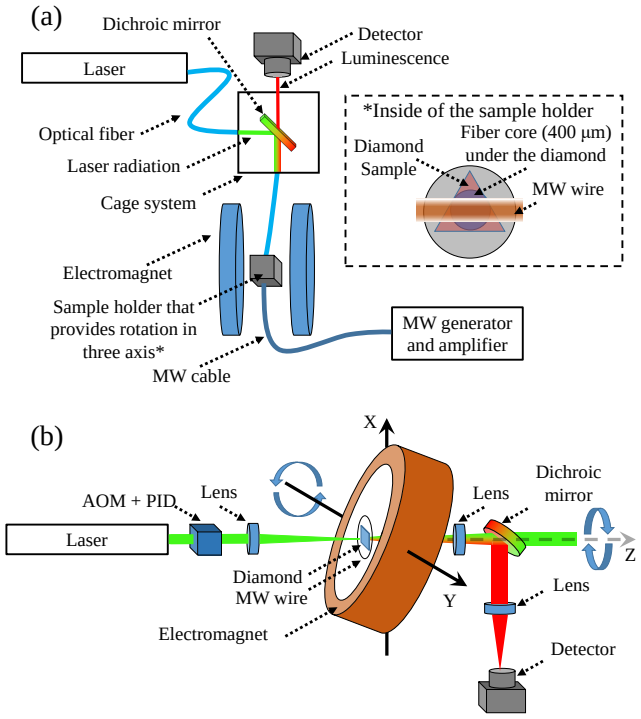

Figure A.3: (a) The setup for the high-density sample experiment. The laser light is guided to the dichroic mirror and to the sample through optical fibers. The fluorescence was passed through the fiber to the dichroic mirror and a long-pass filter and focused onto the photodiode with an amplifier. (b) The setup for the low-density sample experiment. A lens was used to focus the laser light onto the sample. The fluorescence was gathered from the sample using a lens and was measured with a photodetector.

Figure A.3(a) shows the experimental setup used for the experiments with the high-

density sample in Riga. A custom-built electromagnet, initially designed for electron paramagnetic resonance (EPR) experiments, was used to produce the magnetic field. The magnet contains two iron poles 19 cm in diameter and 13 cm in length each that are separated by a 5.5 cm air gap. The inhomogeneity of the magnetic field was estimated using a simulation software COMSOL to be 0.0002 mT over the sensing volume. The diamond sample was inserted into a nonmagnetic sample holder, which was custom-made by STANDA. The holder provided three axes of rotation so that the NV axis could be aligned with the bias magnetic field. The laser (Coherent Verdi Nd:YAG) produced the light with a wavelength of 532 nm, that was passed through an optical fiber with a core diameter of 400 micrometers (numerical aperture of 0:39). The red fluorescence was collected with the same fiber. To separate the residual green light from the fluorescence, a dichroic mirror and a long-pass filter (Thorlabs DMLP567R and FEL0600) were used. The fluorescence was then focused onto an amplified photodiode (Thorlabs PDA36A-EC). A digital oscilloscope (Agilent DSO5014A or Yokogawa DL6154) and a DAQ card (Measurement Computing USB-1408FS) were used to record and average the ODMR signals. The microwave field was generated and amplified in two regimes, requiring different devices: for the low frequencies a TTi TG5011 generator (0.001 mHz to 50 MHz) was used and for the high frequencies a function generator (SRS SG386) with a power amplifier (Minicircuits ZVE-3W-83+) which provided up to +30dBm.

Figure A.3(b) shows the setup used for the experiments with the low-density sample in Mainz. A custom-made electromagnet consisting of 200 turns wound on a water-cooler copper mount. The electromagnet was able to achieve a magnetic field up to 1035 G by producing a field of 2.9 mT/A. The diamond holder provided the rotation of the diamond around the z-axis (NV axis). The translation and rotation of the electromagnet was provided by a computer-controlled 3D translation stage (Thorlabs PT3-Z8) and a rotation stage (Thorlabs NR360S, y-axis). This provided all degrees of freedom for centering and aligning the diamond with respect to the magnetic field. The laser intensity stabilization was implemented in combination with an acousto-optic modulator (AOM), a photodiode and a proportional-integral-derivative (PID) controller. A function generator (SRS SG386) was used to generate the microwave field over the entire range combined with power amplifiers: an RFLU PA0706GDRF amplifier (Lambda) at high frequencies and (Minicircuits ZHL-32A+) amplifier at low frequencies.

A.3 The experimental setup for the DNP experiment

The experiments were executed by Reinis Lazda and Andris Berzins at the Laser Centre of the University of Latvia.

The sample used in the experiments to achieve the results described in Section 7.2 and in Section 6.3.4 (Figure 6.19) was a CVD diamond crystal with a (100) surface cut. The nitrogen concentration of the crystal was 5–20 ppm. The crystal was irradiated with 10^{17} cm^{-2} e^- irradiation dosage at 2 MeV e^- irradiation energy. The sample was then annealed: first at 800 °C and then 1100 °C. In the annealing process NV centers were created in the bulk of the diamond.

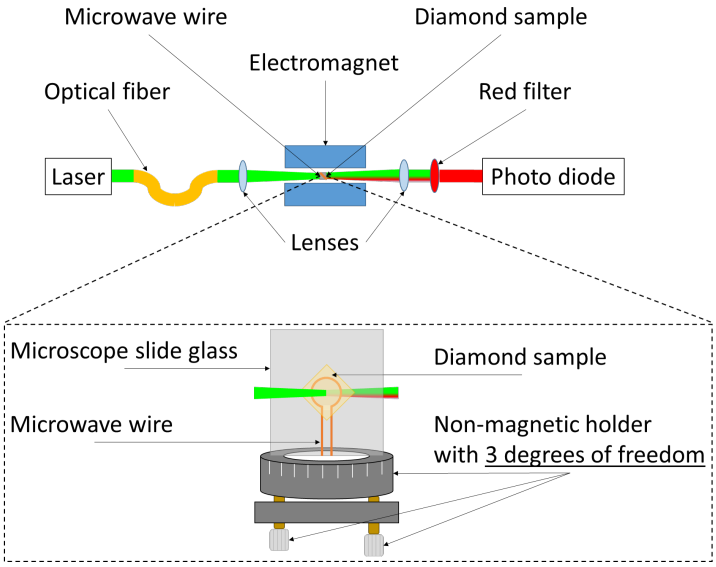

Figure A.4: Experimental setup, top shows the overall experimental scheme, bottom shows a zoomed in detailed scheme of the sample holder and the microwave antenna.

Figure A.4 shows the experimental setup used to perform the measurements. A non-magnetic sample holder with three degrees of freedom is attached to an aluminum rail. Two aspheric condenser lenses, used for delivering and collecting the light to and from the sample, are also attached to the rail, which is inserted into an electromagnet. It consists of two iron poles with a length of 13 cm and diameter of 19 cm and an air gap of 5.5 cm between the poles. The inhomogeneity of the magnetic field created by the electromagnet was determined by numerical calculation to be about 0.2 μT in the sensing volume of $2 \times 2 \times 0.1$ mm^3. An "omega" shaped microwave antenna, about 1 mm in diameter, is etched on a microscope slide glass with the diamond sample glued to the antenna. The slide glass is then attached to the non-magnetic sample holder on the aluminum rail. A Nd:YAG laser was used to generate green (532 nm) light, which is delivered to the sample by a single mode optical fiber. The red fluorescence is filtered using a red longpass filter and then focused onto an amplified photodiode. A digital Yokogawa oscilloscope is used

for recording and averaging of the signals. The microwave field was generated with a combination of a function generator (SRS SG386) and a power amplifier (Minicir-cuits ZVE-3W-83+). Finally, the recorded signals were stored on a computer.